Department of Precision and Microsystems Engineering

Reciprocating Geared Mechanism With Compliant Suspension

Jan Wessels

Report no : MSD 2016.004
Coach : dr. N. Tolou
Professor : prof. dr. ir. J.L. Herder
Specialisation : Mechatronic System Design
Type of report : MSc Thesis
Date : 25.01.2016

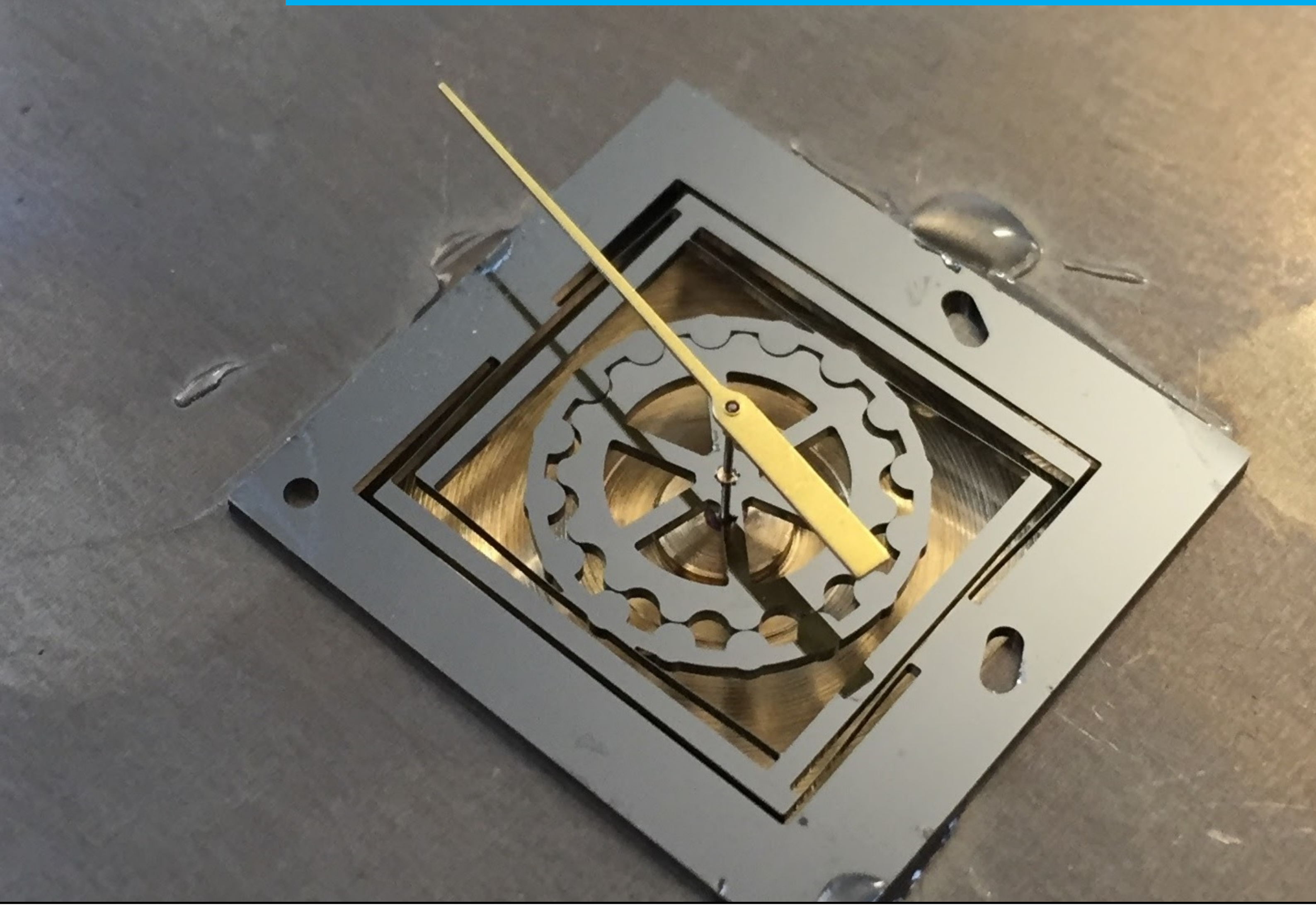

TU Delft Delft University of Technology

Precision and Microsystems Engineering

Challenge the future

Reciprocating Geared Mechanism With Compliant Suspension

For application in a mechanical wristwatch

by

Jan Wessels

in partial fulfilment of the requirements for the degree of

Master of Science

in Mechanical Engineering

at the Delft University of Technology,

to be defended publicly on Monday January 25, 2016 at 10:00 AM.

Student number:	1516671	
Project duration:	January 1, 2015 – January 25, 2016	
Supervisor:	prof. dr. ir. J.L. Herder	
Daily supervisor:	dr. N. Tolou,	TU Delft
Thesis committee:	dr. F. Alijani,	TU Delft
	ir. J.F. Schorsch,	TU Delft

This thesis is confidential and cannot be made public until January 25, 2023.

An electronic version of this thesis is available at `http://repository.tudelft.nl/`.

PREFACE

The drive for innovation has been my motivation to start my journey at the Technical University Delft. To be part of technological advancements and never stop learning is my goal for the future.

The complex and delicate inner workings of mechanical watches have always sparked my interest. When this innovative project proposal in collaboration with TAG HEUER was announced by Nima Tolou, of course I was the first to sign up. This project has given me space to express my opinion and valued my input. I was lucky to be on a project with such freedom and possibilities, and most importantly to be allowed to make mistakes and learn from them.

In the tribulations of my Master‘s thesis I got support from a group of young talented engineers at TU Delft and Flexous, who always provided sound advice. Some people that deserve to have their names mentioned are Davood, Sjoerd, Guiseppe, Wout, Sybren, and Wouter. Also the contribution of the team at TAG HEUER has been valuable, for which my gratitude.

Besides an increased understanding in the interesting world of horology I have gained much on a personal level. The process of graduating has made me a more complete person by the realization that a balance is needed to have a sustainable lifestyle. During this process my supervisor Just Herder has been an inspiration both on a technical, as well as on a personal level.

Of course I want to thank my parents and family for their support, and in particular my girlfriend Abigail.

Jan Wessels
Delft, January 2016

Contents

1 Introduction **1**

I Literature review **5**

Towards A Compliant Rotational Micro Speed Reducer (CRSR) **7**

II Thesis design paper **19**

Reciprocating Geared Mechanism With Compliant Suspension **21**

III Chapters **31**

2 Case specific design **33**

3 Design principles **39**
- 3.1 Functions original concept . . . 39
- 3.2 Suspending annulus . . . 39
- 3.3 Guarantee contact . . . 41
- 3.4 Suspension synthesis . . . 42

4 Prototypes **47**
- 4.1 Working principle original concept . . . 47
- 4.2 Prototype 0 . . . 48
- 4.3 Prototype I . . . 49
- 4.4 Prototype II . . . 53
- 4.5 Prototype III . . . 54

5 Modelling **59**
- 5.1 Mechanical advantage . . . 59
- 5.2 Static balancing . . . 61
- 5.3 Efficiency gear contact . . . 63
- 5.4 Frictional losses due to stiffness . . . 66
- 5.5 Negative stiffness . . . 70
- 5.6 Ansys model . . . 72
- 5.7 Free-Body-Diagram . . . 77
- 5.8 New Ansys model . . . 81

6 Experiments **85**
- 6.1 Force-deflection measurement . . . 85
- 6.2 No-load torque measurement . . . 91

Bibliography **103**

A Ansys APDL code for Silicon prototype **105**

B Ansys APDL code improved model - dual layer **111**

C Matlab script Linear Beam Theory model **117**

D Matlab script cycloidal rotor **121**

E Matlab script cycloidal rotor contact force analysis **125**

F Ansys APDL code for negative stiffness **129**

1

Introduction

This thesis is written in collaboration with TAG Heuer, well-known for their craftsmanship in mechanical watches. The goal of the project is to introduce flexible monolithic mechanisms in a mechanical wristwatch. The aim is to reduce the total thickness of the watch, and reduce the total number of parts in the assembly. Part of the project is to innovate and improve on a specific part of the mechanical watch, the gear train. This thesis focusses on a particular part of the gear train; the first gear in this gear train, the barrel gear, which functions as the energy storage and driving mechanism of the watch.

This thesis consist of three parts. Firstly a literature review, part I, will provide an overview of traditional speed reducer mechanisms. This literature review is needed to determine the direction for the rest of the research. The second part, part II, contains the article on the 'novel compliant reciprocating gear mechanism' presented in this thesis. This section contains the outcome of my research and is therefore the most important chapter in this thesis. The third part, part III, contains a detailed report of the performed actions during this research, of which the corresponding modelling code is provides in the appendices.

The following section will give a background on key aspects and problems of the gear train as it is implemented in today's mechanical watches. Key features of the barrel gear will be presented to give the reader a grasp of the topic of this thesis before continuing with the literature review in part I.

Case study - mechanical watch

A typical watch movement comprises approximately 30 gears[1]. Not all of those gears are in the main gear train, other functions like winding the watch and setting the time are carried out by gears. The gears in the main gear train have two functions in the watch. Firstly the gear train has a *kinematic* function. It bridges the rotational speed ratio between the slow moving barrel gear (first gear) and the fast moving escapement wheel (last gear). The gear ratios in between the barrel gear and the escapement wheel determine the rotational speed of the indicators of the watch. The gear ratios of the gears in between has to be carefully chosen. The combined gear ratio of the several stages is in the range of 7200, between escapement wheel and barrel gear.

To achieve a combined ratio of 7200 in the main gear train, several stages of compound gears are used, see figure 1.1. High transmission ratios per stage are desired to limit the required number of gears in the gear train. In a compound gear train this means large differences between the diameters of gears, for example 110/16 (ratio 6.875) and 90/9 (ratio 10)[1]. The maximum ratio in this compound gear train is dominated by the manufacturing of the smallest gear, the pinion, which is typically about 1mm in diameter with a tooth count of 7[1].

The bearings in which the shafts of these gear pairs are suspended are called 'jewels', and are made of synthetic rubies, (aluminium oxide, Al_2O_3). These bearings are used for their high wear resistance and low friction coefficient.

The second function of the gear train is a *kinetic* one. Energy is transferred from the main spring to the escapement wheel, see figure 1.1. As a result of the high gear ratio the torque applied by the main spring is

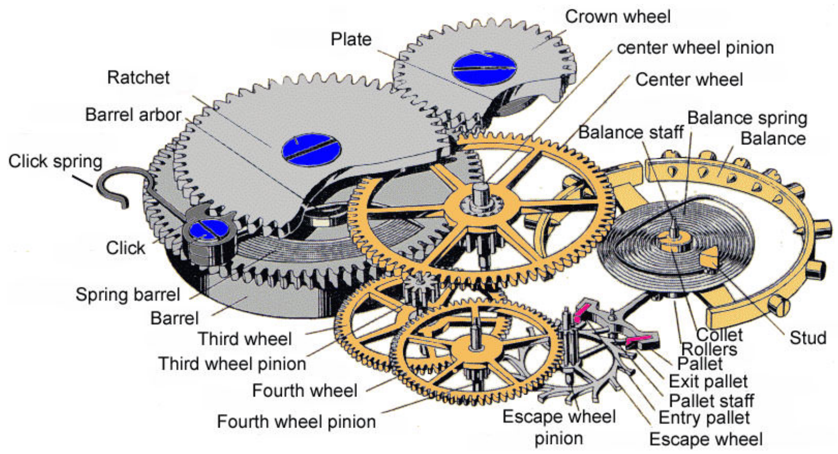

Figure 1.1: Overview of functional components in a gear train in traditional mechanical watches. The compound gears are fixed on shafts and suspended using micro bearings called jewels.

reduced to an appropriate level for the most delicate parts of the watch; the balance, or the 'brain' of the watch. The barrel spring, the 'heart' of the watch, contains the energy used to drive the timekeeping mechanism. The barrel spring is contained in a drum, the barrel, with a gear profile on the edge, thus called the barrel gear. The barrel gear is the first gear in the main gear train. Figure 1.2(a) shows the key components of barrel gear. The entire assembly is suspended in two jewel bearings on both ends of the central axis. The central axis is called the barrel arbor, which is used to rewind the watch either manually or automatically. The barrel (gear) is suspended on a jewel bearing on the barrel arbor itself. The main spring applies a torque between the barrel gear and barrel arbor, resulting in a driving torque for the gear train. This allows for a continuous rewinding of the system while keeping track of time.

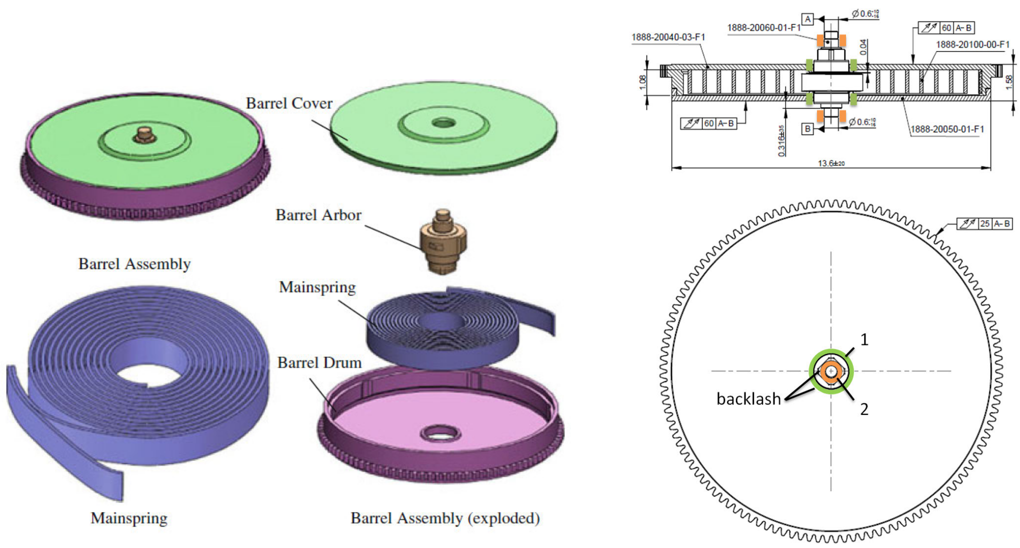

(a) Components and assembly of the barrel gear system[1]. The main spring is the energy storage of the mechanical watch. The gear profile on the barrel drum drives the gear train.

(b) Dimensions of a barrel gear provided by partner TAG Heuer. Positions of the bearings suspending the assembly are highlighted.

Figure 1.2: Assembly of the barrel gear and dimensions as provided by partner TAG Heuer. The barrel gear is continually rewound during operating using the 'barrel arbor'.

As mentioned above this thesis focusses on the first gear in the gear traditional gear train, the barrel gear. A schematic of the barrel gear assembly, including key dimensions, is provided by our partner TAG Heuer, see figure 1.2(b). The main spring delivers a torque on the start of the gear train with a working range between 6.3Nmm and 10.8Nmm. This torque is relatively high compared to the size of the system due to the high transmission ratio. As a result the barrel gear will make a single rotation in $6-8$ hours, depending on the precise gear ratio.

The barrel spring is an assembly of several components, seen in figure 1.2(a). Two jewel bearing locations are needed for the working principle of the barrel spring. These jewels each introduce some backlash in the system, see figure 1.2(b). The backlash in jewel 1 and 2 is respectively $10-15\mu$m micron and 10μm. The total backlash at the perimeter of the barrel gear is therefore $20-25\mu$m. The out-of-plane backlash of the barrel gear is 6μm (axial translational backlash). However an out-of-plane backlash of 24μm at the perimeter of the barrel gear is observed. This is the combined backlash of both the translational and rotational error of the jewels suspending the barrel gear.

The general dimensions of the barrel gear assembly are to be kept as a given for this thesis. The gear profile used on the barrel gear however can be changed. Also the specifications of the barrel spring are to be kept, defining the input torque for the system.

I

Literature review

Towards A Compliant Rotational Micro Speed Reducer (CRSR)

J. Wessels, N. Tolou and J.L. Herder
Faculty of Mechanical Engineering
Delft University of Technology, Delft, The Netherlands

***Abstract*—A categorization aiming at miniaturization of existing speed reducer systems is established. Categorization of the speed reducer systems is based on key aspects of compliant mechanisms design: The type of motion; planar fabrication methods; and complexity of the mechanism. The 'ring reducer' mechanism and 'pulse transmission' mechanism both have attributes advantageous for conversion into compliant mechanism, making miniaturization within reach. Recommendations are made for the development of a micro speed reducer system using a (partially) compliant design.**

***Index Terms*—gear mechanism, monolithic, MEMS**

I. Introduction

SPEED reducers are a specific branch of mechanisms designed to create a ratio between the input and output of the system. Different types of motion can be reduced, but the majority of speed reducers in use is based on rotating input and output shafts. An example of a speed reducer system is bicycle's chain and sprocket. The mechanical advantage created by the speed reducer system is used to reduce input force on the pedals. Especially when cycling up a steep slope a large reduction ratio is preferred.

A bicycle's chain and sprocket is an example of a speed reducer mechanism on a macro scale. Often macro speed reducer systems are not suitable for downscaling to the micro domain. Tolerances become increasingly important and assembly of the micro mechanism becomes more difficult. These are two of the reasons why compliant mechanisms are often used in the micro domain[1].

Compliant mechanisms transfer motion, force or energy, like conventional rigid-body mechanisms. A compliant mechanism gains its mobility from deflection of elastic members instead of relative motion between separate parts like a conventional mechanism. On a micro-scale compliant mechanisms have several advantages, such as; reduced friction and wear, reduced cost, no need for lubrication and no need for assembly[2].

In the field of compliant mechanisms speed reducers are developed and implemented. These compliant speed reducers rely on deformation of elastic members for which energy is needed. As a result of using elastic members compliant mechanisms have an inherent stiffness. This stiffness is a disadvantage for a compliant speed reducer mechanism. Energy stored inside the mechanism cannot benefit the mechanical advantage[3].

Compliant mechanisms without stiffness would overcome this drawback. Instead of accumulating energy inside the mechanism the energy is transferred to the output directly. As a result the energy in the system would remain constant, resulting in an optimal mechanical advantage of 1, equal to rigid body mechanisms[3]. Static balancing is a technique enabling mechanisms without inherent stiffness[4][5].

Motions that mechanisms can perform can be categorized in four categories, as depicted in table I. Motions can be transferred, meaning the input and output motion are of the same type. A motion conversion mechanism has a different type of input motion as output motion. Arguably rotational-to-translational and translational-to-rotational belong to the same type of motion mechanisms. This work only focusses on input and output motion of speed reducers of the same type (motion transferring), that being more suitable for the application it is intended for, a compliant micro drive-train with fixed input-output ratio.

A preliminary search toward compliant speed amplifiers/reducers shows that already some research towards compliant translational amplifiers has been done[6][7]. Due to the geometry of these mechanisms the input motion is amplified (or reduced) at the output. Most of these mechanisms are purposely designed to enhance the sensitivity of sensors[8][6][7], or to increase the range of motion of actuators[9][10][11]. For this purpose these compliant translational motion amplifiers are very well suited.

In order to replace the most prominent existing speed reducers a rotational motion needs to be amplified or reduced, functioning like a gear train. Not a single compliant mechanism was found that could amplify or reduce a rotating input to a rotating output with a full rotation on the output shaft. In this research only compliant mechanisms with a full cycle output motion were selected as potential CRSRs, since only they could substitute existing speed reducer mechanisms. One design, consisting of a compliant ratchet and pawl in combination with a guidance shuttle between both rotary inputs, had some features of a speed reducer although not specifically designed for this purpose[12].

TABLE I
TYPES OF MOTION FOR PLANAR COMPLIANT MECHANISMS

	rotation	translation
rotation	[12]	excluded
translation	excluded	[6][7][8][9][10][11]

The traditional speed reducers have drawbacks when scaled down to the micro domain. The friction and backlash between the moving parts becomes a larger factor for small systems. Attempts on scaling down traditional speed reducer mechanisms have been made[13]. Scaling down these traditional speed reducers results in problems such as increased wear and adhesion[14], which are not encountered on a macro scale. Compliant mechanisms lack most of the aforementioned drawbacks. Also assembly becomes problematic when the components become smaller and tolerances tighter. Compliant mechanisms are relatively easy to scale down, making them very suitable for micro applications. However no compliant mechanisms where found in literature functioning as a rotational speed reducer.

The aim of this report is to give an overview of rotational speed reducer systems and identify which ones are potential candidates for transformation into a compliant counterpart with the aim on a micro speed reducer system.

Technological improvements keep pushing the borders of miniaturization. Similarly drive trains are desired to reduce in size. A single compliant mechanism that could replace all components of traditional (micro) drive-train systems would greatly reduce the cost and time needed to fabricate the system. Besides the economic relevance compliant mechanism have the potential to be very thin, potentially resulting in a slim design.

One of the drawbacks of compliant mechanisms is their limited range of motion[2]. Designing a CRSR capable of delivering a full rotation at the output is therefore a challenge, which requires a clever design to transform a limited motion into a full rotation.

II. METHODS

To identify why there is a lack of (partially) compliant rotational speed reducers a broader search was performed on speed reducers in general. To structure the search sets of keywords are defined (table II). The separate keywords are combined with keywords from the other sets, but also with keywords from the same set. For example the search term ‘speed’ is combined with ‘compliant’, but also with ‘reducer’ and ‘variator’.

TABLE II
TYPES OF MOTION FOR PLANAR COMPLIANT MECHANISMS

sets	keywords
variable speed	variable speed; speed; converter; increaser; reducer; amplifier; variator; gearless; ratio
variable displacement	displacement; motion; stroke; amplifier; multiplier; increaser
compliant mechanisms	compliant; mechanism; flexible; monolithic; lumped; distributed

These search terms are systematically used in the search engines *Google Scholar* and *Scopus*. Both of these search engines gave many hits on journals and conference articles. *Espacenet* was mainly consulted for searching for patents. Relevant references from articles found with the use of aforementioned keywords were also included in this literature survey.

The literature search provided a variety of different reducer principles. All the *compliant* mechanisms with an inherent ratio are already discussed in the introduction (table I). The remainder of the speed reducers are part of the broader search to provide an overview of existing principles.

These speed reducers will be ranked on fitness to be transformed into a compliant counterpart. Firstly the speed reducer systems are categorized based on their motion. After this general categorization multiple criteria are introduced aiming towards conversion into a compliant mechanism. The categories and criteria will be discussed in this section, after which the selection will be made in the results section.

A. Classes of motion

In general three motion types are identified in the encountered speed reducer systems: rotation about a fixed axis, motion with a movable axis and motion with a skewed axis (nutation). These motion classes will be elaborated in this paragraph. For the last two motion types, motion with movable and skewed axes, a distinction can be made between rotation about the main axis, or no rotation about the main axis. The number of defined motion classes is thus five. The goal of a speed reducer system is to have a fixed rotational output shaft with a certain speed. This output shaft will be illustrated in **green** in the following figures. The **red** parts indicate the functional parts of the speed reducer system. The motion of the **red** parts determine to which class of motion the speed reducer system belongs.

Rotation with fixed axis: An often used principle to obtain a transmission ratio between two rotating shafts is using cylinders with different radii (figure 1). The ratio between the radii results in a ratio between rotation speeds of the two shafts. This principle can be directly expanded to the number of teeth on a gear. The angular velocity of both the input and output shaft remain constant. This principle is based on the fact that the axes of the moving parts are fixed. As a result of the fixed axis, the point of contact between moving objects will remain at a fixed position. Note that this principle can also be applied in a spatial configuration (i.e. a worm gear), besides the illustrated planar configuration.

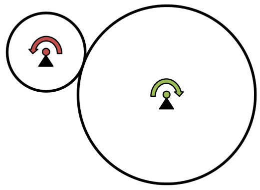

Fig. 1. Illustration of rotation with fixed axis motion principle

Rotation with floating axis: In addition to the pure rotation of the previous principle, speed reducers with movable axes also have a translating movement. The rotating shaft spins about its own axis while spinning about another axis (figure 2). As a result the point of contact between parts will shift. Various speed reducers rely on this motion principle, the planetary gear being the most well known. Different layouts of the components can result in high reduction ratios in a small volume. Especially reducers relying on a small difference in teeth can achieve high reduction ratios.

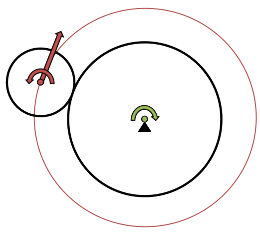

Fig. 2. Illustration of rotation with floating axis motion principle

No rotation with floating axis: The floating axis does not necessarily have to make a rotating motion. Instead speed reducers rely on a circular motion of the floating axis, instead of pure rotation (figure 3). The path traced by the floating axis can be described as a circle about another (fixed) axis. This motion type is comparable with the planetary gear example, except now the planet gear does not make a full rotation relative to its carrier. This motion type can be very useful for the application on compliant mechanisms since here a full rotation is problematic. Instead the focus should lie on describing a circular path.

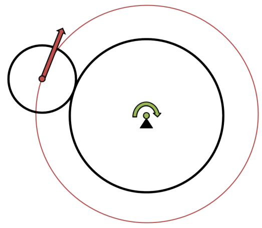

Fig. 3. Illustration of floating axis without rotational motion principle

Rotation with skewed axis: A principle resulting in high reduction ratios is nutation. Like the previous motion principle parts moves around another (movable axes), but the axis of a nutating part is skewed (figure 4). The resulting motion is best described by the movement a gyroscope makes when it is slightly out of balance. The point of contact between parts will move along the circumference of the nutating object.

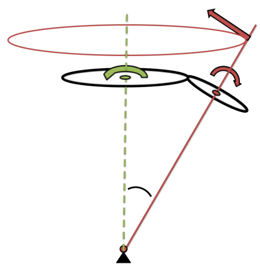

Fig. 4. Illustration of rotation with skewed axis motion principle

Nutation based reducers using gear teeth differences are found, but also reducers with solely rolling contacts have been encountered. The point of contact between objects will not be constant, but will move around the circumference of the nutating object.

No rotation with skewed axis: Following the same reasoning as before, there should be a motion type where the skewed floating axis does not rotate about its own axis. Again this would be an interesting type of motion for conversion into a compliant mechanisms because no full cycle rotation is encountered.

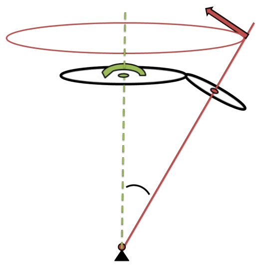

Fig. 5. Illustration of skewed axis without rotational motion principle

B. Criteria towards compliance

In order to identify speed reducer principles that are suited to be converted into a compliant counterpart, other criteria are to be defined. This paragraph discusses the chosen criteria and the importance for compliant mechanisms. These criteria are chosen with the aim on finding the most promising speed reducer systems with the eye on a compliant version. The criteria are therefore based on the known characteristics of compliant mechanisms. Some of these characteristics have already been addressed in the introduction, others will be elaborated in the next section.

Continuous or reciprocation: The first classification is aiming to distinguish speed reducer systems relying on a full cycle motion (continuous) from mechanisms with a reciprocating motion. The reasoning behind this classification is that a full rotation is hard to accomplish with a monolithic mechanism. Even though one paper has proposed a compliant mechanisms capable of a full cycle rotational motion [15], practical designs are not yet developed. The mechanisms relying on a reciprocating motion are combined with a rectifying mechanism resulting in a full cycle rotational output. Speed reducers in the reciprocating group have at least one functional part making a reciprocating motion. Of course any full continuous (full cycle) mechanism could be used to make a reciprocating motion. These mechanisms however are not designed to transform a reciprocating motion into a continuous motion. Therefore a distinction is made between reciprocating motion resulting in a full cycle output (*reciprocating motion*) and a continuous motion resulting in a full cycle motion (*continuous motion*).

Spatial or planar: Several techniques are known of fabricating planar structures/mechanisms on a very small scale [16]. Fabrication of three-dimensional mechanisms on a small scale is more difficult to realize. A distinction is made between speed reducer mechanisms where all functional parts lie in one plane and a spatial speed reducer mechanism. The *planar* principles are desired for both fabrication and (possible) assembly of the speed reducer mechanism on a small scale. Speed reducers with functional parts in multiple planes are defined as spatial. These mechanisms cannot be manufactured with planar fabrication techniques without some sort of assembly afterwards. Per definition speed reducers relying on a motion with a skewed axis are spatial mechanisms. For the other two motion types it depends in which plane the parts rotate. For instance the axes in a differential mechanism are perpendicular, therefore this speed reducer mechanism is classified as being *spatial*.

Number of functional parts: In general the more parts are required for the system to function, the more complicated the system is. A complicated system will be more difficult to turn into a compliant counterpart than a simple system comprising few parts. For this categorization the exact number of parts is not of importance. A rough division is made between systems with a small number of parts ($n \leq 6$) and systems requiring a large number of parts ($n > 6$) to function. As can be seen in table III some fall in both the '$n \leq 6$' and '$n > 6$' categories. These systems can both function with a small or large number of parts. In most cases a larger number of parts can lead to an i.e. a higher reduction ratio. Therefore the criterion of number of functional parts sometimes depends on the functionality of the speed reducer itself. Still this criterion is included since it gives an indication on the complexity of the system.

III. Results

A wide variety of speed reducers is encountered in this broader field and summarized in table III.

The most promising speed reducer systems are to be selected and grouped. Firstly all spatial speed reducer systems are eliminated since planar fabrication methods for (compliant) micro mechanisms are desired. This results in a feasible selection of seven speed reducer systems, highlighted in table III with a bold font.

fixed (compound) gears Firstly a wide variety of geared speed reducer systems where encountered for both fixed parallel axes (e.g. multi-stage helical gear reducer) as well as fixed perpendicular axes (e.g. worm gear reducer). Different types of geared shapes have been used, the involute gearing system being the most commonly used.

(compound) planetary gears Planetary gear reducers are well-known for their high speed reduction in a small volume. Compound planetary gears can achieve even higher reduction ratios by using a multi-stage carrier gear. In contrast to the fixed axes of the previous system, the planetary gear system makes use of a floating gear called the planet gear. In the

traditional planetary system these planet gears are mounted on a carrier.

belt/chain drive Belt and chain drives connect two axes positioned apart. The reduction principle is identical to the fixed gear system, where the radii of the gears determine the speed reduction. A system combining a planetary system with a belt drive is also encountered.

cycloid reducer A cycloid reducer uses a circular motion of a relatively large planet gear to obtain a reduction ratio with respect to the outer ring. Different shapes of the planet gears are proposed resulting in a high reduction ratio in a small volume. The high reduction is achieved via a small teeth difference between the outer ring and planet gear.

harmonic reducer Harmonic reducers use a flexible ring with teeth to achieve a reduction ratio. A cam mechanism pushes the flexible ring against a ring gear with a small teeth difference compared to the flexible ring. As a result the high reduction ratios can be achieved.

(three-)ring reducer A ring reducer uses a circular motion of the outer ring gear to obtain a rotational motion of the sun gear. The reduction ratio is again obtained using a small teeth difference between the gears.

pulse transmission This reducer system, unlike the previously mentioned systems, does not rely on a full rotation of all its comprising parts. The reduction ratio is achieve via a ratio between the crank and the rocker. The reciprocating motion is rectifier using a ratchet mechanism.

Most of these remaining speed reducers still rely on a full cycle motion of a large number of parts. Conversion of these systems into a compliant mechanisms is difficult, if not impossible. After eliminating all the systems relying on a full cycle motion of all comprising parts we end up with two speed reducer systems, see table IV. Both of these systems consist of a small number of parts, hence the last criteria is met.

TABLE IV
SPEED REDUCERS AND THEIR MOTION TYPE

	motion type
(three-)ring reducer[34][35]	floating no rotation
pulse transmission [37][38][39]	fixed

Table shows the remaining speed reducer systems after eliminating the non-viable ones. These systems will be discussed and elaborated on further and explained how they could result in a compliant speed reducer system.

(Three-) ring reducer: A special case of a planetary gear where the planet gear is an internal gear

TABLE III
SPEED REDUCERS AND THEIR WORKING PRINCIPLE

	motion type	planar/ spatial	continuous/ reciprocation	number n of functional parts
fixed (compound) gears[17]	fixed rotation	planar/spatial	continuous	$n \leq 6$
rolling cam reducer[18][19]	fixed rotation	spatial	continuous	$n > 6$
(compound) planetary gear[20][21][22]	floating rotation	planar/spatial	continuous	$n \leq 6$ & $n > 6$
(gearless) differential[23][24]	floating rotation	spatial	continuous	$n \leq 6$ & $n > 6$
belt/chain drive[25]	fixed/floating rotation	planar	continuous	$n \leq 6$
cycloid reducer[26][27]	floating rotation	planar	continuous	$n \leq 6$
nutating reducer[28][29][30]	skewed rotation	spatial	continuous	$n \leq 6$
rolling balls reducer[31][32]	skewed rotation	spatial	continuous	$n > 6$
harmonic reducer[33]	fixed rotation	planar	continuous	$n \leq 6$
(three-)ring reducer[34][35]	floating no rotation	planar	reciprocation	$n \leq 6$
R-S-R reducer[36]	fixed rotation	spatial	continuous	$n \leq 6$
pulse transmission[37][38][39]	fixed rotation	planar	reciprocation	$n \leq 6$

ring. Figure 6 shows the schematic of the three-ring reducer. The ring gear makes a circular motion around the sun gear, without rotating itself. As a result the sun gear makes a rotating motion with a reduced speed.

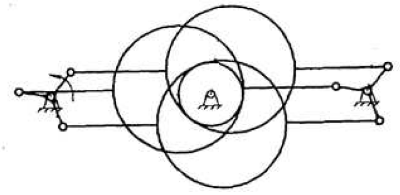

Fig. 6. Three-ring reducer illustration [35]

The circular motion is realized with two rotating shafts on both ends. Other methods of achieving a circular motion can be found, some not relying on a full rotation. Compliant mechanisms could be used for this purpose.

The ratio R_i between the input and output is defined by the number of teeth on the internal gear ring and the sun gear and can be calculated as follows. From this equation follows that a small teeth difference between the internal ring gear and the sun gear results in a large reduction ratio.

$$R_i = \frac{n_{annulus} - n_{sun}}{n_{sun}}$$

Pulse transmission: A pulse transmission is based on a reciprocating motion in combination with a rectifier to only allow motion in one direction (like a ratcheted wrench). The reciprocating motion is often obtained by a crank-slider mechanism. But other mechanisms to create a reciprocating motion are found in literature, such as a swash plate mechanism[37]. This principle is also applied in piezoelectric (PZT) motors. The small translational motion of the PZT is amplified with a lever and rectified with a ratchet and pawl mechanism[39]. The reciprocating part of these systems deflects over (relatively) small angles, therefore ideal for conversion into a compliant mechanism. The ratio between the input and output depends on the lengths of the interconnecting links and the resolution of the rectifier mechanism.

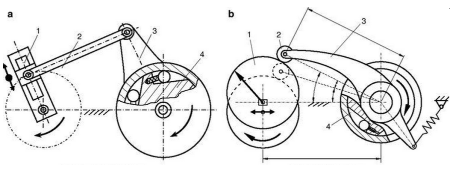

Fig. 7. Examples of pulsating speed reducer systems

IV. Discussion

From the two selected speed reducer systems can be seen that two different approaches could lead to a compliant speed reducer. One way is to use a reciprocating mechanism with limited rotation combined with a mechanisms only allowing motion in one direction (e.g. ratchet and pawl). The other way is to use a smart motion path, e.g. a circular path, eliminating the problematic full rotational motion.

Figure 8 shows a proposition of a three-ring reducer without the full rotational revolute joint. Two carefully coordinated translational inputs are required for the ring in this mechanism to describe a circular path. As a result of this modification all the **red** joint angles have a limited motion, thus can be replaced by compliant joints.

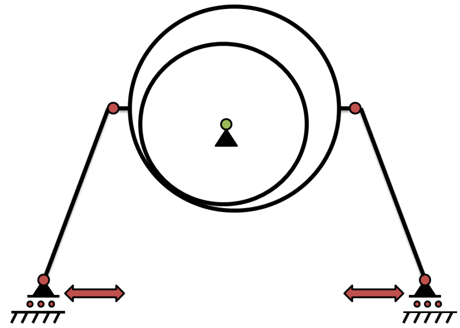

Fig. 8. Proposed alteration to three-ring reducer system. The depicted revolute joints have a limited range of motion, and could be replaced by flexible hinges.

An interesting observation is the fact that a class is defined in which none of the existing speed reducer mechanisms can be fitted. A nutating motion where the skewed axis does not rotate could be a novel way of achieving a speed reduction. Especially for designing a (partially) compliant speed reducer system this motion type is very desirable since it does not rely on a full rotation of the main axis.

For both this novel nutating principle and the proposed compliant ring reducer a way of obtaining the desired input motion has to be developed. The two inputs (figure 8) should translate in a coordinated manner with a phase difference between the inputs, resulting in a circular motion of the ring. Micro wobbling motors have been encountered using the same type of motion [40] [41].

Alternative compliant mechanisms can be used for the reciprocating part of the pulsating transmission. For example an Xr-joint, consisting of two cylinders connected via a thin band can be used to obtain a ratio between two limited rotation joints. Also a displacement amplifying compliant mechanism as discussed in the introduction could be used as a reciprocating mechanism. In this way the limited motion of a DaCM would be combined with a mechanism that rectifies the output motion resulting in a fully rotational output.

Various ways of compliant rectifying mechanisms are found in literature [42] which are directly applicable in the pulse transmission. Micro motors using reciprocating motion from electrostatic comb-drive actuators have been encountered [43]. A similar approach could lead to a (partially) compliant speed reducer mechanism.

Ratcheting mechanisms are subjected to sliding contact resulting in friction losses in the system. Compliant ratcheting mechanisms also have sliding contact, hence a frictional loss. Especially when multiple reciprocating systems in series are used these frictional losses cannot be ignored in the pulse transmission concept.

A fully monolithic speed reducer mechanism is not encountered in literature. This only makes sense since all of the encountered speed reducer mechanisms rely on rigid body mechanics. In order to design a full monolithic speed reducer mechanism different principles will have to be developed. A monolithic speed reducer mechanism would be beneficial for fabrication since no assembly would be required.

V. Conclusion

An overview of speed reducer systems is presented and the feasibility of converting each system into a (partially) compliant mechanism is discussed. The classification is based on the type of motion observed in the system. Additionally the speed reducer systems are analysed on several criteria needed for a compliant micro speed reducer system. After eliminating the infeasible speed reducer systems two candidates remained showing potential for (a partial) conversion into a compliant counterpart.

References

[1] Sridhar Kota, Jinyong Joo, Zhe Li, Steven M. Rodgers, and Jeff Sniegowski. Design of compliant mechanisms: Applications to mems. *Analog Integr. Circuits Signal Process.*, 29(1-2):7–15, 2001.

[2] Larry L. Howell. *Compliant Mechanisms*. John Wley & Sons, Inc, New York, 2001.

[3] B. A. Salamon and A. Midha. An introduction to mechanical advantage in compliant mechanisms. *Journal of Mechanical Design*, 120(2): 311–315, 1998.

[4] Just L. Herder. Some considerations regarding statically balanced parallel mechanisms (sbpm's). In *Proceedings of the workshop on fundamental issues and future research directions for parallel mechanisms and manipulators*.

[5] Mark Schenk and Simon D Guest. On zero stiffness. *Proceedings of the Institution of Mechanical Engineers, Part C: Journal of Mechanical Engineering Science*, 2013.

[6] Girish Krishnan and G. K. Ananthasuresh. Evaluation and design of displacement-amplifying compliant mechanisms for sensor applications. *Journal of Mechanical Design*, 130(10): 102304–102304, 2008.

[7] Sudarshan Hegde and G. K. Ananthasuresh. A spring-mass-lever model, stiffness and inertia maps for single-input, single-output compliant mechanisms. *Mechanism and Machine Theory*, 58(0):101–119, 2012.

[8] AB Bhaskar, Girish Krishnan, N Shamsudhin, and GK Ananthasuresh. Design, fabrication, and tetsing of a mesoscale accelerometer made of spring steel. *Journal of the Instrumentation Society of India*, 39(1):46–52, 2009.

[9] Choi Kee-Bong, Hyun-Woo Lee, and Kim Min Young. Cartwheel flexure-based compliant stage for large displacement driven by a stack-type piezoelectric element. In *Control, Automation and Systems, 2007. ICCAS '07. International Conference on*, pages 2754–2758.

[10] M. Dinesh and G. K. Ananthasuresh. Micro-mechanical stages with enhanced range. *International Journal of Advances in Engineering Sciences and Applied Mathematics*, 2(1-2):35–43, 2010.

[11] P. R. Ouyang, R. C. Tjiptoprodjo, W. J. Zhang, and G. S. Yang. Micro-motion devices technology: The state of arts review. *The International Journal of Advanced Manufacturing Technology*, 38(5-6):463–478, 2008.

[12] John A. Kennedy, Larry L. Howell, and William Greenwood. Compliant high-precision e-quintet ratcheting (cheqr) mechanism for safety and arming devices. *Precision Engineering*, 31(1): 13–21, 2007.

[13] J. J. Sniegowski and E. J. Garcia. Surface-micromachined gear trains driven by an on-chip electrostatic microengine. *Electron Device Letters, IEEE*, 17(7):366–368, 1996.

[14] Ping Yang and NingBo Liao. Surface sliding simulation in micro-gear train for adhesion problem and tribology design by using molecular dynamics model. *Computational Materials Science*, 38(4):678–684, 2007.

[15] Matthew S Moses, M Kendal Ackerman, and Gregory S Chirikjian. Origami rotors: Imparting continuous rotation to a moving platform using compliant flexure hinges. In *ASME 2013 International Design Engineering Technical Conferences and Computers and Information in Engineering Conference*, pages V06BT07A037–

V06BT07A037. American Society of Mechanical Engineers.

[16] A Schiltz. A review of planar techniques for multichip modules. *Components, Hybrids, and Manufacturing Technology, IEEE Transactions on*, 15(2):236–244, 1992.

[17] C. Pan. Calculation of speed ratio of two-stage helical gear reducer for minimum mass. volume 274, pages 149–152. 2013.

[18] M. A. Gonzlez-Palacios and J. Angeles. The design of a novel mechanical transmission for speed reduction. *Journal of Mechanical Design, Transactions of the ASME*, 121(4):538–543, 1999.

[19] S. P. Bai and J. Angeles. The design of a gearless pitch-roll wrist. In *Robotics and Automation, 2005. ICRA 2005. Proceedings of the 2005 IEEE International Conference on*, pages 3213–3218.

[20] Long Chang Hsieh and Tzu Hsia Chen. On the design of planetary gear reducer with simple planet gears. *Applied Mechanics and Materials*, 284:867–871, 2013.

[21] D. R. Salgado and J. M. Del Castillo. Analysis of the transmission ratio and efficiency ranges of the four-, five-, and six-link planetary gear trains. *Mechanism and Machine Theory*, 73: 218–243, 2014.

[22] Wisam M Abu-Jadayil and Mousa S Mohsen. Design and manufacturng of self actuating traction drives with solid and hollow rollers. *EDITORIAL BOARD*, 4(4):467, 2010.

[23] Hisashi Machida and Yasuo Murakami. Development of the powertoros unit half toroidal cvt. *Motion and Control*, (9):15–26, 2000.

[24] Lapitsky. Bevel gear differential, April 1975. URL `http://www.freepatentsonline.com/3874251.html`.

[25] Xin-Bo Chen, Bin Wang, Mei-fang Chen, and Yan Li. An innovative speed reduction mechanism with self-adaptability to variable transmission angles. *Mechanism and Machine Theory*, 48(0):41–51, 2012.

[26] Yuan Song, Qizheng Liao, Shimin Wei, Lei Guo, and Lifeng Zhou. A novel approach to design a pure rolling cycloid reducer with involute teeth superimposed. In *Modelling, Identification & Control (ICMIC), 2012 Proceedings of International Conference on*, pages 998–1003. IEEE.

[27] Toshihiro Yukawa and Masaharu Kaneko. Mechanisms of a cyclo gear reducer with several gear ratios. In *SICE Annual Conference (SICE), 2012 Proceedings of*, pages 2274–2279. IEEE.

[28] H. Sasaki, T. Masuyama, and T. Takahashi. Development of a low backlash crown reducer. pages 1384–1389.

[29] Zihni B. Saribay and Robert C. Bill. Design analysis of pericyclic mechanical transmission system. *Mechanism and Machine Theory*, 61 (0):102–122, 2013.

[30] G. Wang, L. Li, H. Guan, and T. Guan. Modeling and simulation for nutation drive with rolling teeth. volume 538-541, pages 470–473. 2012.

[31] W. K. Nam, J. W. Shin, and S. H. Oh. Design of thin plate-type speed reducers using balls for robots. *Journal of Mechanical Science and Technology*, 27(2):519–524, 2013.

[32] H. Terada. The development of gearless reducers with rolling balls. *Journal of Mechanical Science and Technology*, 24(1):189–195, 2010.

[33] Qing Bin Tong, Chao Qun Jiao, Tao Ning, and Xiao Dong Zhang. Harmonic gear reducer transmission error analysis and detection. *Advanced Materials Research*, 711:375–380, 2013.

[34] Feng Guan, Chuanxi Zhou, and Qingshi Huang. An innovative planetary gear reducer with overcoming the" dead point". *Open Mechanical Engineering Journal*, 7, 2013.

[35] Y. Liu and Y. Wei. The performance study of three-ring gear reducer. volume 605-607, pages 1261–1264. 2013.

[36] X. Liang, B. Chen, and G. Xu. The research of the reducer based on r-s-r mechanism. pages 352–354.

[37] Jiandong Sun, Wenyu Fu, Hong Lei, E. Tian, and Ziping Liu. Rotational swashplate pulse continuously variable transmission based on helical gear axial meshing transmission. *Chinese Journal of Mechanical Engineering*, 25(6): 1138–1143, 2012.

[38] Qin Hong Chen, Dong Ming Sun, De Hua Zhao, Gui Rong Kang, and Jian Sun. Kinematics analysis of morse cvt input mechanism. *Applied Mechanics and Materials*, 477:384–387, 2014.

[39] Nader Jalili, John Wagner, and Mohsen Dadfarnia. A piezoelectric driven ratchet actuator mechanism with application to automotive engine valves. *Mechatronics*, 13(89):933–956, 2003.

[40] S. De Cristofaro, C. Stefanini, N. Ng Pak, E. Susilo, M. C. Carrozza, and P. Dario. Electromagnetic wobble micromotor for microrobots actuation. *Sensors and Actuators A: Physical*, 161(12):234–244, 2010.

[41] T. Furuhata, T. Hirano, L.H. Lane, R.E. Fontana, L.S. Fan, and H. Fujita. Outer rotor surface-micromachined wobble micromotor. In *Micro Electro Mechanical Systems, 1993, MEMS'93, Proceedings An Investigation of Micro Structures, Sensors, Actuators, Machines and Sys-*

tems. IEEE., pages 161–166. IEEE, 1993.

[42] Gregory M. Roach and Larry L. Howell. Evaluation and comparison of alternative compliant overrunning clutch designs. *Journal of Mechanical Design*, 124(3):485–491, 2002.

[43] Phuc Hong Pham, Dzung Viet Dao, Lam Bao Dang, and Susumu Sugiyama. Single mask, simple structure micro rotational motor driven by electrostatic comb-drive actuators. *Journal of Micromechanics and Microengineering*, 22(1): 015008, 2012.

VI. Appendix

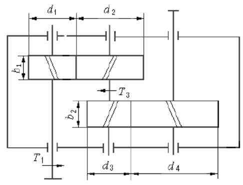

Fig. 9. fixed (compound) gears [17]

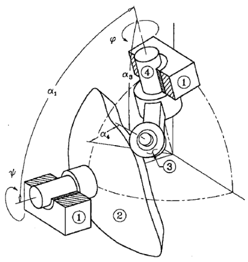

Fig. 10. rolling cam reducer [18]

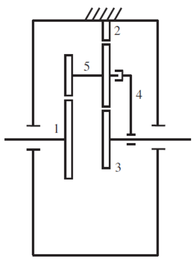

Fig. 11. (compound) planetary gear [21]

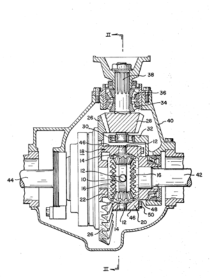

Fig. 12. (gearless) differential gear [24]

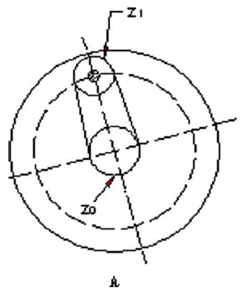

Fig. 13. belt/chain drive [25]

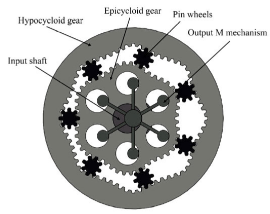

Fig. 14. cycloid reducer [26]

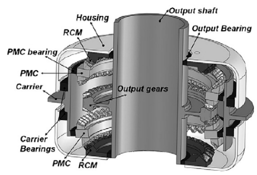

Fig. 15. nutating reducer [29]

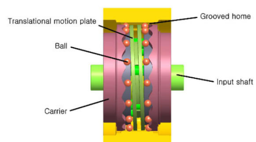

Fig. 16. rolling balls reducer [31]

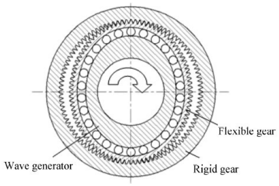

Fig. 17. harmonic reducer [33]

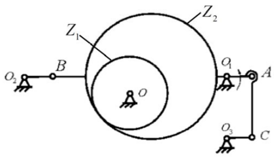

Fig. 18. (three-)ring reducer [34]

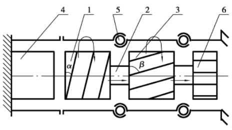

Fig. 19. R-S-R reducer [36]

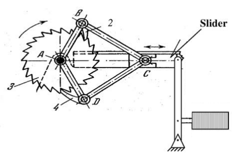

Fig. 20. pulse transmission [39]

INTERMEZZO

In the previous section two speed reducer mechanisms with features suitable for a micro version were identified. Both have the potential to be (partially) compliant, resulting in a mechanism more suited for a micro scale. Both are planar mechanisms and therefore planar micro manufacturing techniques are applicable. One of the two mechanisms has more favourable attributes over the other when considering the application, a mechanical wristwatch. This section will discuss the advantages of the '(three-) ring reducer' mechanism over the 'pulse transmission' and why this concept selected for further development.

Well-defined gear ratio As mentioned in the introduction the gear train of a mechanical wristwatch has two purposes. The first key role is the kinematics of the transmission; the indicators have to be driven with a precise speed to show the correct time. For this purpose the transmission ratio needs to be fixed precisely. The transmission ratio of the ring reducer mechanism is clearly defined by the gear pair. The pulse transmission relies on a length of a lever arm, rather than a fixed integer in the form of number of gear teeth. In addition to this the ring-reducer has better potential to be used as a speed increaser than the pulse transmission, which is required for application in a mechanical wristwatch.

Clear rotation as input The input motion of the ring reducer is clear; the main spring will be attached to the sun gear which drives the ring gear. For the pulse transmission however a mechanism is needed to drive the reciprocating motion. In the macro version of the pulse transmission this motion is acquired by the use of a cam mechanism[2].

Reported efficiencies Planetary gear transmission mechanisms are known for their efficiency and high reduction ratio in a small volume[3]. The ring reducer is a special case of a planetary gear transmission. Efficiencies of 93% are reported for the ring reducer[4]. Efficiencies as high as 97.4% are reported, depending on the type of lubrication used[5].

II

Thesis design paper

Reciprocating Geared Mechanism With Compliant Suspension

J. Wessels[1], D. Farhadi Machekposhti[1], N. Tolou[1], G. Semon[2], and J.L. Herder[1]

[1]Department of Precision and Microsystems Engineering,
Delft University of Technology, Delft, The Netherlands
[2]Department of Research and Development, TAG HEUER, La Chaux-de-Fonds, Switzerland

***Abstract*—We present a novel cycloidal geared mechanism with a continuous rotational input and featuring a reciprocating translational output. A statically balanced compliant mechanism suspends an annulus, driven by a cycloidal rotor. The Freedom and Constraint Topologies (FACT) design method is used to synthesize the compliant suspension. A fixed transmission ratio of 15 results from the ratio between the cycloidal rotor and annulus. The static balancing conditions of the suspension is shown analytically, and validated using Finite Element Modelling (FEM) and experimental results. Moreover, the estimation of the frictional loss as a function of the stiffness of the compliant members is derived using a force analysis of the system, and verified using experimental data. A case study on a mechanical watch yields dimensions for the prototype, fabricated in silicon using Deep Reactive Ion Etching (DRIE). Experiments show that energy loss as a function of the stiffness of compliant members is marginal, and independent of the position of the compliant suspension.**

***Index Terms*—gear mechanism, monolithic, MEMS, compliant mechanism, transmission**

I. Introduction

SPEED ratio mechanisms are widely applied in mechanical devices to achieve a mechanical advantage. Often speed reduction mechanisms are paired with electrical motors to increase the output torque by reducing the high rotational speed of the motor output. Other applications require speed increaser mechanisms to increase the output speed by decreasing the mechanical advantage. Some key factors characterizing speed ratio mechanisms are efficiency, transmission ratio, and maximum carrying load. Speed ratio mechanisms are used in applications on a scale ranging from meters to micrometers.

An example of a micro speed increaser mechanism is the gear train of a mechanical watch, which is used as the subject for a case study. The gear train consists of several stages of compound gears, suspended by micro bearings to achieve a transmission ratio, complicating miniaturization of the system[1]. A thinner system consisting of fewer parts is desired to further reduce the size of the wristwatch.

Therefore a literature review on speed ratio mechanisms was performed and a classification aiming at miniaturization of these mechanisms was provided. Goal of the literature review was to identify speed ratio mechanisms eliminating the need for micro bearings. Most of the encountered speed ratio mechanisms rely on a large number of moving parts[2–5], like in the mechanical watch, and are not suited for miniaturization[6–9].

A speed ratio mechanism achieving a high ratio in a compact form is a cycloidal drive, sometimes referred to as a wobbling drive because of its distinct motion principle[10]. High efficiencies have been reported for low-speed high-torque applications[11]. Several different cycloidal drive configurations have been encountered, including one that replaces the eccentric bearing with a parallelogram linkage to achieve a wobbling motion[12, 13]. A schematic of this mechanism is presented in section II.

Monolithic mechanisms address problems concerning assembling mechanisms on a micro scale[14]. Compliant mechanisms have been widely adopted in precision mechanisms to eliminate problems as backlash, wear, need for lubrication, and repeatability[14]. These one-piece mechanisms are preferred for miniaturization to traditional rigid body mechanisms. Monolithic mechanisms have an inherent problem of complicating a full rotation; motions are restricted to deflection of flexural beams. However, part of the aforementioned cycloidal drive translates over a circular path; a motion a compliant mechanism can facilitate.

Compliant mechanisms rely on deformation of elastic members for which energy is needed[15]. However, energy stored inside the mechanism cannot benefit the mechanical advantage of the mechanism[16]. To achieve an optimal energy transmission from the input to the output of the system, the energy stored inside the system should remain constant. Mechanisms with a constant potential energy are called statically balanced mechanisms[17].

The fields of compliant mechanisms approaches the field of speed ratio mechanisms in the form of compliant displacement amplifiers[15, 18]. However all of the compliant displacement amplifiers have a limited translational input, while all encountered speed ratio mechanisms are based on a full cycle rotational input[2–9]. Consequently speed ratio mechanisms increase the frequency of the input rotation, while displacement amplifiers solely increase the translational range of motion of the mechanism. Also compliant mechanisms are often delicate precision mechanisms, and seem to contradict the robust nature of speed ratio mechanisms. A mechanism with a full cycle rotational input, and able to transfer the forces to a reciprocating translational output, bridges the gap between these two fields.

This paper introduces a cycloidal geared compliant motion conversion mechanism and presents the methodology used to reach the novel design. Key features that distinguish this compliant cycloidal drive mechanism from traditional ones are simulated and verified using measurements. A case study on implementation in a mechanical watch is used for dimensional design of the mechanism. The designed mechanism, however, can be applied on a broader field of micro transmission mechanisms and micro motors[19].

The novel reciprocating geared mechanism with compliant suspension will be presented in section II. Test results verifying key aspects of a compliant gear mechanism can be found in section III and will be discussed in section IV. Conclusions based on aforementioned results are given in section V.

II. Methods

A speed ratio mechanism is identified having features beneficial for miniaturization, see fig. 1. The motion principle consists of a gear rotating about a central input axis, and a ring gear translating over a circular path by means of a parallelogram linkage. By removing the parallelogram linkage in the original design[12, 13], and replacing it by a compliant suspension, this mechanism has potential for miniaturization. As such, the problematic full rotation can be eliminated by utilizing a moving contact point between a rotating input gear, and an output gear translating over a circular path. This novel motion conversion mechanism has a rotational input and a reciprocating translational output. The key functionality of the parallelogram is identified as a base for the design process of the compliant suspension.

Criteria are determined for application in a mechanical watch as a case study. The novel gear mechanism is to be driven directly by the barrel gear, the first gear and power reserve of a mechanical watch.

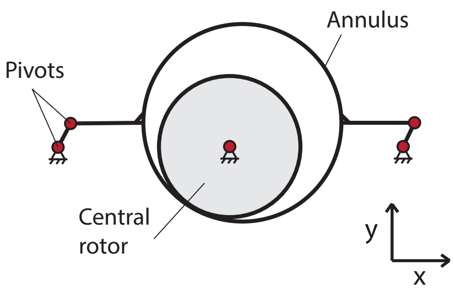

Fig. 1. Schematic of ring reducer concept as presented in literature[12, 13]. Parallel crank mechanism is used to obtain a circular translation motion.

The compliant suspension should be resistant of an applied moment of 9Nmm. Except for the central axis of the input gear no other axes/bearings are allowed in a planar design space with a diameter of 29mm (diameter of the mechanical wristwatch). The central part of this design space is occupied by the barrel gear itself. A transmission ratio higher than 12 is desired, since this would exceed the maximum achievable ratio of the current transmission mechanism in a mechanical watch. A low power loss compared to the power throughput of the system is required. And a constant energy transmission, independent of the position of the suspension, is needed to guarantee the functionality of the watch.

A. Suspension design

1) FACT method: Following the Freedom and Constraint Topology (FACT) method[20] the topology for the compliant suspension is established. The design criteria are formulated as a desired freedom topology for the annulus: a planar 2T (2 translational) mechanism. The FACT method links the desired freedom topology to a specific constraint topology. In the case of a 2T freedom topology the only resulting constraint topology is a serial flexure mechanism consisting of two perpendicular translational stages connected via a rigid intermediate stage. The minimal flexure count to achieve a 1T mechanism is two. Therefore the 2T suspension will consist of four flexural beams, connected via a rigid intermediate stage, see fig. 2(a).

2) Statically balanced: The output of the system is affected by a frictional loss between gears and an internal stiffness of the suspension. Like regular gear pairs energy is lost due to friction, often this term is constant over a cycle. However, a non-constant contact force due to a compliant suspension can cause a fluctuation in the energy loss during each cycle. Additionally energy is stored and released in the flexural members, yielding a varying potential energy of the system. As a result the output force will depend

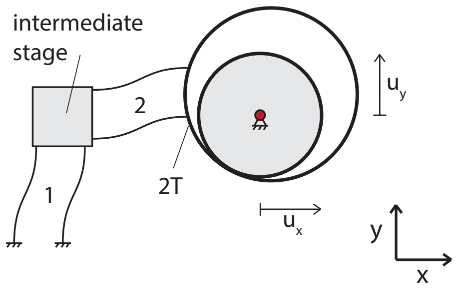

(a) Conceptual design replacing parallel cranks with a 2T compliant mechanism synthesized using FACT method. Translational parallel flexures 1 and 2 are connected via an intermediate stage to obtain a 2T suspension.

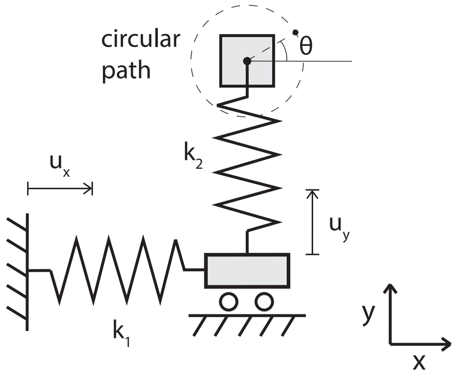

(b) Simplified model of the compliant suspension. k_1 and k_2 represent the combined linear stiffnesses of respectively parallel flexural stages 1 and 2.

Fig. 2. Conceptual design of compliant gear mechanism based on original ring reducer mechanism, see fig. 1.

on the position of the compliant suspension, hence the mechanical advantage will be affected.

A statically balanced mechanism is needed to obtain a constant output force; if the energy stored inside the suspension is constant, the input force is transferred to the output of the mechanism directly rather than being stored and released. As a result there will be no energy fluctuation on the transmission due to energy stored in the suspension.

Fig. 2(b) shows a simplified model of the suspension to approximate the strain energy level of the suspension during operation. The circular displacement of the suspension is dictated by the cycloidal profile, see section II-B. The translational range of motion is characterized by eccentricity parameter e, determining the output motion u_x of the intermediate stage:

$$u_x = e\cos(\theta) \tag{1}$$

$$u_y = e\sin(\theta) \tag{2}$$

For small deflections the strain energy in the flexible beams, represented by springs with linear stiffness k_1 and k_2, can be described as:

$$U_1 = \frac{1}{2}k_1 u_x^2 = \frac{1}{2}k_1 e^2 \left(\cos\theta\right)^2 \tag{3}$$

$$U_2 = \frac{1}{2}k_2 u_y^2 = \frac{1}{2}k_2 e^2 \left(\sin\theta\right)^2 \tag{4}$$

Note that these springs have an initial length of zero and exert no initial force, which is a valid assumption for flexible beams without pre-loading.

The sum gives the total strain energy stored in the system. For $k_1 = k_2 = k$ this results in a constant energy level, independent of the angle θ:

$$U_{total} = U_1 + U_2 = \frac{1}{2}ke^2\left(\left(\cos\theta\right)^2 + \left(\sin\theta\right)^2\right) \tag{5}$$

$$= \frac{1}{2}ke^2 \tag{6}$$

An identical stiffness profile is expected in all radial directions in the case of k_1 being equal to k_2.

Stiffness k scales to the power 3 with respect to thickness t. To reduce the influence of fabrication errors on the static balancing performance, the length l and thickness t for the flexural members in both translational stages is chosen identical. Any fabrication errors will influence the stiffness of both translational stages equally, hence static balancing will not be compromised. The stiffness k can be estimated using linear beam theory, assuming a rectangular cross-section for the flexural beams:

$$k = E\frac{wt^3}{l^3} \tag{7}$$

Where E is the Young's modulus of the material, and w the width of the flexure.

B. Rotor profile design

A cycloidal gear profile has several key advantages: high ratio without interfering gear teeth, high reported efficiencies, no possibility of losing contact and skipping teeth. The efficiency of cycloidal speed reducers is dominated by the frictional losses[9, 21], which is dominated by the contact force between the gears. A general expression for the cycloidal profile used in cycloidal drives has been established, including all practical restrictions to avoid undercutting and interfering parts[22]. These models are derived and validated for traditional cycloidal drive mechanisms, including revolute joints and eccentric cams. However, reaction forces due to the stiffness of a compliant mechanism are not incorporated, hence will be discussed in this section.

Generally a cycloidal profile can be expressed based on four parameters: the radius of the pitch circle of the central rotor R; the eccentricity e of the center of the rotor to the input shaft; the radius of the (fused) rollers on the ring R_r; and the number of (fused) rollers on the annulus N[23]. Eq. (8) shows the expressions for the position vector C from the center to the circumference of the cycloidal profile [23].

$$\begin{bmatrix} C_x \\ C_y \end{bmatrix} = \begin{bmatrix} R\cos\phi - R_r\cos(\phi-\psi) - e\cos((N)\phi) \\ -R\sin\phi + R_r\sin(\phi-\psi) + e\sin((N)\phi) \end{bmatrix} \tag{8}$$

Where ψ represents the relative angle of the rollers with radius R_r unrolling on the pitch circle of the rotor with radius R, defining the cycloidal profile:

$$\psi = -\arctan\left[\frac{\sin((1-N)\phi)}{R/eN - \cos((1-N)\phi)}\right] \tag{9}$$

$$\text{for} \quad (0^\circ \leq \phi \leq 360^\circ)$$

Additional constraints applied on these general equations ensure a cycloidal profile without undercutting or interference between parts[22].

The ratio r_i depends on the number of teeth of the cycloidal rotor and annulus, see eq. (10), where N_{rotor} represents the number of lobes on the cycloidal rotor and N represents the number of (fused) rollers on the annulus. High ratios are obtained for a small difference in the number of teeth.

$$r_i = \frac{N - N_{rotor}}{N_{rotor}} \tag{10}$$

1) Frictional loss: The addition of a stiffness to a gear pair results in increased frictional losses due to an increase in normal force F_n, depicted in fig. 3. The magnitude of the contact force depends on the (constant) reaction force of the suspension, which is the result of stiffness k and eccentricity e. The reaction force from the suspension F_s is assumed to be directed towards the center of the cycloidal rotor, see fig. 3. The angle of contact between the gear pair affects the normal force F_n, and is a function of the gradient of the cycloidal profile. Using a Coulomb friction coefficient μ, the friction force F_{fr} on every position of the cycloidal profile can be determined, see eq. (11). Note that the friction force F_{fr} is in line with shear force F_{sh}, but with different magnitude, fig. 3. Multiplying this friction force F_{fr} with the corresponding moment arm R_{fr} yields the resulting moment about the central axis.

Integrating the friction loss over the circumference of the cycloidal profile provides an estimation of the energy loss due to friction per cycle. The circumference C of the cycloidal profile is characterized by eq. (8).

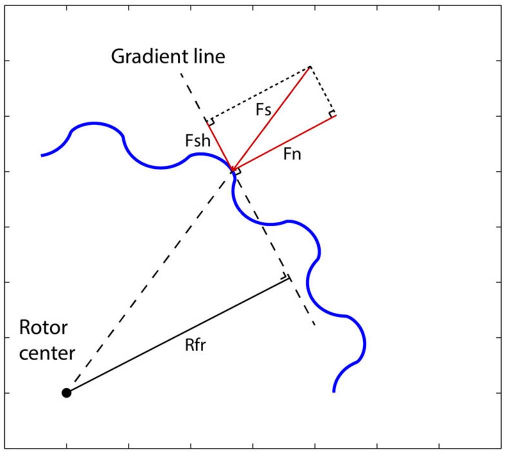

Fig. 3. Normal force F_n depends on the contact angle on the cycloidal rotor with the suspension reaction force F_r pointed at center of cycloidal rotor. Friction coefficient μ determines the magnitude of frictional force F_{fr}, collinear with F_{sh}. The friction force F_{fr} is used to calculate the expected no-load resisting moment.

$$W_{Loss} = \int_0^{2\pi} \underbrace{F_n \cdot \mu}_{F_{fr}} \cdot R_{fr}(\phi) \cdot \delta C(\phi) d\phi, \tag{11}$$

C. Prototype

A prototype is fabricated in silicon using deep reactive-ion etching (DRIE), shown in fig. 4. The flexural members have a thickness of 20μm and a height of 525μm, verified using a Scanning Electron Microscope (SEM) with a tolerance of $\pm 1.5\mu$m, see fig. 5. The prototype is designed to verify the radial stiffness and measure the no-load quasi-static driving torque of the system.

Friction coefficients for silicon vary depending on the conditions[24, 25]. A friction coefficient $\mu = 0.3$ is assumed for the contact between the cycloidal rotor and annulus, based on experience in micro fabrication of previous prototypes. The parameters of the cycloidal rotor are $R = 5.2$mm; $e = 0.295$mm; $R_r = 0.6$mm; $N = 16$, resulting in a transmission ratio of $r_i = 15$ for a single tooth difference according to eq. (10). A 10μm gap between gears ensures that the rotor is not interfering with the annulus. The friction loss W_{Loss} as a result of the stiffness of the suspension is less than 1% of the available input energy per cycle according to eq. (11), assuming a constant input moment of 9Nmm.

D. Experimental setup

Two experiments are done to evaluate two features of the prototype. The first experiment aims at verifying a statically balanced suspension by performing a

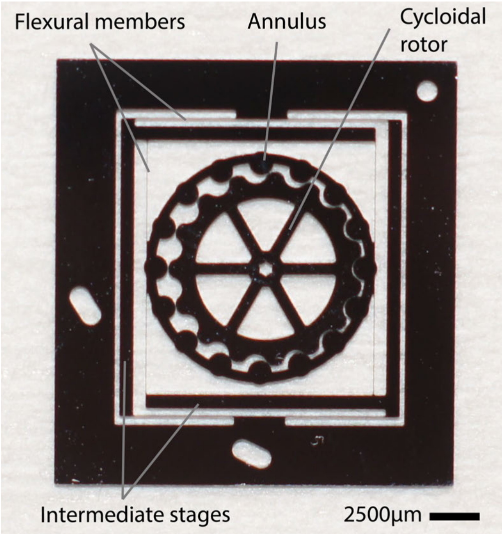

Fig. 4. Top-view of prototype indicating the main components. The mirrored suspension consists of 8 flexural members, connected via 2 separate intermediate stages. The end-effector of this suspension is an annulus, fitted on the cycloidal rotor. All eight flexural members have a length $l = 5$mm and thickness $t = 20\mu$m.

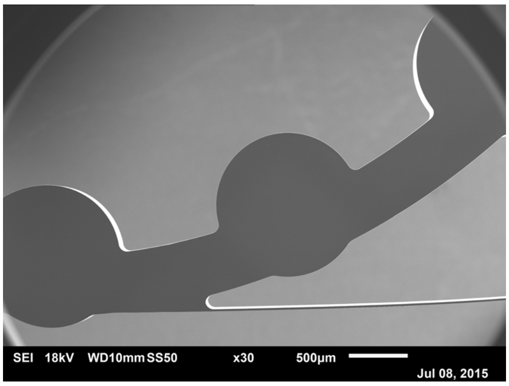

Fig. 5. Close-up of DRIE silicon prototype using Scanning Electron Microscope (SEM). Flexural members are inspected with a measurement tolerance of $\pm 1.5\mu$m.

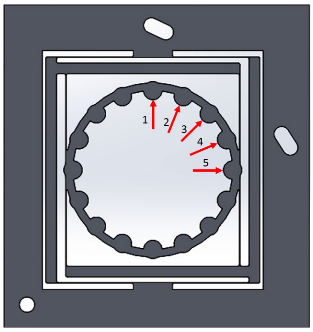

Fig. 6. Measurement positions and directions for Force-Deflection experiment. The force sensor is rotated and re-aligned with the prototype using manual precision stages between measurement positions. Measurements for each direction are repeated 5 times.

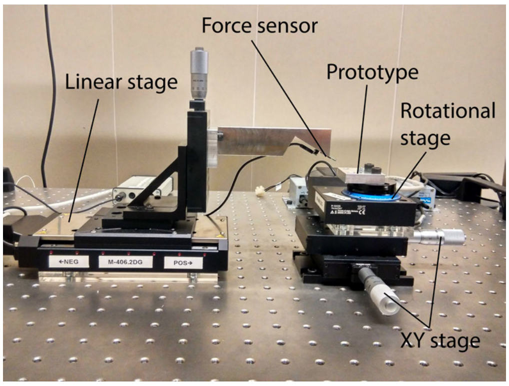

Fig. 7. Force-deflection setup indicating the components. The prototype is manually positioned using the XY stage and rotated with respect to the force sensor for each measurement direction.

force-deflection measurement for different directions. The second experiment verifies the motion principle, and verifies the frictional loss as a result of the suspension stiffness by performing a no-load torque measurement.

1) Force-deflection: The stiffness of the suspension is measured in 5 directions, shown in fig. 6, using a force sensor (*FEMTO FT-S10000*) with a resolution of 0.5μN. The force sensor tip is actuated using a precision linear stage (*Physik Instrumente M-406.2DG*) with a resolution of 8.5nm. The sensor is aligned with the prototype using a rotational stage (*Physik Instrumente M-060.2DG*) with a resolution of 2.1μrad. Aforementioned components are positioned using two manual precision translational stages (*Thorlabs PT1*). Between measurements the rotational stage is rotated $\frac{360}{16}$ degrees, after which the sensor is re-positioned and aligned with the prototype. Each force-deflection measurement is repeated 5 times. An identical force-deflection characteristic is expected for all 5 measurement positions.

2) No-load torque: A no-load measurement is performed by driving the central rotor while measuring the resisting moment. The experimental setup consists of two independent XY manual precision stages (*Newport M-406*). One XY stage is used to position the cycloidal rotor with respect to the torque sensor, the other is used to position the annulus with respect to the cycloidal rotor, fig. 8. The positioning accuracy is verified using a microscope with a resolution of 0.5μm. The torque on the axis of the cycloidal rotor is measured using a torque sensor (*TA Instruments AR-G2*) with a resolution of 0.1nNm, and serves as indication of the required torque to drive the system. The cycloidal rotor is driven at low velocity (0.0154rad/s) for a single rotation, and the resulting torque is measured with a sampling rate of 1Hz.

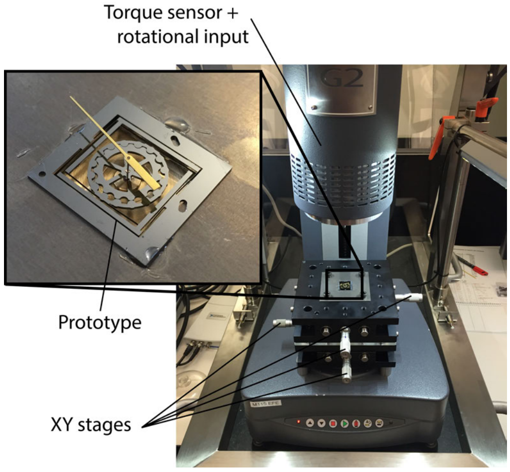

Fig. 8. Setup used to measure the no-load driving moment. An rotational input is applied on the cycloidal rotor, and the resisting moment is measured using a torque sensor.

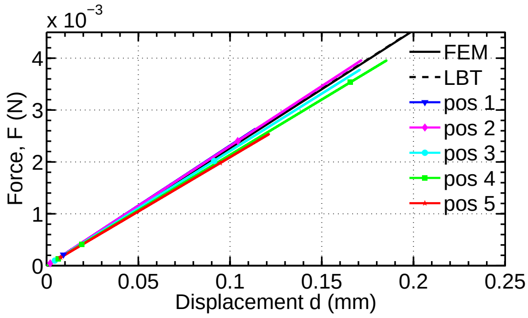

Fig. 9. Force-deflection data compared to finite element modelling (FEM) and linear beam theory (LBT) for 5 measurement positions.

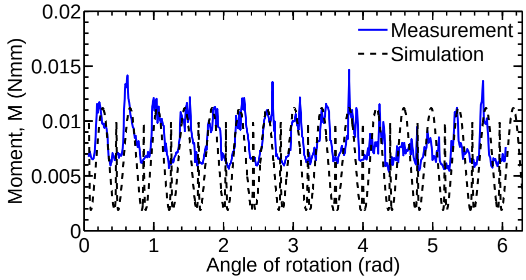

Fig. 10. Results from no-load torque measurement for a full rotation of the cycloidal rotor. An adjusted friction coefficient of $\mu = 0.35$ is used for the simulation. A correction factor of $\frac{16}{15}$, corresponding with the number of lobes and (fused) rollers on respectively the cycloidal rotor and annulus, is used to align the peaks in the simulated results with peaks in the measured data.

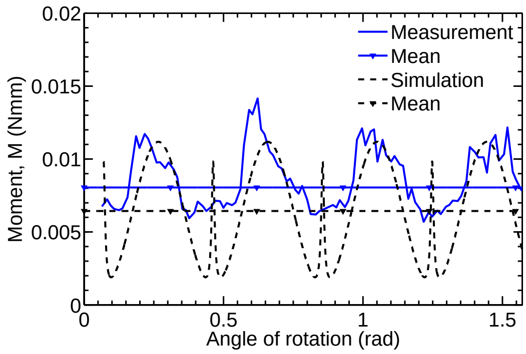

Fig. 11. Results from no-load torque measurement for a quarter rotation on the cycloidal rotor. The mean of both the simulation and measurements is provided as an indication of the lost energy.

III. Results

A. Force-deflection measurement

The data of the 5 force-deflection measurements is plotted and compared to the FEM and LBT simulations in fig. 9 to analyse the static balancing performance.

The experimental data shows a linear correlation between the reaction force and displacement for all 5 measurement positions $\left(R^2 > 0.99, p < 0.001\right)$, indicating a linear stiffness k, see table I.

TABLE I
Measured stiffness per measurement direction; Coefficient of determination (R^2)

Position	stiffness k [N/mm]	R^2
1	0.02318	0.995
2	0.02307	0.996
3	0.02211	0.999
4	0.02135	0.999
5	0.02091	0.999

B. No-load torque measurement

The data from the no-load measurement is compared to the expected torque as a result of the friction component for a full rotation in fig. 10. A correction factor of $\frac{16}{15}$ is used to scale the simulation results to include the gear ratio, resulting in 16 peaks for both the simulation and measured plot, see fig. 10. The friction coefficient μ is the only uncertain factor in the model. For a better fit between simulations and measurements the μ is adjusted from 0.3 to 0.35 in the model.

The area under the plotted graph indicates the lost work, visualized by the mean of the simulated and experimental data, see fig. 11.

IV. Discussion

A. Force-deflection measurement

A perfectly statically balanced suspension would yield an equal stiffness in all directions. The measurements show a 9.78% discrepancy between the lowest and highest stiffness between measurement positions, resulting in a difference in contact force between the gears, see table I. As a result of this imbalance in the suspension, a fluctuation in the output torque is expected, however this pattern is not recognized in fig. 10.

The difference in stiffness can be partly explained by a small difference in flexure length induced by not including a correction for fillets on the flexural beams. This length difference can explain 3% of the observed stiffness difference. Another explanation is a variation in thickness between the flexural beams in x- and y-direction as a result of a directional dependent fabrication error. This cannot be confirmed since this variation would lie within the $\pm 1.5\mu$m margin of error of the SEM measurement itself.

As a result of the etching process the thickness of the flexible beams varies, especially in the in-plane direction. Instead of a rectangular cross-section, the beams have a trapezoidal profile, affecting the moment of inertia. A trapezoidal cross-section with 17.5μm and 22.5μm for respectively the thinnest and thickest section of the flexural component gives an increase in stiffness of 1.5% with respect to the rectangular cross-section with a constant (averaged) thickness of 20μm.

The stiffness of the suspension is highly sensitive to fabrication errors. An increase in thickness t of 1μm for flexural members with an initial thickness $t = 20\mu$m results in 16% stiffness increase. Thicker flexural components will help reduce the sensitivity to fabrication errors, however this will yield higher stiffness and stresses in the material for equal displacement. Although a 9.78% discrepancy is observed between the highest and lowest measured stiffness, see fig. 9, the variation between measured directions is small compared to the discrepancy with the simulation due to fabrication errors. This observation substantiates the decision to use equal thickness flexural members to reduce the effect of fabrication errors. The stiffness in x- and y-direction has been equally affected by the inaccurate fabrication, still resulting in an almost statically balanced suspension.

B. *No-load torque measurement*

The torque measurement and simulation data show the same behaviour and order of magnitude for the driving torque, see fig. 10. A fabrication error of 4μm for DRIE on the cycloidal rotor parameters cannot account for the observed difference. The only remaining factor to influence the frictional loss model is the friction coefficient μ. The measured torque indicates a friction coefficient higher than the assumed value of 0.3. The corrected value of 0.35 for μ for silicon is within the range provided in literature[24, 25]. Different materials could improve the efficiency, e.g. coating of rotor surface to reduce friction and wear. Materials with a lower Young's modulus will have a lower reaction force due to deformation, hence lower frictional losses.

The sharp peaks in the simulation, corresponding with the valleys of the cycloidal rotor, are not visible in the measured data. This observation indicates that the assumption of a single contact point is not correct, and that the contact in the valley does not occur. Instead the contact point will skip on higher locations on the cycloidal rotor, which would explain why only the top half of the simulation accurately represents the resulting moment, see fig. 11.

The play in the central bearings of the cycloidal rotor affects the maximum displacement of the suspension. This play needs to be subtracted from the displacement of the suspension, resulting in an lower effective eccentricity for the cycloidal rotor resulting in a lower expected torque fluctuation. This play is neglected in the modelling of the system, but will play a role for low values for the eccentricity e.

The area under the plotted lines in fig. 10 indicates the lost work as a result of the stiffness of the suspension pushing the gears together. Comparing this to the available energy in the form of a constant torque on the cycloidal rotor with a magnitude of 9Nmm, this additional lost work due to the suspension stiffness is negligible, see fig. 10.

The compliant cycloidal drive is described as merely a transmission mechanism. However the mechanism has potential to be used as a micro motor, as others researchers also concluded[19]. By adding actuators to an XY 2-translational mechanism and initiating them in the correct order, Hwang & Higuchi, 2015 achieve a circular path for the ring gear. A full cycle rotation is obtained using two reciprocating translational inputs. A similar function inversion could be done with the mechanism proposed in this paper.

To increase efficiency of the gear contact and still retain a statically balanced system, a negative stiffness suspension could be used for both translational stages. Eq. (6) shows that a negative stiffness would still yield a statically balanced system while eliminating most of the sliding contact, resulting in higher efficiency. However an embodiment satisfying all design criteria lacks.

C. *Future work*

In the case of a mechanical watch a substantial moment is applied in a single direction on the axis of the cycloidal rotor by the barrel spring. To avoid buckling the flexural beams can be oriented such that they are loaded in tension to increase the load-carrying capacity of the system, see fig. 12. Increasing

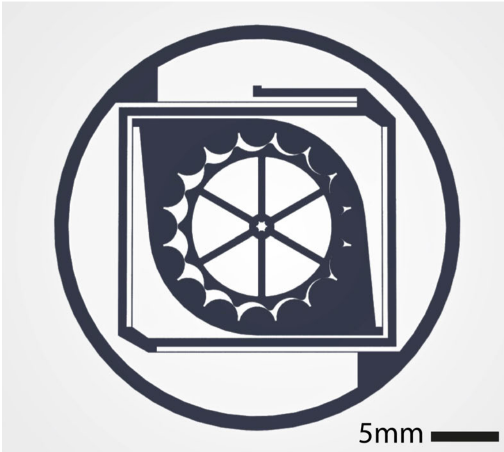

Fig. 12. CAD model including features to improve the torque handling capabilities by loading all flexural components in tension for a clockwise applied moment on the rotor axis. Depicted flexures have a length of $l = 14.3$mm and a thickness $t = 60\mu$m.

the length of the beams results in a lower in-plane stiffness, as well as the possibility to increase the thickness of the beams before running into the stress limit.

Using thicker beams makes the stiffness less sensitive to fabrication errors, since it will have less of an effect on the overall thickness, see fig. 12. Future work will include conducting experiments for conditions such as an applied translational load to the reciprocating output of the system aiming to estimate the efficiency of the reciprocating compliant gear mechanism.

V. Conclusion

A novel reciprocating geared mechanism with compliant suspension featuring a continuous rotational input and a reciprocating translational output was designed, fabricated and tested on a micro scale. A torque fluctuation is eliminated using a statically balanced suspension, resulting in a constant energy transfer. The dissipated energy due to an increased contact force resulting from the suspension stiffness is assessed by a no-load driving torque measurement. For scenarios with a high load this additional energy dissipation can be neglected, showing a potential for further development of reciprocating micro transmission mechanisms.

VI. Acknowledgements

This research is conducted at the instigation of, under the supervision of, and with the close collaboration of TAG HEUER and its General Manager, dr. Guy Semon, and received funding from TAG HEUER. Authors would also like to acknowledge Christian Guichard for creating the test bench.

References

[1] Ruxu Du and Longhan Xie. *The Mechanics of Mechanical Watches and Clocks*. Springer, 2013.

[2] S. P. Bai and J. Angeles. The design of a gearless pitch-roll wrist. In *Robotics and Automation, 2005. ICRA 2005. Proceedings of the 2005 IEEE International Conference on*, pages 3213–3218.

[3] D. R. Salgado and J. M. Del Castillo. Analysis of the transmission ratio and efficiency ranges of the four-, five-, and six-link planetary gear trains. *Mechanism and Machine Theory*, 73: 218–243, 2014.

[4] W. K. Nam, J. W. Shin, and S. H. Oh. Design of thin plate-type speed reducers using balls for robots. *Journal of Mechanical Science and Technology*, 27(2):519–524, 2013.

[5] Qin Hong Chen, Dong Ming Sun, De Hua Zhao, Gui Rong Kang, and Jian Sun. Kinematics analysis of morse cvt input mechanism. *Applied Mechanics and Materials*, 477:384–387, 2014.

[6] Zihni B. Saribay and Robert C. Bill. Design analysis of pericyclic mechanical transmission system. *Mechanism and Machine Theory*, 61 (0):102–122, 2013.

[7] X. Liang, B. Chen, and G. Xu. The research of the reducer based on r-s-r mechanism. pages 352–354.

[8] M. A. Gonzlez-Palacios and J. Angeles. The design of a novel mechanical transmission for speed reduction. *Journal of Mechanical Design, Transactions of the ASME*, 121(4):538–543, 1999.

[9] G. Wang, L. Li, H. Guan, and T. Guan. Modeling and simulation for nutation drive with rolling teeth. volume 538-541, pages 470–473. 2012.

[10] E. Chen and D. Walton. The optimum design of khv planetary gears with small tooth differences. *International Journal of Machine Tools and Manufacture*, 30(1):99–109, 1990.

[11] Jonathon W Sensinger and James H Lipsey. Cycloid vs. harmonic drives for use in high ratio, single stage robotic transmissions. In *Robotics and Automation (ICRA), 2012 IEEE International Conference on*, pages 4130–4135. IEEE.

[12] Xin Li, Weidong He, Lixing Li, and Linda C. Schmidt. A new cycloid drive with high-load capacity and high efficiency. *Journal of Mechanical Design*, 126(4):683–686, 2004. 10.1115/1.1758254.

[13] Ce Zhang, Yimin Song, and Jun Zhang. Review of researches on ring-plate gear reducers with

small tooth number difference. In *12th IFToMM World Congress, France*.

[14] G. K. Ananthasuresh and Larry L. Howell. Mechanical design of compliant microsystems-a perspective and prospects. *Journal of Mechanical Design*, 127(4):736–738, 2005.

[15] Girish Krishnan and G. K. Ananthasuresh. Evaluation and design of displacement-amplifying compliant mechanisms for sensor applications. *Journal of Mechanical Design*, 130(10): 102304–102304, 2008.

[16] B. A. Salamon and A. Midha. An introduction to mechanical advantage in compliant mechanisms. *Journal of Mechanical Design*, 120(2): 311–315, 1998.

[17] Just L. Herder. Some considerations regarding statically balanced parallel mechanisms (sbpm's). In *Proceedings of the workshop on fundamental issues and future research directions for parallel mechanisms and manipulators*.

[18] M. Dinesh and G. K. Ananthasuresh. Micromechanical stages with enhanced range. *International Journal of Advances in Engineering Sciences and Applied Mathematics*, 2(1-2):35–43, 2010.

[19] D. Hwang and T. Higuchi. A planar wobble motor with a xy compliant mechanism driven by shape memory alloy. *Mechatronics, IEEE/ASME Transactions on*, PP (99):1–1, 2015. ISSN 1083-4435. doi: 10.1109/TMECH.2015.2439046.

[20] Jonathan B. Hopkins and Martin L. Culpepper. Synthesis of precision serial flexure systems using freedom and constraint topologies (fact). *Precision Engineering*, 35(4):638–649, 2011.

[21] T Mackic, M Blagojevic, Z Babic, and N Kostic. Influence of design parameters on cyclo drive efficiency. *Journal of the Balkan Tribological Association Vol*, 19(4):497–507, 2013.

[22] Yii-Wen Hwang and Chiu-Fan Hsieh. Determination of surface singularities of a cycloidal gear drive with inner meshing. *Mathematical and Computer Modelling*, 45(34):340–354, 2007.

[23] Joong-Ho Shin and Soon-Man Kwon. On the lobe profile design in a cycloid reducer using instant velocity center. *Mechanism and Machine Theory*, 41(5):596–616, 2006.

[24] Shigehisa Suzuki, Tsukasa Matsuura, Manabu Uchizawa, Shinsuke Yura, Hirosh Shibata, and Hiroyuki Fujita. Friction and wear studies on lubricants and materials applicable to mems. In *Micro Electro Mechanical Systems, 1991, MEMS'91, Proceedings. An Investigation of Micro Structures, Sensors, Actuators, Machines and Robots. IEEE*, pages 143–147. IEEE.

[25] Deng Keren and H. Ko Wen. A study of static friction between silicon and silicon compounds. *Journal of Micromechanics and Microengineering*, 2(1):14, 1992.

III

Chapters

2

Case specific design

The prototype presented in the concept paper is based on a preliminary design of the compliant suspension. Several design features and choices specific to the mechanical watch case are not incorporated in the fabricated prototype. This chapter presents a further improved design for the specific case. The measurements and results presented in the concept paper are unaltered, since an unloaded scenario is tested. In a loading case however the presented prototype would show unwanted behaviour, according to the simulations in section 5.8.

The fabricated prototype is an overconstrained mechanism. This does not give any (serious) problems for the current prototype since it was fabricated monolithically using a fabrication process that does not give any residual stresses. Other fabrication methods or materials may result in a multistable mechanism, jeopardizing the working principle.

Case specific suspension design

A conceptual design is presented in the paper, see part II, based on the FACT method, see figure 2.1. When applied a moment on the end-effector, the annulus, half of the flexures will be loaded in tension while the others are compressed. Too high compression forces on slender beams result in buckling problems. The way this was solved for the fabricated prototype (presented in part II), was to mirror the entire suspension. To fit the mirrored design in the design space of a mechanical watch, the length l of the flexural components was decreased. In the case of a single-sided moment applied as the input the flexures of translational stage 1 and 2 can be oriented to be loaded in tension, see figure 2.1.

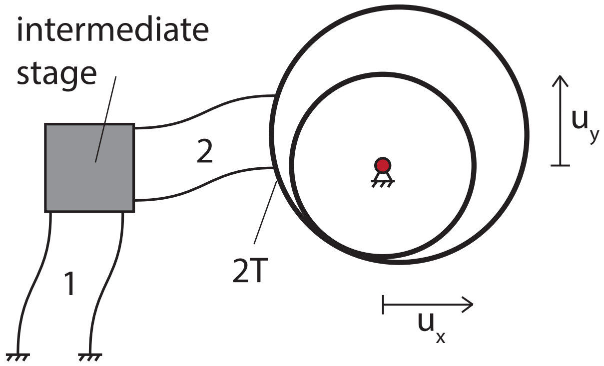

Figure 2.1: 2T (2 translational) suspension by combining two parallel flexure translational stages, following from FACT design method. The suspension has an resting position at u_x and u_y equal to 0, corresponding with the center of the central gear. An intermediate stage functions as reciprocating translational output.

The barrel gear in a mechanical watch will be the input for the system, and will always apply a one-sided torque. The prototype would work equally well for a clockwise and anti-clockwise applied torque, however this is not needed. A more optimal suspension design has the flexural members orientated such that all four beams are loaded in tension when an input torque is applied. This way buckling is prevented, and a rotationally stiff mechanism is achieved. Design parameters for the suspension are the length l of the flexural beams, spacing s between flexural beams, and thickness t of the flexural beams. Other design parameters are fixed to guarantee a statically balanced system when a load is applied to the system, see section 5.8. A Free-Body-Diagram (FBD) of the suspension, including an applied moment, shows how using a different spacing s between flexural members in x- and y-direction affects the stiffness of the suspension, see section 5.7. A varying spacing s between flexures of the translational stages results in a varying stiffness for x- and y-direction when a load is applied, hence jeopardizing the static balancing of the suspension. An identical spacing s for all four flexural members is determined to result in a statically balanced suspension, even under loaded conditions.

The flexural members are orientated such that the axis of the cycloidal rotor lies in the elastic center of both the first and second translational stage, figure 3.8(b), to ensure an both flexural members are loaded evenly during application of a force [6]. As such the outputs are positioned in line with the center of compliance, see figure 2.2(a).

The stiffness of the flexural members scales to the power 3 with the thickness, making the stiffness of the individual translational stages sensitive to fabrication errors. To minimize the effect of fabrication errors on the total stiffness of the suspension, the flexural members of the first and second translational stage are chosen equal. This way both the first and second translational stage, see 3.8(b), are equally affected, resulting in a statically balanced suspension despite of varying thickness.

To maximize the rotational stiffness, and minimize the translational stiffness, the length l and spacing s parameters are as large as the design space permits, including a minimal gap size of 100μm imposed by the etching process, see figure 2.2. Finite Element package *ANSYS® Mechanical APDL 14.5* is used to determine the minimal thickness t for which the stresses in loaded condition (applied torque and force) remain under 200MPa, a safe stress level for this fabrication process. This low design stress is to account for peak stresses that may result from shocks during an impact. Silicon will fracture rather than plastically deform since it is a mono-crystal, thus a high safety factor is included for the design stress. Exceeding the maximal stress level will result in instant failure in Silicon. The flexural components are modelled using BEAM188 elements, and the intermediate stages are modelled using element MPC184, representing rigid bodies.

This design approach results in a length l of the flexures of 14.3mm, with a spacing s from the center of the annulus of 8.9mm. These dimensions take into account the fabrication tolerances for the Silicon etching process. A flexure thickness t of 60μm results in a maximum Von Mises stress of 184MPa in the entire cycle including all loading conditions.

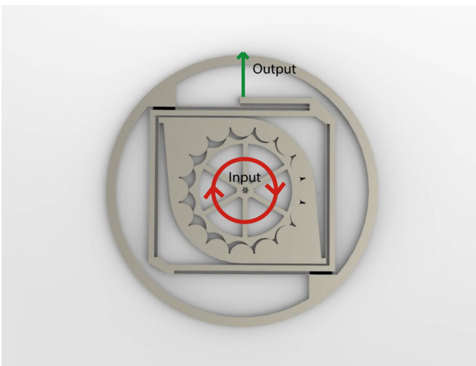

(a) Top-view of improved design. Central rotor is driven in clock-wise direction, resulting in tensional loaded flexures.

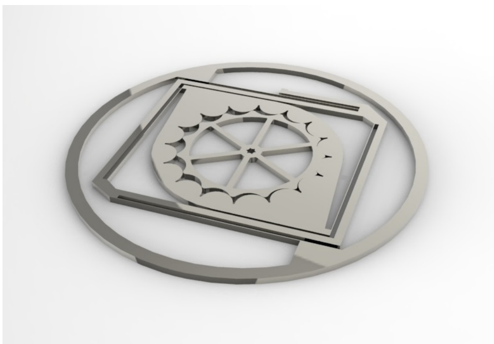

(b) Angle-view of improved design to show aspect ratio of flexures. Note that two identical layers are required to avoid singular positions. The second layer is rotated 90° with respect to the first layer.

Figure 2.2: Renders of improved design. The outer edge of the circular frame represents the design space with a diameter of 29mm. The diameter of the cycloidal rotor is 14mm, corresponding to dimensions of the current barrel gear. A flexure thickness of 60μm results in a permissible stress level, determined used FEM analysis.

In order to lock the annulus in both x- and y-direction a dual layer suspension is needed. One layer will take care of locking the x-direction, the other layer is meant to lock the y-direction. A single layer suspension will always have a singular position, where the annulus cannot be locked. A dual layer model is made in Ansys to analyse the performance of the system.

Performance

A model is implemented in Ansys, as will be elaborated on in section 5.8. This section only shows the most relevant results. Firstly the expected force transmission based on simulations is discussed. Note that the measurements in part II did not include an applied load on the input and a locked output stage, as will be the case in the real case. After this the robustness of the system in out-of-plane direction will be discussed.

Force analysis

A screenshot including all applied loads and constraints can be seen in figure 2.3. The stiffness of the suspension in loaded condition is 0.087N/mm resulting in a frictional loss of 2.7%, calculated using a contact force analysis, see section 5.8. This will only be the energy lost due to the addition of a compliant suspension with a certain stiffness.

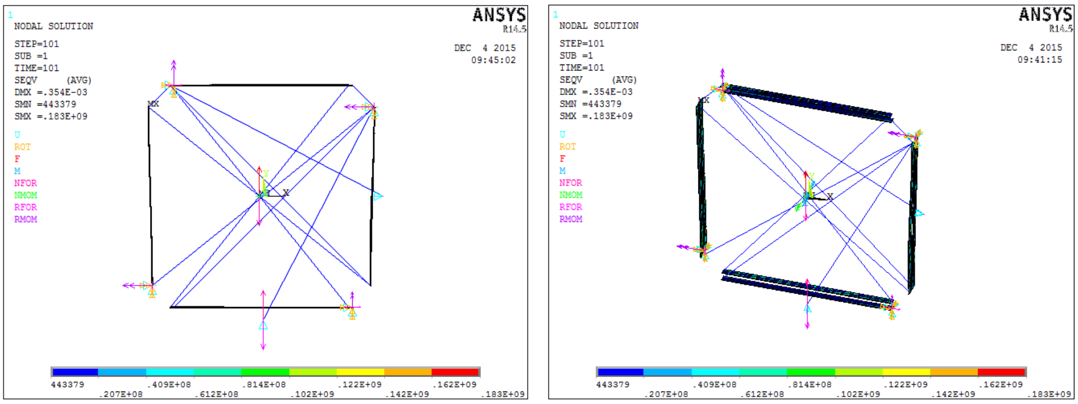

(a) Top-view of dual-layer model implemented in Ansys including all applied loads and constraints; 9Nmm on annulus center + $\frac{9}{7}$N ($\frac{M}{r}$) applied on the center of the rotor. The intermediate stages are locked to imitate a connected transmission.

(b) Angle-view of dual-layer model implemented in Ansys including all applied loads and constraints. Note the maximal Von Mises stress is 184MPa in the position with the maximum stresses during the cycle.

Figure 2.3: Screenshots of FEM model implemented in *ANSYS® Mechanical APDL 14.5*.

The simulated output force on the intermediate stages as a result of the applied loads and the component of the stiffness only are plotted in figure 2.4. Note that the reaction force on the intermediate stage is also the force that the rest of the reciprocating transmission will have to deliver as a counter force. In the case when an input load of 9Nmm is applied on the input of the system, these required reaction are in the order of 1 Newton, see figure 2.4(b).

Figure 2.4(a) clearly shows that the reaction force by the suspension stiffness has an equal magnitude in all directions, as was already discussed in part II.

Also the conclusion made that the energy loss as a result of the stiffness induced friction force is negligible, see part II, compared to the power being passed through the mechanism just by looking at the axes of the two plots, see figure 2.4. The stiffness component is very small compared to the forces applied and passed through the system by the barrel gear.

Robustness

By increasing the flexural components the out-of-plane stiffness is reduced compared to the fabricated prototype. Displacing the annulus in the out-of-plane (along z-axis) over 400μm results in a maximum stress of 220MPa. Note that this mechanism is a subsystem of a total system comprising of multiple layers, and therefore this out-of-plane displacement will never occur. A rigid constraint will be in place to prevent the annulus from moving such a distance, and thus protecting the flexural components from crossing the yield stress limit. To put the aforementioned displacement of 400μm in perspective, the total thickness of the planar mechanism is 525μm.

The annulus will be on contact with the cycloidal rotor at all time due to the applied moment from the barrel spring. The contact force between the annulus and rotor will reduce effect of any shock force in the out-of-plane direction (along z-axis). Shocks in other directions will be taken by the same mechanism that keeps the output (intermediate stage) locked in position.

An extreme case is simulated and depicted in figure 2.5. The full 9Nmm and resulting force from the gear contact is applied on the center of the annulus. At the same time the annulus is displaced and kept at 525μm (thickness of a silicon wafer) in z-direction, representing extreme conditions. The displacement is on the translational output shuttles is constrained, as explained in section 5.8. The maximum stress as a result of these extreme conditions is 517MPa, which is still a survivable stress level.

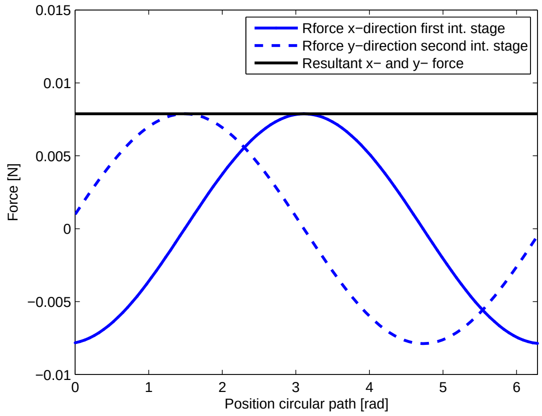

(a) Output force on locked intermediate stages in x- and y- direction without any applied loads to the input of the system. These reaction forces are the result of the suspension stiffness only. Note that the resultant of the x- and y-components is constant indicating a statically balanced suspension; the reaction force is constant in all positions.

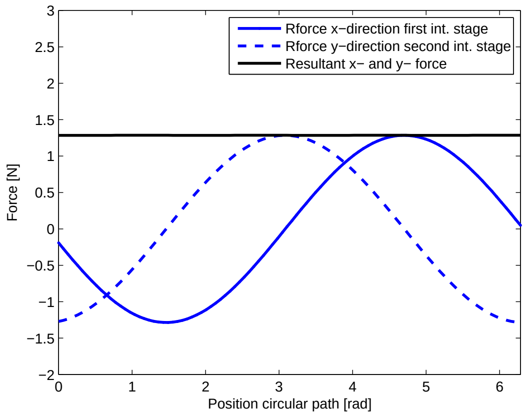

(b) Output force on locked intermediate stages in x- and y- direction including the applied moment and force on the input. Note that the connected suspension will have to deliver this locking force. The power transferred is orders of magnitude higher than the forces due to the suspension stiffness, see figure 2.4(a).

Figure 2.4: Simulated FEM in Ansys; force analysis of suspension with and without applied loads. A circular translation is prescribed on the system, resulting from the gear contact constraint, see section 5.8. The resultant force is dominated by the applied load, rather than the component of the stiffness of the suspension.

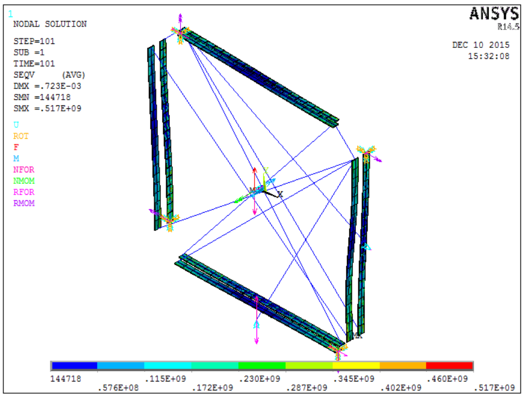

Figure 2.5: Loading conditions applied on center of annulus (moment + force) + extreme displacement of 525μm along z-axis resulting in a maximum stress of 517MPa. Although way above the design stress of 200MPa, the design should be able to survive this level of stress.

3

DESIGN PRINCIPLES

3.1. FUNCTIONS ORIGINAL CONCEPT

A circular translation of the internal ring gear is observed in the original design of the (three-) ring reducer. The rigid body parallelogram, as observed in the original design, is an example of a mechanisms that constrains the rotation while constraining the rotation of the connecting link (ring gear), see figure 4.1. For the sake of a micro design the aim is to replace the parallelogram mechanism with a (monolithic) compliant suspension. Since the ring gear only has a translating motion and no rotation, replacement by a compliant mechanism is a possibility. Looking at the original design of the ring reducer mechanism, several functions can be identified that are crucial for making the mechanism work. The essence of these functions is determined and used as starting point for the design of a compliant speed increaser mechanism.

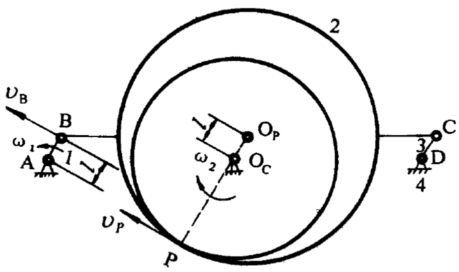

Figure 3.1: Mechanism diagram as sketched by Li[4]. A central gear with external gear profile meshes with an annulus (ring gear) with an internal gear profile. The annulus is the connection link between two parallel cranks of equal length. The resulting motion of the annulus is a translating circle.

3.2. SUSPENDING ANNULUS

The first function identified is the motion path of the ring gear: it describes a circular translational motion path. This motion is achieved by a parallel crank mechanism. The functional requirements for the motion of the ring can be distilled to two things:

- An in-plane (circular) translational path is allowed
- The radius of the path is constrained

Different ways of achieving the desired motion path are listed. The list is based on all possible degrees-of-freedom for a planar mechanism, thus making the list enclosing all possibilities. An overview is presented in table 3.1.

Table 3.1: Overview of functions for suspension

Function	Method	approach
Circular path + specific radius	1DOF circular path	remote center of motion mechanism
	2DOF + guarantee contact	**2T + internal contour**
		2T + external contour
	3DOF + guarantee contact + rotational constraint	2T1R + internal contour + constrain 1R
		2T1R + external contour + constrain 1R

Some functions require a way to 'guarantee contact' between the gear pairs. Guaranteeing contact can be done via a range of options. Another overview is presented to show all options to guarantee a contact between the gear pair. All reasoning steps will be elaborated in the following paragraphs. The viable options resulting from the reasoning are already highlighted in the presented overviews.

1DOF circular path This is exactly the type of behaviour we want to achieve for the suspension. A compliant suspension that could achieve this directly would be the best solution. However all rigid body mechanisms describing a circular path while at the same time constraining the rotational motion at the end point require at least one full cycle rotation. The full cycle rotation is obtained by a crank rotating about a revolute joint. The second observation is that we are limited in design space. The input gear (sun gear) is a given by the application. As a result we cannot use the centre of the sun gear to rotate around. Therefore a 'remote centre of rotation' mechanism is required to achieve the circular path for the ring gear. Again all encountered 'rigid body remote centre of rotation' mechanisms require at least one full rotation somewhere in the mechanism (figure 3.2). A full cycle rotation is something we cannot do with a monolithic, compliant, planar suspension. As a result all encountered 'compliant remote centre of rotation' mechanisms can only deliver a part of the circular path, not the full circle. For the ring reducer mechanism a full circular path is required.

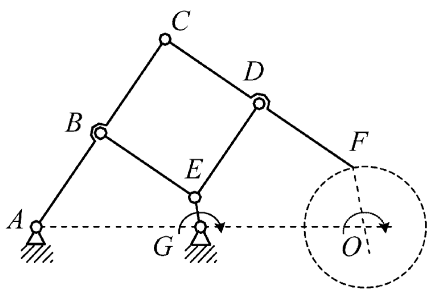

Figure 3.2: Example of a mechanism describing a circular path about a remote center[7]. A circular motion is obtained for point F, but a rotating pivot at point G is required. Other mechanisms exists performing the same remote center motion, but all of them require a full cycle rotating joint.

2DOF + guarantee contact As mentioned above, a 1DOF system is needed to replace the parallel cranks in the original design. By taking a system with two degrees-of-freedom and adding another constraint, we could achieve a 1DOF system. A planar system can have a maximum of 3 degrees-of-freedom: two translations and one rotation. Since one of the functional requirements of the suspension is to constrain the rotation, this automatically means that the two remaining degrees-of-freedom are two translations. As a result of this reasoning the extra constraint should be the one that constrains the circular path, thus constrains a certain radius. This can be either done by a constraint point (revolute joint) and a link with a certain offset, resulting in a radius (lower kinematic pair). Or by using a constraint line (cam) in the form of a circular object (higher kinematic pair). The latter can be used to follow the internal or external contour of the circular object (figure 3.3). Since we want the entire design to fit in a single plane, following an external contour will result

Table 3.2: Overview of approached to guarantee contact

Approach	Solution	Sub-solution
Guarantee contact	Ridid (kinematic pairs)	Lower pair (e.g. revolute joint + crank)
		Higher pair (e.g. cam)
	Elasticity (force)	**Use negative stiffness suspension**
		Use additional negative stiffness
	Magnetism	Permanent magnet
	Mass	Gravitational
		Centripetal

in interference between moving parts. Therefore only following an internal contour is selected as a feasible solution.

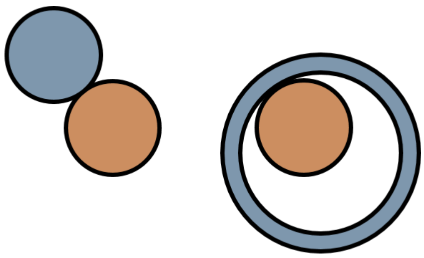

Figure 3.3: Using an internal or external body to constrain radius. These are the two ways of constraining a circular motion where only one side is blocked (by a body).

3DOF + guarantee contact + rotational constraint Following the same reasoning as before also a compliant suspension with three degrees-of-freedom could be combined with additional constraints. The suspension allows for two translations and 1 rotation (all DOF in-plane). Again an extra constraint is needed to constrain the radius, similar to the previous paragraph. This could be again done by either a lower (point constraint) or a higher (line constraint) kinematic pair. In this case however also an additional constraint is needed to lock the rotational motion of the ring gear. An in-plane system that only constrains the rotation is equivalent to an in-plane system that only allows two translations. Hence the additional constraint we need for this system to work is identical to the suspension described in the previous paragraph. Therefore the third category can be ruled out since it is identical to the second group, but increasing the complexity by adding an unnecessary parallel constraint.

3.3. GUARANTEE CONTACT

Another function fulfilled by the parallel crank mechanism is guaranteeing the contact between the two gears. For some solutions shown in table 3.1 a way to guarantee contact is required, therefore another set of solutions for this sub-category of functions is shown in table 3.2. Again the feasible solutions are highlighted. The following paragraphs will give an insight in the reasoning behind this selection. Note that all of the solutions shown in table 3.2 are the result of ‘ways to generate a passive contact (force)’, meaning no extra energy is required.

Lower pair Kinematic pairs (mechanical couplings) can be categorized into 2 groups; higher kinematic pairs and lower kinematic pairs. Lower kinematic pairs are defined by having a surface contact when relative motion takes place, while higher kinematic pairs have a line or point contact. Examples of a lower kinematic pair are screw pairs or slider bearings. To constrain a circular path using a lower kinematic pair, automatically a full cycle rotation is required between moving parts, e.g. a crank connected to a slider bearing. Examples of higher kinematic pairs are gearing and roller bearings. In this type of kinematic pairs the relative motion between moving parts is partly turning and partly sliding. Using a higher kinematic pair the problematic full cycle rotation can be avoided while still being able to constrain a circular path.

Elasticity Since we already established that we need a 2T mechanism to follow an circular internal contour, we can narrow down the stiffness profile that we need to guarantee a contact using the elasticity of the suspension. The suspension would then need to generate a force 'away from its center' at every position of the circular path, and this force should 'have the same magnitude' at every position. This mechanism therefore is a statically balanced negative stiffness x-y stage with an unstable equilibrium position in the center. This mechanism can either be the suspension itself, or an additional mechanism to guarantee the contact using a different mechanism as the suspension (resistant to torque). This category of solutions cannot be excluded based on reasoning or existing literature, therefore it is left as one of the possibilities. In the modelling chapter a section is dedicated to a suspension with such a stiffness profile to further check the feasibility of this concept.

Permanent magnet Another way of generating a passive (constant) force is by using a permanent magnet. If we use two magnetic surfaced on both sides of the gear pair, these two surfaces will attract and remain in contact, at least that is the idea. A quick search to the state of the art of permanent magnets in MEMS shows that this category of solutions can be excluded. Existing methods either have a too low performance, resulting in a low contact force between the gears. Such a low contact force would result in a mechanism that is sensitive to shocks, since a small perturbation would result in a loss of contact between the gears. Other reasons are the fabrication process that limits the use of permanent magnets. For example for rare-earth alloys, reported having higher performance [8], requires the use of special substrates and high-temperature annealing. Since we are currently using etching processes in Silicon, these stumbling blocks in the manufacturing of MEMS permanent magnets are insurmountable.

Centripetal & gravitational Another passive way of generating a force is by using the mass of the system itself. However the direction of the contact force changes when the gears move with respect to each other, rendering gravitational force useless. And centripetal forces only come in play for fast moving masses. Since we have a system moving at nearly zero velocity, the use of centripetal forces is not an option. Also the small weight of the moving mass would require a very high velocity to generate an acceptable contact force.

3.4. SUSPENSION SYNTHESIS

A systematic way to determine the design of the compliant suspension to replace the aforementioned parallelogram linkage is needed. Firstly a method is discussed that allows the user to find all topologies of rigid body linkages with a specific degree-of-freedom. After that an alternative method is discussed aiming at finding a compliant suspension allowing a certain degree-of-freedom. The latter was found to be a more direct and effective approach to find the desired suspension for this case.

TOPOLOGY

The design of the compliant suspension will start at the basis functionality the suspension has to fulfil and will then be expanded with more criteria to find the optimal design. The first criteria for the compliant suspension is to allow motion in two directions. For this reason all possible mechanisms with 2 degrees-of-freedom are identified. Gruebler's equation (equation (3.1)) gives all possible numeral combinations of links and joints that form a 2 DOF mechanism. In this equation n and n stand for the number of links and joints respectively.

$$DOF = 3(n-1) - 2f \tag{3.1}$$

Table 3.3: Combinations of links and joints resulting in a 2DOF mechanism

Number of links	Number of joints
3	2
5	5
7	8
9	11

The first four combinations resulting in a 2 degrees-of-freedom mechanism are listed in table 3.3. There are more possible solutions from Gruebler's formula, but these are not considered in this design. Increasing the number of links and joints will result in a more complex system. Generally the simpler a design is, the better. Especially when the mechanism needs to be converted to a compliant version fewer joints are desired. The next step is type synthesis where all possible topologies are generated. Increasing the number of links and joints will result in an increased number of topologies. The combinations listed in table 3.3 already result in 39 different topologies, considering only the 'non-fractioned' kinematic chains [9]. The 39 topologies can be seen in figure 3.4.

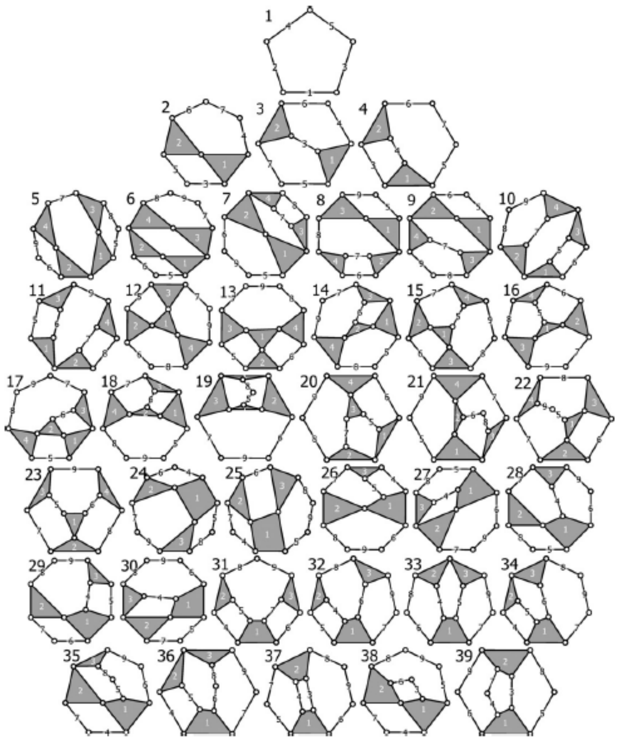

Figure 3.4: 39 topologies with 2 degrees-of-freedom[9]. These topologies do not include the open loop mechanisms.

The generated kinematic chains are only the closed-loop solutions. The solution with the fewest links and joints (table 3.3) does not appear in this overview (figure 3.4) since it cannot have a closed loop. This simple 2DOF mechanism is shown in figure 3.5(a).

Also the mechanism with 5 links and 5 joints has an additional open-loop variant, that is not depicted in the overview in figure 3.4. This open-loop variant can be seen in figure 3.5(b). Both of these mechanisms are not considered in the method for generating topologies presented by [9].

This mechanism synthesis method does give a nice overview of possible mechanisms allowing two degrees-of-freedom. However as discussed before, we not only need a 2DOF mechanism, it also needs to constrain the rotation. Therefore an additional check needs to be performed in the remaining 2DOF mechanisms to shown all 2T mechanisms. Another downside of this synthesis method is the fact that these are rigid body mechanisms. An additional design step is needed to transform these linkages into compliant mechanisms.

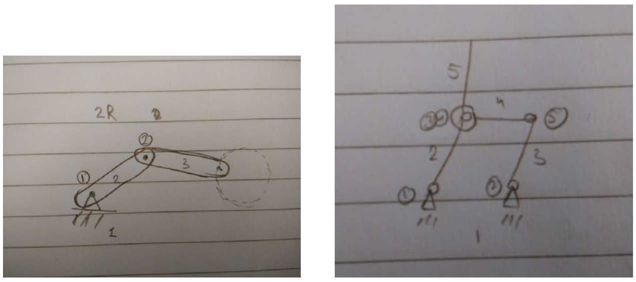

(a) open-loop 2DOF mechanism with 3 links and 2 joints.

(b) open-loop 2DOF mechanism with 5 links and 5 joints.

Figure 3.5: Open-loop linkages not included in 39 topologies in figure 3.4.

A mechanism synthesis method that includes the restrictions imposed by using a compliant design would be beneficial. Therefore we opted to go for a different method that is developed for compliant mechanism synthesis.

FACT METHOD

Based on the observations made on the original gear reducer design some requirements for the compliant suspension can be found. These requirements for the suspension are used in a design methodology for finding all possible designs that fit the requirements. A design methodology that is developed as a tool for designing compliant mechanisms based on their desired degrees of freedom is the 'Freedom And Constraint Topology' design method (FACT)[10]. The FACT method is aiming at giving the designer an intuitive tool to translate the requirements into a specific conceptual designs. This method is in contrast to most other design tools, which rely on the insight of the designer and requires many iterations (figure 3.6, according to Hopkins[10].

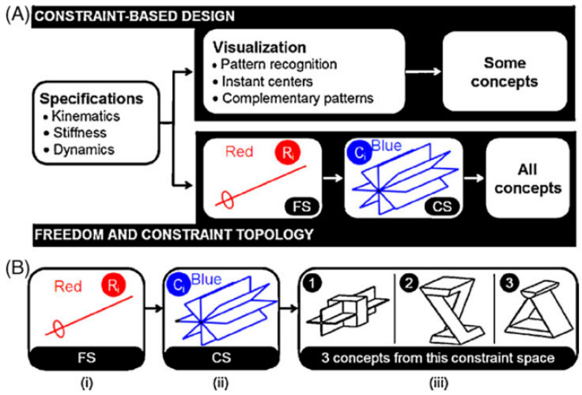

Figure 3.6: FACT method in contrast to traditional design methodology [10]. Traditional design methods rely a great deal on experience of the designer. The FACT method aims to give a complete overview of the solution space.

The FACT method is uses a 'Freedom Space', figure 3.6, which describes the permissible (desired) motion of the mechanism. At this stage the requirements are used as an input for the design methodology. As described above it is difficult to come up with conceptual solutions directly from the specified permissible motions. Therefore the FACT method also specifies a 'Constraint Space' figure 3.6, a set that contains all the constraints that result in a certain permissible motion. The FACT method defines a principle - the principle of complementary topologies - that provides a unique mapping between the 'Freedom Space' and its 'Constraint Space'. So for every set of permissible motions the FACT method defines which set of constraints can be used to achieve the desired motion. The designer then can simply pick constraints from the 'Constraint Space' to form various conceptual solutions (figure 3.6).

At first the complementary topologies were only mapped for parallel flexure systems [10]. In a later publication this was expanded to incorporate also serial flexural systems [11].

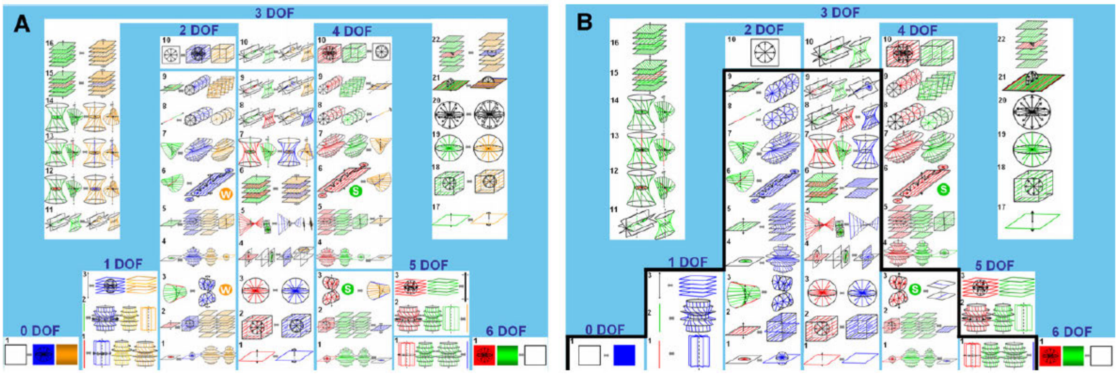

Figure 3.7: 'Twist and wrench types' (A) and Mapping of 'Constraint Space' for flexure synthesis (B) [11]. Defining a desired freedom space and following this chart will provide the solution space using the FACT method.

In our case there are two permissible motions; two translational motions. The rotational motion is constrained. This can be translated into a freedom topology for the FACT method: A 2T (2 translational) freedom topology.

Following the schematic provided by Hopkins [11] to synthesize flexure designs, we can see that a planar 2T mechanism (2DOF type 10 in figure 3.7) falls outside of the framed types. The latter means that a planar 2T mechanism cannot be synthesized using only parallel flexure elements, and a combination of building blocks is needed, resulting in a serial mechanism. Following the design steps in the FACT method we find that there is one solution to obtain a planar 2T mechanism, see figure 3.8, and that is to combine two perpendicular translational stages using an intermediate body. The easiest configuration for a translational stage is shown in figure 3.8(a).

Combining two of these translational stages using an intermediate body results in the conceptual solution for the suspension shown in figure 3.8(b).

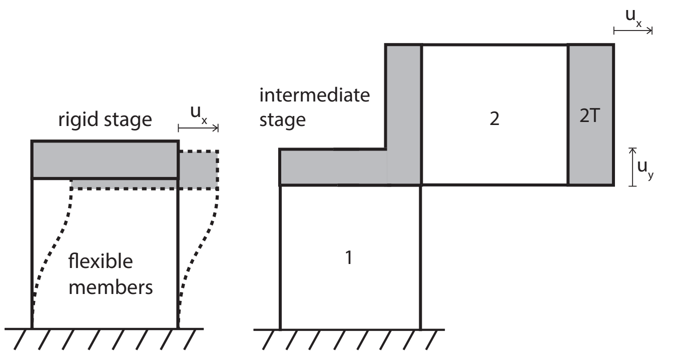

(a) 2T (2 translational) suspension by combining two parallel flexure translational stages

(b) 2T (2 translational) suspension by combining two parallel flexure translational stages

Figure 3.8: FACT method to determine suspension design. Combining two translational parallel flexure stages using an intermediate rigid stage to form a 2T mechanism. Following this method, 4 is the fewest number of flexural members to obtain a 2T suspension.

4

PROTOTYPES

Before spending resources on the design of a novel mechanism a feasibility study is required. This way any complications that rise with the implementation should come to light at an early stage. For the design of a transmission on a micro scale several aspects should be checked before proceeding.

4.1. WORKING PRINCIPLE ORIGINAL CONCEPT

MOTION PRINCIPLE

The working principle of the ring reducer mechanism is based on a circular motion path of the internal geared ring[4]. The circular path is achieved by the use of two parallel crank links of equal length, as depicted in figure 4.1. The annulus (ring gear) forms the connecting link between the two cranks. As a result the connecting link (annulus) traces a *circular path* with *no rotation* relative to the ground. Note that the distance l between the center of the central gear and the center of the annulus equals the length of the cranks. This way the two gears remain in contact throughout the entire cycle. The diameters of the circles drawn represent the 'reference diameter' of the gear profiles. The *closer* the diameters of the two gears are together, the *smaller* the required crank links will be.

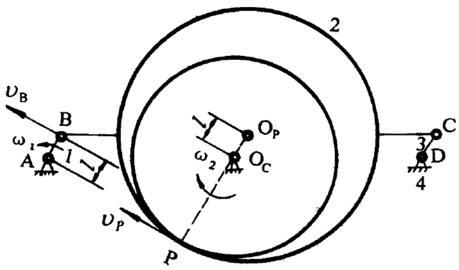

Figure 4.1: Mechanism diagram as sketched by Li[4]. A central gear with external gear profile meshes with an annulus (ring gear) with an internal gear profile. The annulus is the connection link between two parallel cranks of equal length. The resulting motion of the annulus is a translating circle.

RING SPEED INCREASER

As the name suggests the ring reducer is designed to reduce the rotational speed of the input shaft. Depending on the ratios of the gears large reduction ratios can be achieved. In this case however the speed of the input shaft has to be increased, rather than decreased. To check whether or not the mechanism is bidirectional a free body diagram was made (figure 4.2). The force acting on the ring as a result of the torque on the input shaft is always in the tangential direction of the rotation of the output crank. Therefore the mechanism should be able to inverse the input and output and act as a speed increaser.

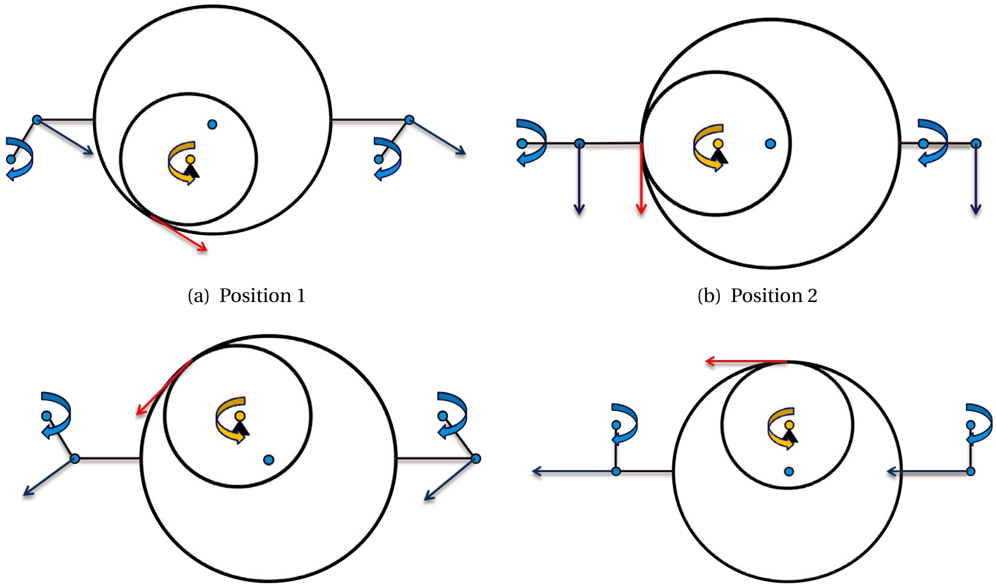

(a) Position 1 (b) Position 2

(c) Position 3 (d) Position 4

Figure 4.2: Free body diagram of ring reducer mechanism during various positions of operation. The direction of the forces are illustrated to show that the mechanism can also be driven by the central gear, acting as an speed increaser rather than speed reducer.

There is however a singular point in the trajectory, as seen in figure 5.27(b), where the crank links and ring link align. This singularity will pose a problem for the working principle of the ring reducer. Solutions have been presented to overcome this singularity [12][5].

RATIO

The ratio between the input (central gear) and the output (cranks) can be calculated as from the difference of the diameters as described in the following equation. The calculation for the ratio can be directly extended to the number of teeth of the two gears. The *closer* the diameters are together, the *larger* the transmission ratio will be. A compliant suspension with a small range of motion could therefore still achieve a high ratio.

$$R_i = \frac{d_{central}}{d_{annulus} - d_{central}}$$

4.2. PROTOTYPE 0

What The first prototype was a replica of the design shown in the ring reducer paper [4]. This paper describes a novel cycloid reducer mechanism, of which the diagram is shown in figure 4.1. The mechanism as described by Li [4] is driven by the link AB. To avoid a singular position, link AB and DC are synchronized using a pulley mounted on the two driven shafts (A and D). Link 2 connecting the two incorporates a gear with internal gearing, meshing with the external gear mounted on the output shaft O_C. The length of the driven links AB and DC is chosen such that the gear pair is always meshed correctly.

Why As mentioned above, the mechanism is driven via link AB (and DC) and the output is a slower moving rotation at shaft O_C. For out application we are not interested in a speed reducer, but a speed increaser. This prototype was fabricated to get a better understanding of the ring reducer mechanism, but also to check the assumption that the input and output of the system can be inverted without jeopardizing the function.

How A model was designed in Solidworks containing the functional parts as shown in figure 4.1. The gear profile was generated using a specialized gear design program called Kissoft. The gear ratio for this prototype was chosen to be 10; 90 and 99 teeth for respectively the central gear and the ring gear. For every rotation of the central external gear, the crank links AB and DC were expected to rotate 10 times. The module was chosen matching to the overall dimensions of the prototype. The parts and gears were cut from PMMA using a laser cutter. The mechanism requires 5 pivots to function, located at A, B, C, D and O_C. Slider bearings were used at these locations to allow for the rotation. A cylindrical bar of aluminium was cut unto small units to form the shafts for the mechanism.

Results As expected the two parallel cranks have a singular position, which can clearly be seen and felt during operation. The ring gear link sometimes has the tendency to switch to the 'wrong' position, resulting in a locked system. In the range clear from this singular position however the system behaves as expected. The system can either be driven by the crank link(s), or by the central gear.

A picture of the fabricated prototype is shown in figure 4.3.

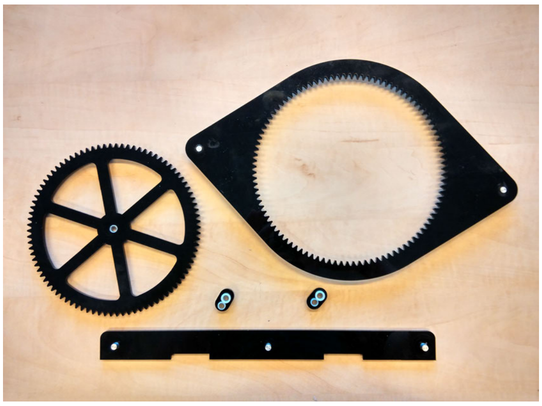

(a) Parts ring reducer prototype fabricated from PMMA and cut using a laser cutter at the TU Delft workshop.

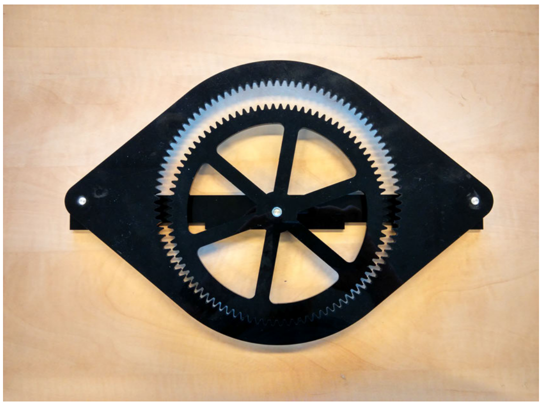

(b) Assembled ring reducer prototype. The rotating joints are made from plastic slider bearings.

Figure 4.3: Prototype to proof speed increaser principle as illustrated in figure 4.2

The slider bearings and the shafts have some backlash, resulting in some play in the system. As a result of this play the ring gear and central gear sometimes tend to misalign due to the ring gear moving out of plane. When this happens the gears are no longer in contact and some gears are skipped. This is clearly a result of the poor manufacturing process.

Conclusion The input and output of the ring speed reducer mechanism can indeed be switched, hence resulting in a ring speed increaser mechanism.

4.3. PROTOTYPE I

What This was the first attempt at designing a gear system with the ring gear attached to a compliant suspension. The parallel crank mechanism shown in prototype 0 is replaced by a suspension.

Why The aim of this suspension is to fully replace the parallel cranks and their functions. Therefore a negative stiffness was required for this suspension, pushing the gears into contact. Removing most of the pivots will result in a design that can be more easily scaled down.

How The internal and external gears were designed with the program Kissoft. The number of teeth on the gears was chosen as 60 for the central gear and 66 for the ring gear. A ratio of 10 was the result for this prototype. The gears profile is an involute profile. The module was chosen according to the scale of the prototype; the smaller the prototype, the smaller the module. The scale of the prototype was approximately

1:3.5, compared to the actual barrel gear of the mechanical watch. The resulting reference diameter of the central gear (in the application the barrel gear) was in 48 mm. The module of the gears was M = 0.8. The reference diameter of the internally teethed ring gear was 52.8 mm, based on the same module. As a result the central gear has a 'wiggle room' of 2.4 mm to the left and right.

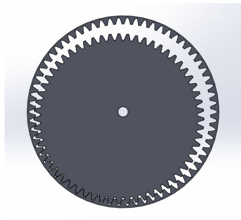

Figure 4.4: Assembly of the involute gears used for prototype I. Kissoft program was used to draw the profile of these gears.

Figure 4.4 shows an assembly of the gears. The difference in diameters is shown in the figure by an eccentric hole in the central gear. This eccentric hole has an offset of 2.4 mm measured from the center of the central gear. In the actual design this offset will be created by the suspension of the ring gear, and not by an eccentric hole in the central gear.

The design of the suspension is based on the simplest way to create a 2T (2 translational) compliant mechanism according to the FACT method. This reasoning will be elaborated in another chapter. The mechanism consists of 2 1T mechanisms connected in series to result in a 2T mechanism. The only way to create a 1T mechanism with only flexural components is to place two constraints in parallel planes. A very simple serial mechanism consisting of 4 flexures with one intermediate body was designed. The design was mirrored to achieve a higher out-of-plane stiffness. This also results in an over-constrained mechanism, however for small motions this is not a problem as will be shown later by the Ansys simulations.

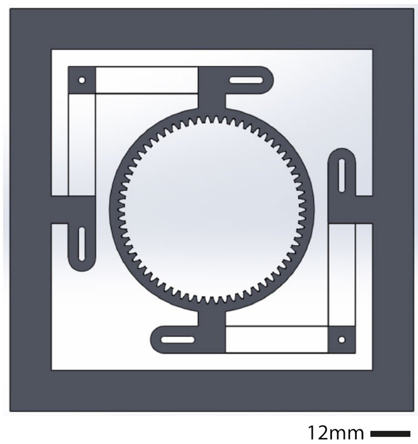

Figure 4.5: Suspension of ring gear. The individual parallel flexure stages will be placed under compression by applying pre stressed coil springs. Each of the parallel stages will behave as a bistable mechanism, ensuring a contact between the gear pair. At least that is the idea.

A simple 2T mechanism however is not enough. The gears also have to be pushed into contact. This will be done by modifying the design of the suspension to achieve a negative stiffness, instead of the inherent positive stiffness.

Figure 4.6 shows the approach used to achieve a bistable behaviour of the parallel suspension. Additional tension springs are attached between the rigid parts to pre-tension the parallel flexure beams. Since the connection points lay further apart than the length of the flexures this will result in a bistable behaviour.

An Ansys simulation (figure 4.7) is done to achieve the desired bistable behaviour as a result of applying pre-stress with an additional tension spring. The stiffness of this spring was determined from the Ansys modelling. To account for any errors in the manufacturing and assembly of the design a tuning slot was designed on both stages of the suspension. With these tuning slots the amount of pre-tension of the springs can be

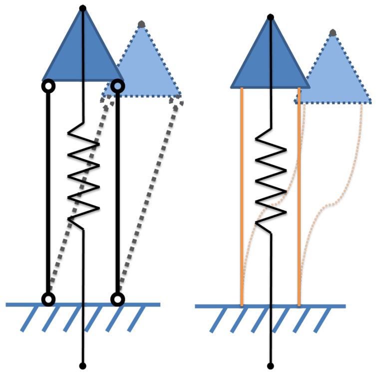

(a) Rigid body bistable mechanism. (b) compliant bistable mechanism.

Figure 4.6: Approach to achieve a bistable mechanism is to compress a parallel flexure mechanism using a pre stressed tensional coil spring.

adjusted. The Ansys simulation calculates the reaction forces for a circular displacement. Moving over this circular path is done in 100 steps. When plotting the calculated data for each of these 100 steps a nice graph of the resulting forces and stiffnesses over the entire rotation appears (figure 4.8(a)).

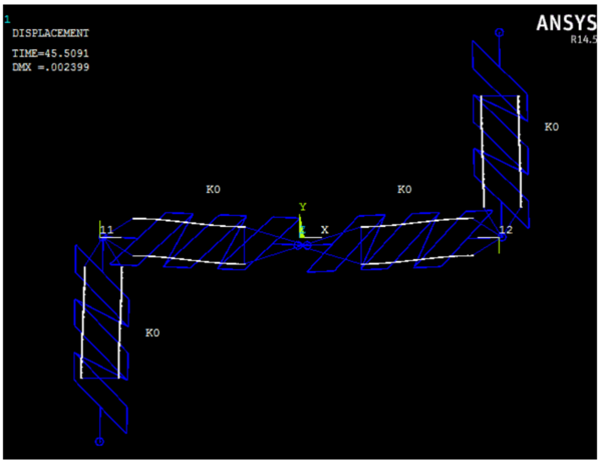

Figure 4.7: Simulation of the compliant suspension in finite element modelling (Ansys). The bistable behaviour was analysed, and a corresponding coil spring stiffness was selected.

An interesting observation is made when the resulting forces are considered. In figure 4.8 the resulting forces are plotted from prescribing a circular motion path. The plot in the top shows that the resulting forces change direction over the entire cycle. Depending on the direction of the stiffness, the forces either always point toward, or away from the center, as can be seen by the circular graph. Interestingly the direction of the force does not matter. Thus the suspension can be balanced both by using a positive stiffness, as well as using a bistable mechanism. As long as the stiffness is linear and equal, the forces are cancelled out.

From the magnitude of the resulting forces, plotted below, can be concluded that the resulting force is equal in all directions. As a result the stiffness in tangential direction of the motion path will be equal to zero, hence statically balanced.

The springs will be attached at the connection points (springs not shown), see figure 4.5, and the force can be tuned via the slots.

The rigid parts of the prototype were cut from PMMA using a laser cutter, see figure 4.9. The flexures were cut from 0.1mm spring steel and glued in place in the PMMA. For this purpuse recesses were included in the PMMA cutting patern where the flexures fit snuggly. Super glue was then applied to fix the flexures in place. This fabrication technique has been used multiple times in the compliant mechanisms lab, and has proven

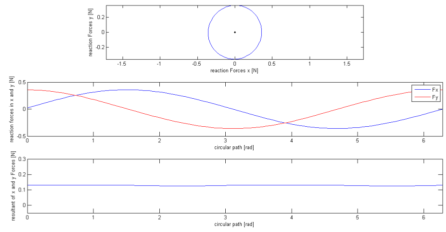

(a) Positive stiffness suspension resulting in a statically balanced system.

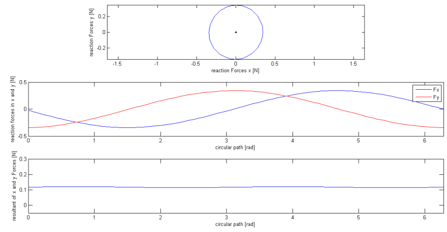

(b) Negative stiffness suspension resulting in a statically balanced system.

Figure 4.8: Positive or negative suspension stiffnesses using finite element simulation. According to the simulations the bistable behaviour would result in a statically balanced mechanism. In both cases the stiffness of the suspension would ensure a contact between the gear pair.

itself useful for small prototypes.

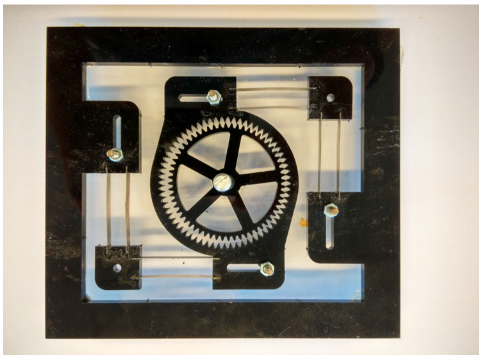

Figure 4.9: Fabricated compliant ring reducer prototype. Again cut from PMMA using a laser cutter at the TU Delft workshop. The flexures were cut from a sheet of spring steel, and glued in position using super glue. Coil springs were attached to pieces of thread, which where tightened after tuning. The entire prototype has a length of roughly 120mm.

Results A picture of the fabricated prototype can be seen in figure This design has been fabricated on a larger scale as a proof of concept model. No measurements were performed on this model. It was fabricated to get an idea of the kinematics and to check the method for creating a suspension with an unstable equilibrium point in the center. The prototype showed poor results in terms of robustness. This prototype relied on buckling of compliant beams by pre-tensioning them with additional tension springs. As a result the rotational stiffness of the suspension was greatly decreased. The rotational stiffness of the suspension has to be high for the application to work. As a result of pre-stressing the suspension to the verge of buckling results in a system that can not transfer any more load to perform work. The suspension is already loaded to the max to achieve a negative stiffness, and any additional torque will buckle the system. Another observation made was the result of positioning the flexural elements close together. When an input torque in applied to the ring gear, the resulting forces in two parallel flexures will be a compressive and a tensile force. The tensile force will stiffen the structure, however the compressed flexural element will buckle under the load. A solution implement in the next model is to position the flexures further apart, resulting in a bigger moment arm between the applied input torque and the center of rotation of the flexure. The result will be a much stiffer system. Also the direction of the forces in the flexural members will be further investigated (tensile or compressive), since they have a huge effect on stiffening or softening of the system.

Conclusion Using pre-stress to achieve a bistable behaviour is very sensitive, and can easily result in buckling (failing) of the flexural components. Other methods to guarantee a contact between the gears will have to be found, since using a negative stiffness alone is too sensitive and risky.

4.4. PROTOTYPE II

What The lessons learned from the first prototype are used in the design of the second prototype. The second prototype incorporates a different method for 'guaranteeing contact'. Instead of a negative stiffness using buckling compliant beams, this time the function of 'guaranteeing contact' was done by using a rigid constraint solution.

Why A large scale prototype was required for both testing the new gear profile concept to guarantee contact, and as a proof of principle demo to shown the complete transmission mechanism. The complete transmission mechanism includes the remainder of the reciprocating compliant suspension. The latter is a different part of the transmission project, therefore only the compliant ring reducer prototype will be discussed.

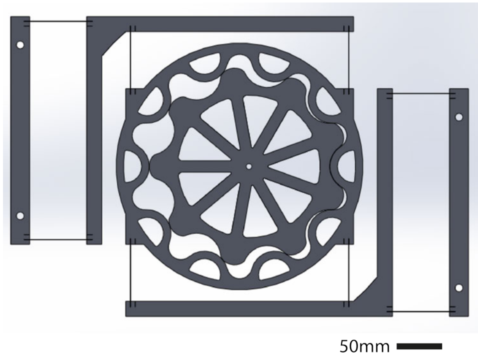

Figure 4.10: Overview of the second prototype of the compliant suspended gear mechanism. This prototype was to be connected with a prototype of the reciprocating transmission. To obtain the range of motion required for the input of this reciprocating transmission prototype, this prototype was made on a larger scale than previous ones.

How Firstly the lessons learned from the previous prototype in terms of flexure placement were taken into practice. Of course the majority of buckling issues encountered with prototype *I* were due to the pre-stressing force applied by the springs. But after removing the pre-stress the rotational stiffness of the suspension was not high, as a result of buckling of the beams. After a free-body-diagram of the situation it was concluded that the flexures should be placed as far apart as possible to increase the lever arm, and reduce the chance of buckling any beams. Therefore the flexures are placed on either end of the ring gear, as can be seen in figure 4.10.

The cycloidal profile can be described by the following equation. Several constraints are needed to find the plausible rotor shapes (e.g. undercutting or interfering bodies), which will be elaborated on in the section 5.8. Feasible parameters for the rotor shape were selected and implemented in the equation for the rotor shape (equation (5.11). The selected parameters can be seen in table 4.1. As can be seen from the parameters used for the rotor design, this is a large scale prototype. Reason for these dimensions is to get a good view on the interaction between the various transmission systems (not shown in this report). Also a large range of motion was required for the other parts of the transmission, hence the large eccentricity $e = 10mm$ for this prototype.

$$C_x = R\cos\phi - R_r\cos(\phi+\psi) - e\cos\big((N+1)\phi\big) \tag{4.1}$$

$$C_y = R\sin\phi - R_r\sin(\phi+\psi) + e\sin\big((N+1)\phi\big) \tag{4.2}$$

A ratio of 9 was selected for this prototype, and again the same fabrication techniques were used as in the previous prototype. Note that the out-of-plane stiffness of this prototype is poor. The suspension cannot handle, and sags under its own weight. This prototype is merely designed as a demo, and to show the working principle of the cycloidal gear. The soft suspension is however enough to sufficiently constrain the rotation, which is a key aspect for the working of the mechanism.

Results A figure of the fabricated prototype can be seen in figure 4.11

Table 4.1: parameters rotor shape for prototype II

Parameter	Symbol	Unit	Value
Radius central gear	R	[mm]	120
eccentricity	e	[mm]	10
Radius rollers	R_r	[mm]	25
Number or rollers	N	[-]	10

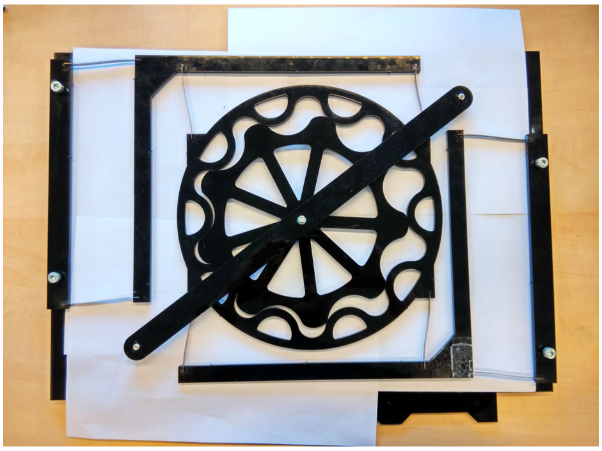

Figure 4.11: Second fabricated compliant ring reducer prototype. The length of the total prototype is approximately 500mm to facilitate a large range of motion for the prototype of the subsequent stage in the transmission (not shown in the picture).

Conclusion The rotational stiffness has improved significantly over the previous design where the flexures were positioned close together. However since there will be a significant input torque applied to the system this improvement is not sufficient. A more promising solution will be to achieve only tensile forces in all flexures, eliminating all buckling problems. Repositioning and re-arranging the flexures again for the next design will increase the rotational stiffness even further. This prototype is the first prototype that showed the envisioned kinematics. When an input torque is applied on the axis of the cycloidal rotor, the ring gear will translate over a circle, resulting in a translational output for the shuttles.

4.5. PROTOTYPE III

What Prototype III implements the same design features as prototype II, but this time on a small scale; diameter of annulus 10.4mm.

Why The kinematics of prototype II showed promising results, therefore it was selected to be fabricated on a small scale to show any unexpected behaviour, and to verify the simulations: the static balancing performance, and frictional loss.

How A design was made to be etched in Silicon using deep reactive-ion etching (DRIE), a process where a wafer is subjected to chemicals using a photo-reactive layer to project the design on the Silicon wafer. The topology of the design is identical to that of prototype II, but flexures are placed oriented in a more volumetric efficient way, see figure 4.12.

Parameters for the cycloidal rotor of prototype III are presented in table 4.2. As can be seen a different value for the number of rollers on the annulus is used, resulting in a ratio of 15.

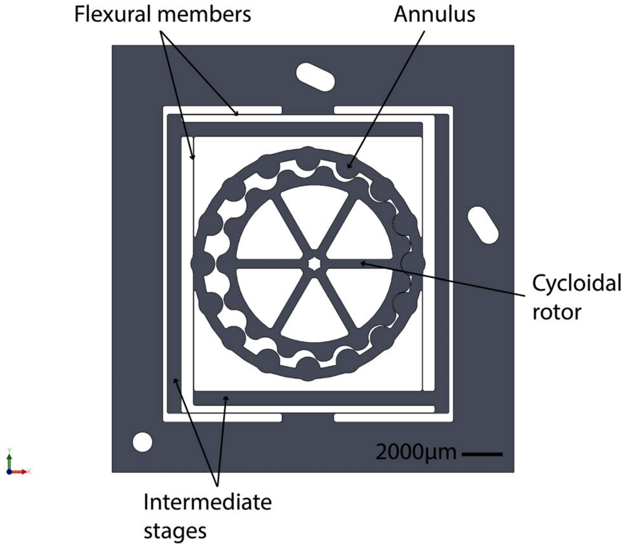

Figure 4.12: Drawing of Silicon prototype to be fabricated using DRIE. This prototype is fabricated validate the predicted energy loss due to stiffness, and measure performance of the static balancing.

Table 4.2: parameters rotor shape for prototype III

Parameter	Symbol	Unit	Value
Radius central gear	R	[mm]	5.2
eccentricity	e	[mm]	0.295
Radius rollers	R_r	[mm]	0.6
Number or rollers	N	[-]	16

Pictures of the fabricated prototype can be seen in figure 4.13.

The etching process results in sharp features, as can be seen in figure 4.14. The thickness in the CAD drawing was 30μm, which is significantly reduced by the etching process; more material is removed than should. Next prototype will incorporate thicker features to make up for this. Another observation is that some over-etching has occurred; the thickness of the flexural elements depends on the height. The top and bottom thickness varies, resulting in an approximate trapezoidal cross-sectional area, instead of rectangular. Again something to be taken into account.

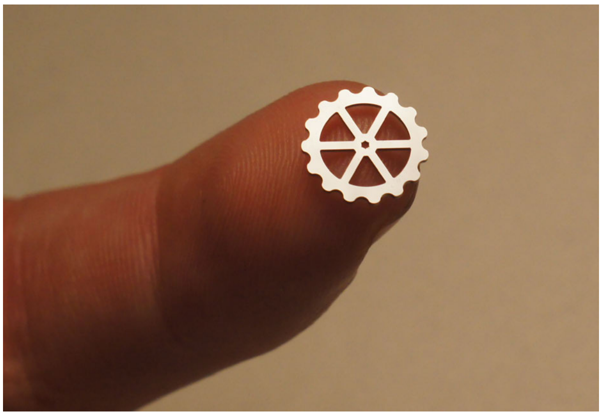

(a) Cycloidal rotor fabricated on micro scale, with a diameter of roughly 10mm.

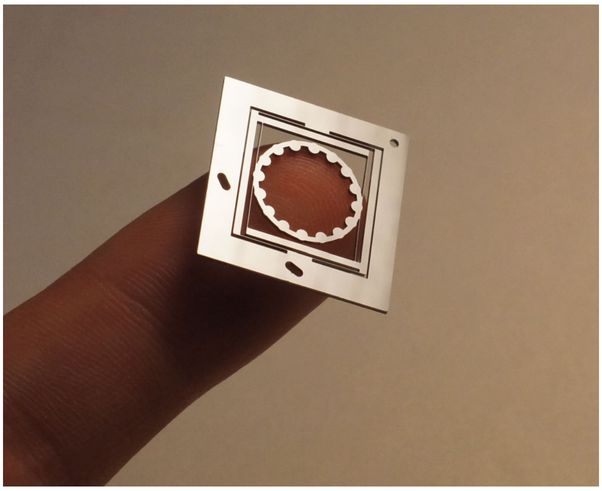

(b) Compliant suspension and annulus fabricated on micro scale. The total suspension prototype was roughly 20x20mm.

Figure 4.13: Fabricated micro scale silicon prototype using DRIE process.

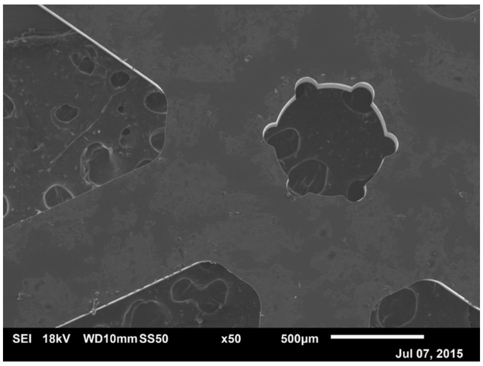

(a) Hexagonal feature of cycloidal rotor to be fitted on shaft.

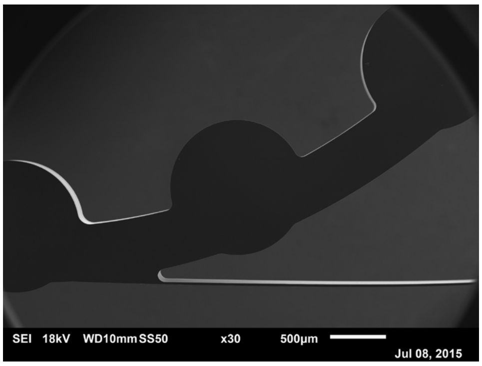

(b) Sharp edges as a result of DRIE.

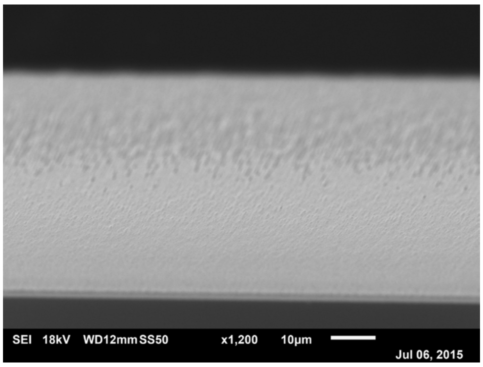

(c) Smooth surface after etching.

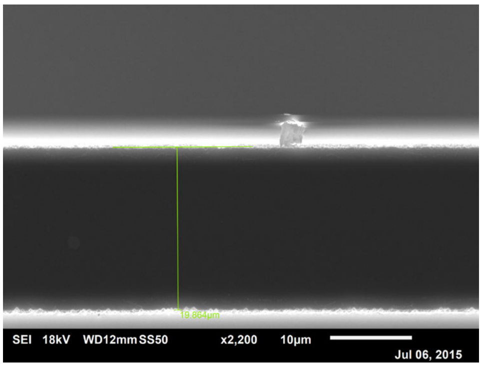

(d) Measured thickness of flexures varies for top and bottom of etched profile.

Figure 4.14: SEM (Scanning Electron Microscope) images of the Silicon prototype. This measurement was done on visual inspection, hence yields a tolerance of $\pm 1.5\mu$m.

5

Modelling

The efficiency of the newly proposed gear mechanism is still unknown. However estimations are possible based on existing knowledge about cycloidal drives[13]. The working principle of this system is different than a typical cycloidal drive, but the gear profile and wobbling motion is identical. Mackic ([14] mentions that the efficiency of the cycloidal drive is primarily depends on the friction between the elements in the cyclo drive. The general equation for the efficiency can be formulated as:

$$\eta = \frac{M_{in} 2\pi - W}{M_{in} 2\pi} \tag{5.1}$$

In this equation M_{in} stands for the input torque on the system. In our case the torque resulting from the barrel spring. The W represents the work done by frictional losses. In the traditional cycloidal drive this term would encompass frictional elements like

- rolling friction in the mounting of the cycloid disc on the input shaft,
- Rolling friction between output rollers and holes in the cycloid disc,
- Rolling friction between housing rollers and the cycloid disc,
- Sliding friction in the mounting of the output rollers,
- Sliding friction in the mounting of the housing rollers

Not all of these components are present in the newly proposed mechanism. Therefore some of the frictional terms can be discarded. On the other hand the stiffness of the suspension has an influence on the efficiency of the system, something not encountered in the traditional cycloidal drive.

To estimate the efficiency η of the compliant suspended gear transmission the loss term W has to be estimated. For the novel suspended gear mechanism this loss term encompasses both the losses from the gear contact, but also the losses as a result of the reaction forces of the suspension (mechanical advantage).

- Reaction forces opposing direction of motion as a result of stiffness suspension (mechanical advantage),
- Frictional losses on contact point between barrel gear and ring gear (as a result of stiffness),
- Frictional loss in the jewel bearings of the barrel gear,

5.1. Mechanical advantage

Compliant mechanisms gain their motion by deflecting flexible beams. As a result of this deflection energy is stored in these compliant members. The energy stored in the beams is generally considered as lost energy. A way to define this energy loss is to look at the mechanical efficiency of a compliant mechanism. The mechanical efficiency of a traditional rigid mechanism is a function of the linkage position only.

The mechanical efficiency of a mechanism is defined by looking at the expression for the total energy Π of the system [15]. The total energy consist of the strain energy U minus the work done by the system W.

$$\Pi = U - W$$

For a system in equilibrium the changes of the total energy must be equal to zero.

$$\delta\Pi = 0 = \delta U - \delta W$$

The rigid body mechanism is connected to the ground via a simple revolute joint. Here we assume that there is no frictional loss and no stiffness in the joint. As a result the work on the input of the system will be equal to the work at the output of the system. The work is defined as the force multiplied by the virtual distance δd.

$$\delta W = \delta W_i - \delta W_o$$

$$\delta W_i = F_i \delta d_i$$

$$\delta W_o = F_o \delta d_o$$

Combining these equations results in the general equation for the energy in a system in equilibrium [15].

$$0 = \delta U - F_i \delta d_i + F_o \delta d_o$$

The mechanical advantage MA is defined as the instantaneous ratio between the output force F_o and the input force F_i.

$$MA = \frac{F_o}{F_i} = \frac{1}{\delta d_o}\left(\delta d_i - \frac{\delta U}{F_i}\right) \tag{5.2}$$

A simple example can be seen in figure 5.1. In this rigid body mechanism there are no elastic elements, therefore the strain energy U is equal to zero. Equation (5.3) can then be simplified to the following expression for the mechanical advantage for a rigid body mechanism. The mechanical advantage of our example mechanism can be expressed in the lengths of the mechanism.

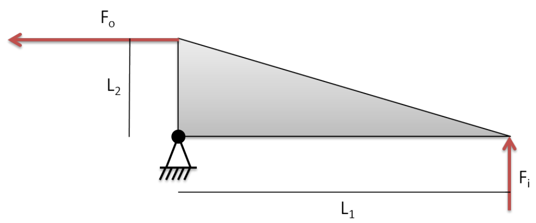

Figure 5.1: Example of mechanical advantage of a rigid body mechanism. No energy will be stored in a rigid body mechanism.

$$MA_R = \frac{F_o}{F_i} = \frac{\delta d_i}{\delta d_o} = \frac{L_1}{L_2}$$

In a compliant mechanism however the strain energy U cannot be neglected. This strain energy is the energy stored inside the system, resulting in a lowered mechanical advantage. An example of a compliant mechanism is shown in figure 5.2.

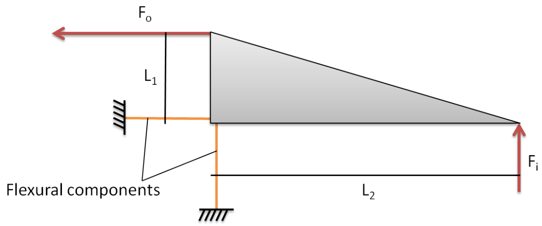

Figure 5.2: Example of mechanical advantage of a compliant mechanism. The flexible members will store energy, which will affect the energy transfer. The input/output ratio is changed depending on the potential energy stored in the flexible members.

The mechanical advantage for the compliant system then includes the strain energy. This equation can be rewritten to include force F_C, representing the force required to displace the mechanism alone, without any work done.

$$MA_C = \frac{\delta d_i}{\delta d_o} - \frac{\delta U}{\delta d_o F_i} = MA_R \left(1 - \frac{F_C}{F_i}\right) \tag{5.3}$$

As can be observed the mechanical advantage of the mechanism is lowered for increasing strain energy stored. This means that a stiffer mechanism, e.g. thicker flexural components, will lower the mechanical advantage of the system. Another observation is that a compliant mechanism without any stiffness would have a mechanical advantage equal to its rigid body counterpart. This is caused by the fact that compliant mechanisms without stiffness (statically balanced mechanisms) by definition have a constant strain energy.

5.2. STATIC BALANCING

In order to maximize the mechanical advantage for a compliant mechanism, the term δU should remain equal to zero: the energy stored in the system will remain constant. This leads to a mechanism that transfers all the energy from the input to the output, identical to a rigid body mechanism. A compliant mechanism that has a constant energy level is called a statically balanced compliant mechanism.

MECHANICAL ADVANTAGE OF SUSPENSION

The same analysis can be performed for the compliant suspension of the gear. Here however the motion of the ring plays an important role. Key again is to design a compliant mechanism that has a constant energy level throughout the entire motion path. In the case of the compliant ring suspension however the motion path is different than in the previous example; a circular path is imposed on the ring. Or formulated differently, a path is described with a certain constant radius.

Firstly lets have a look at a greatly simplified model of the suspension (figure 5.3). The compliant suspension design following from the FACT method can be represented by two springs perpendicular to each other, and connected via an intermediate body (body 1). In this simplified system we assume that the intermediate body and the body at the endpoint (body 2) can only translate, and do not allow for a rotation. In reality the suspension will result in a high rotational stiffness for these bodies.

Another important notice is that the springs in the model are so-called linear zero-length springs. Zero-length springs have a force-deflection curve that passes through the origin. Also the springs do not have any initial length, that means that they start exerting a force as soon as they are elongated (starting from an initial length of 0). This seems unrealistic, however the compliant parallel guidance behaves as a zero-length spring. Using traditional coil springs this system would however be hard to construct because of the need for this zero-length behaviour.

We know that the endpoint of the suspension, the ring gear, will move in a circular path. By prescribing a circular path on the endpoint of the system the strain energy U stored in the system can be calculated. Figure 5.3(b) shows how this circular path is defined. The angle θ is then used to define the position of body 2, and thus the elongation of spring 1 and 2.

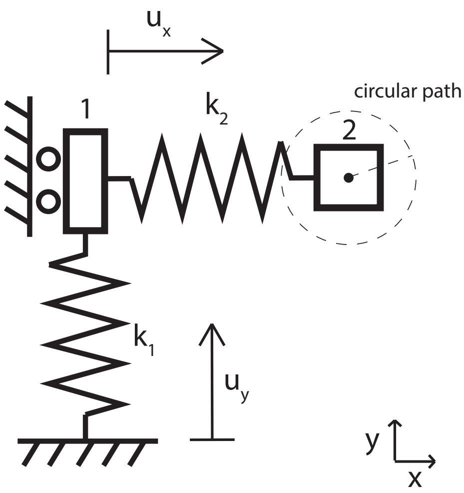

(a) Simplified model of suspension to analyse the energy stored in the suspension depending on the input motion. The motion path is the result of the circular translation of the annulus.

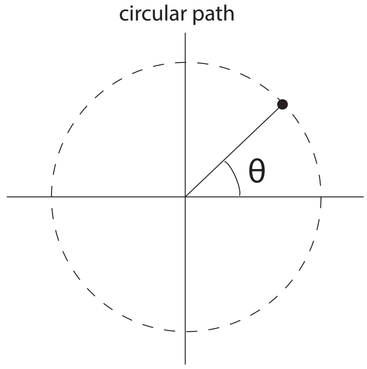

(b) Defining the circular path for body 2.

Figure 5.3: A simplified model of the suspension to analyse the mechanical advantage of the system throughout the working positions.

This circular displacement imposed on body 2 can then be represented by a combination of translations in x- and y-direction:

$$x = e\cos(\theta)$$
$$y = e\sin(\theta)$$

Here e stands for the radius of the circular path imposed on body 2. Note that since bodies 1 and 2 cannot rotate, the displacement in x-direction will only result in deformation of spring 2, and a displacement in y-direction will only affect the elongation of spring 1. With this input motion we can derive the strain energy U stored in the two springs. First the strain energy for the first spring:

$$\begin{aligned} U_1 &= \frac{1}{2}k_1 u_y^2 \\ &= \frac{1}{2}k_1 e^2 (\sin\theta)^2 \end{aligned}$$

And the strain energy for the second spring:

$$\begin{aligned} U_2 &= \frac{1}{2}k_2 u_x^2 \\ &= \frac{1}{2}k_2 e^2 (\cos\theta)^2 \end{aligned}$$

We know that the total strain energy in the system can be calculated by adding the strain energies for both systems together.

$$\begin{aligned} U_{total} &= U_1 + U_2 \\ &= \frac{1}{2}k_1 e^2 (\sin\theta)^2 + \frac{1}{2}k_2 e^2 (\cos\theta)^2 \end{aligned}$$

In the case where both $k_1 = k_2 = k$ we observe something interesting:

$$U_{total} = \frac{1}{2}ke^2\left((\sin\theta)^2 + (\cos\theta)^2\right)$$

The term between brackets can be simplified further since:

$$(\sin\theta)^2 + (\cos\theta)^2 = 1$$

This results in a constant strain energy over the entire circular path.

$$U_{total} = \frac{1}{2}ke^2$$

Since the strain energy in the system is constant, this means that the δU is equal to zero. The efficiency of the system will therefore not be affected by changes of the strain energy stored in the system, since this is constant. This means that all the work W done on the system will be transferred to the output, resulting in an optimal efficiency for this mechanism.

Of course this is in an optimal case. The efficiency of the actual system will be dependent on several factors, such as the degree of balancing that can be obtained due to errors.

An interesting observations is made that the stiffness does not need to be positive for the system to be statically balanced. A negative stiffness will result in a balanced force reaction force in opposite direction. As long as the stiffness follows a linear profile, the suspension will be balanced when moving over a circular path.

Another important note is that the springs in figure 5.3 are so-called zero-length springs. Meaning that at they have a reaction force equal to zero when their length is equal to zero. For coil springs, as depicted in the figure, this is hard to realise. However flexure beams, which will replace the springs depicted in figure 5.3, such a feat is not difficult to realise. For small deformations (linear domain) the flexure beams will behave as zero-length springs, and thus will result in a balanced system, as will be shown using an computer models later.

5.3. EFFICIENCY GEAR CONTACT

A cycloid path can be visualized by tracking a point on a rolling cirle. If this circle happens to be rolling on the surface of another circle we call it a hypocycloid or epicycloid path (figure 5.4).

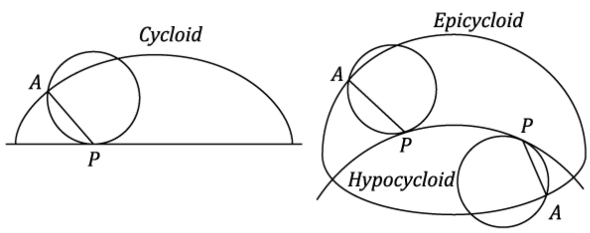

Figure 5.4: Visualization of a cycloid path. The positions of point A can be formulated using equations, which makes it convenient for design of a gear profile. Also a pure rolling gear contact will be the result by definition.

The path that this point on the rolling circle traces can be formulated as follows [16].

$$C_x = R\cos\phi - R_r\cos(\phi-\psi) - e\cos\big((N)\phi\big) \tag{5.4}$$
$$C_y = -R\sin\phi + R_r\sin(\phi-\psi) + e\sin\big((N)\phi\big) \tag{5.5}$$

Where

$$\psi = -\arctan\left[\frac{\sin\big((1-N)\phi\big)}{\frac{R}{eN} - \cos\big((1-N)\phi\big)}\right]$$

here R represents the radius of the circle over which is rolled. R_r represents the radius of the rolling circle. N stands for the number of cylinders in the ring gear and e is the eccentricity of the point on the rolling circle.

These are the general equations for the profile of the cycloidal path. These general formulas need some additional constraints before they can be used to generate useful profiles for cycloidal gear profiles. Hwang et al. [17] have devoloped the undercutting and design constraints for generating a useful cycloidal gear profile. These constraints are based on simple geometric analysis of the gear profile. Imposing these constraints on the equation for the cycloidal profile results in a set of useful profiles for the gear.

First of the constraint for the size of the rollers. The radius of the rollers cannot be equal to zero. The rollers should also not be too big that they do not fit in the ring gear. These two end-points result in a range for the radius R_r of the rollers:

$$0 < R_r < R\sin\frac{\pi}{N}$$

From this constraint follows the design constraint for the 'pin radius ratio' Q, a parameter defined by Hwang et al. [17]. This parameter is defined as the ratio between the radius R of the gear and the radius R_r of the rollers ($Q = \frac{R_r}{R}$).

$$0 < Q < \sin\frac{\pi}{N} \tag{5.6}$$

In the equation above the N represents the number teeth on the ring gear, that is the number of rollers.

The constraint for Q is to avoid interference between any of the two neighbour pins. The following constraint is aiming at defining the region where no undercutting of the profile occurs. For this purpose the 'eccentric ratio' parameter P ([17]) is defined. The 'eccentric ratio' is defined as the ratio between the eccentricity e and the radius R of the central gear ($P = \frac{e}{R}$). The parameter P is constrained as follows:

$$0 < P < \frac{m}{N}$$

In this equation m represents the number of tooth difference between the inner and outer gear. Since we want to maximize the ratio, the tooth difference is chosen equal to 1. The above constraint for P then simplifies to:

$$0 < P < \frac{1}{N} \tag{5.7}$$

Imposing constraint equations (5.6) and (5.7) on the equations to form the cycloidal profile equation (5.11) gives us a set of feasible cycloidal gear profiles. From this set of profile the most suitable design can be chosen based on other criteria, the most important one being the efficiency.

The equation for the rotor profile and the corresponding constraints are implemented in a Matlab model to easily find the feasible rotor profiles. These profiles will then be subjected to a calculation to find the optimal design in terms of efficiency, which will be elaborated on in the following paragraphs.

EFFICIENCY BASED ON EXISTING LITERATURE

An equation for the efficiency of a cycloidal gear profile is found in literature [13]. Note that this formula is derived for a cycloid drive, not for the novel system, but it could give some insight. The functional parts of the cycloid drive for which Jonathan W. Sensinger derived the formulas for the efficiency is depicted in figure 5.5. A key difference is the fact that a cycloid drive uses a eccentric cam on the input to achieve the wobbling motion of the ring gear. In the novel design this wobbling motion is the output of the system, and is achieved by the gear profile itself. The contact between the two gears is also different in the cycloid drive vs. the proposed compliant version. The use of compliant members results in an in-plane stiffness of the ring gear, resulting in a contact force on the gear profile.

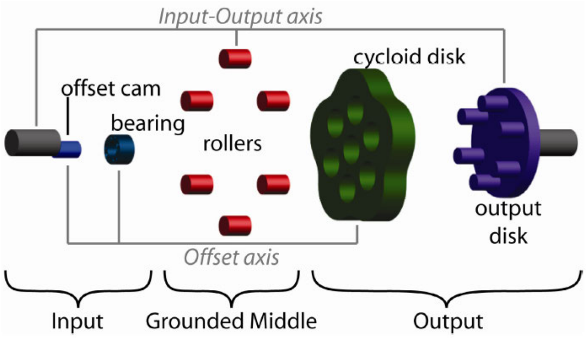

Figure 5.5: Functional parts of the cycloid drive [13]. An eccentric cam forces the cycloidal disc to the outside where it makes contact with a set of rollers. As a result the cycloidal disc will make a wobbling motion where it rotates slowly with respect to the rollers, due to a one-tooth difference (in this image). The slow rotation is captured by the output disk.

In figure 5.5 a set of rollers is depicted. Since we are miniaturizing its difficult to fabricate and assemble these rollers, therefore the rollers will be replaced by a cylinders fixed to the ring gear. Sensinger also gives a formula for the efficiency of this case without rollers, but instead having the 'rollers' fixed to the ring gear:

$$\eta = 1 - \mu \frac{C}{2\pi} \frac{1}{eN} \tag{5.8}$$

In this equation μ stands for the friction coefficient. C represents the circumference of the rotor, and thus the distance over which sliding occurs. Eccentricity e stands for the radius of the eccentric cam. N represents the number of rollers in the ring gear, and in the case of a one-tooth difference between the inner and outer gear, N is equal to the achieved gear ratio.

A grid search is performed using a range for the input parameters of equation (5.11) that lie within the feasible range considering the design space. The radius R of the cycloidal rotor is fixed based on the dimensions of the barrel spring: this diameter is needed to fit the main spring. A larger cycloidal rotor would not be desired since the volume of the watch is limited. The eccentricity e of the profile is fixed as well, since this parameter will determine the range of motion of the output shuttle. A range of motion of 300μm is chosen for the input of the translational output, being used as input for another transmission stage. The radius of the rollers R_r depends on the optimal efficiency, and thus a wide range is selected. The ratio of the gear pair needs to be higher than 10, resulting in a minimal number of rollers N when a 1-tooth difference between cycloidal rotor and annulus is used.

An interesting observation made when studying equation (5.8) is that for an increasing value of N, the efficiency will improve. Since N represents the number of rollers in the cycloidal gear pair, this means that for an larger ratio, a higher efficiency is achieved. Of course the larger value for N will also impact the circumference of the rotor, so there will be a limit to the increased efficiency.

The gridsearch yields an optimal efficiency of η = 61% for the ranges shown in table 5.1. The optimal parameters are shown in table 5.2. An interesting observation is that this equation gives higher efficiencies for an increasing N, for certain ranges. This means that the efficiency will increase to a certain point with an increasing ratio for the gear pair.

Table 5.1: range for parameters rotor shape

Parameter	Symbol	Unit	Value
Radius central gear	R	[mm]	7
eccentricity	e	[mm]	0.3
Radius rollers	R_r	[mm]	$0.2-2$
Number or rollers (= gear ratio	N	[-]	$11-25$

Table 5.2: Parameters following the gridsearch performed

Parameter	Value
R	7
e	0.3
Rr	0.4
N	23

SENSITIVITY

As can be seen in figure 5.6, the efficiency according to the formula from literature is not very sensitive to the two parameters that are left to perform the gridsearch.

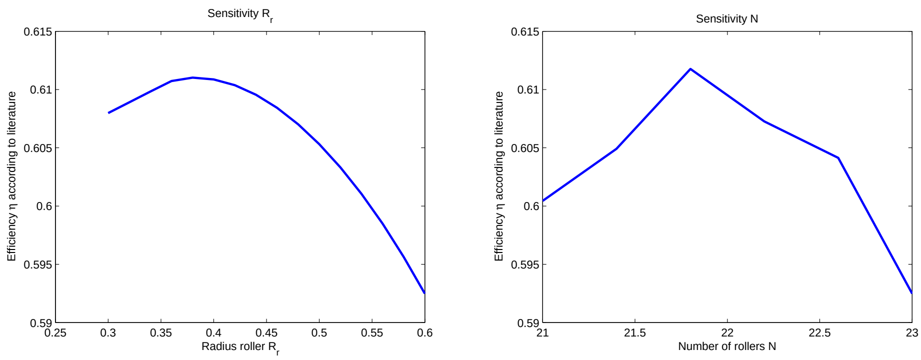

(a) Sensitivity of efficiency to parameter R_r around optimum according to formula equation (5.8).

(b) Sensitivity of efficiency to parameter N around optimum according to formula equation (5.8).

Figure 5.6: Sensitivities of efficiency according to literature to parameters for the cycloidal profile.

5.4. FRICTIONAL LOSSES DUE TO STIFFNESS

With this equation we can find the most efficient shape for the gear profile. However does this formula represent the our system? Several key aspects of the novel design are not taken into consideration, such as the in-plane stiffness of the suspension. This stiffness will increase the normal force between the central gear and the ring gear, resulting in a higher friction force.

This section aims at identifying the effect of the ring gear having an in-plane stiffness. For doing this several assumptions are made beforehand. The first is the assuming a single point contact between the two gears. In reality the contact will most likely occur at two or more locations simultaneously.

The second simplification is neglecting the input torque for this equation. Only the reaction force as a result from the stiffness of the suspension is taken into consideration. It can be expected that the input torque will increase the normal force, therefore deteriorating the efficiency. However because of the multiple contact points in the actual case it is hard to determine the added normal force as a result of the input torque.

To get an estimation on the magnitude of this sliding loss a model was made in Matlab. For this model a single contact point is assumed. All reaction forces work on this single point. In reality there are multiple contact points expected between the gear couple, but reducing the number of contact points to one will give an order of magnitude for the energy loss.

As mentioned above the input torque is delivered by the central gear. This gear has a cycloidal gear profile as described in a previous chapter (equation (5.11)). The energy loss in the system is the result of the sliding motion between this central gear and the ring gear.

$$C_x = R\cos\phi - R_r\cos(\phi-\psi) - e\cos\big((N)\phi\big) \tag{5.9}$$
$$C_y = -R\sin\phi + R_r\sin(\phi-\psi) + e\sin\big((N)\phi\big) \tag{5.10}$$

Where

$$\psi = -\arctan\left[\frac{\sin\big((1-N)\phi\big)}{1}\right] \tag{5.11}$$

The model is based on the equations for the rotor profile. An example of a rotor profile is shown in figure 5.7. The contact force between the gears will be the result of the reaction force from the suspension stiffness and from the imposed input torque.

Lets start with the resultant force from the suspension stiffness. From the Ansys simulation can be concluded that the resulting force is pointing towards the center of the central gear (origin in Ansys) at every displacement location. Also the magnitude of this reaction force is constant for a displacement with a constant radius.

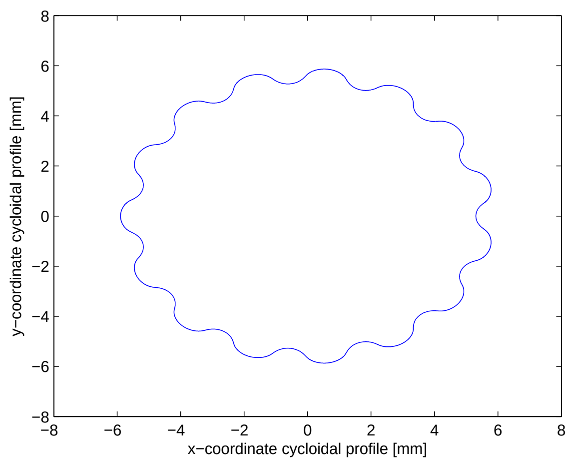

Figure 5.7: Example of a generated cycloidal profile using aforementioned equations for the cycloidal rotor.

In the Matlab model therefore a reaction force vector is defined containing the direction of the reaction forces at every point on the cycloidal profile. Several of these forces are shown in figure 5.8. In the model a reaction forces is defined for each gear profile coordinate, resulting in a force vector with a length of about 6300.

The normal forces of each of these reaction forces is dependent on the contact angle between the gear profile circumference gradient δC. Figure 5.9 shows how the normal force is determined by the reaction force and

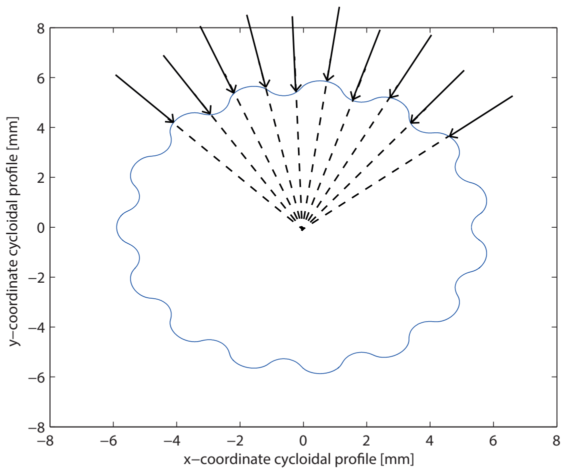

Figure 5.8: Suspension reaction forces acting on the cycloidal gear profile.

the angle θ. The reaction force F_s is the result of the counter force from the suspension. This force can be calculating by multiplying the stiffness k of the suspension with the distance over which it is displaced, in our case this distance is equal to the eccentricity e of the cycloidal profile.

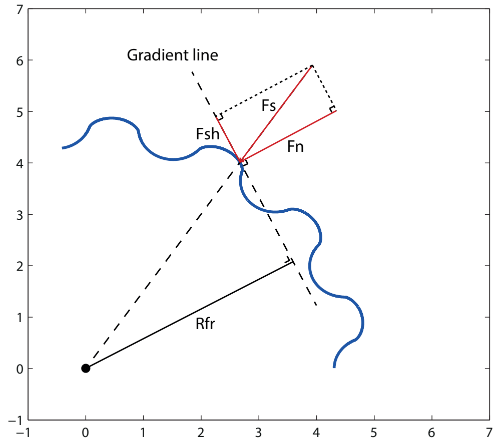

Figure 5.9: Normal force as a result of surface gradient will cause a friction force with a magnitude dependent on the cycloidal surface angle and the friction coefficient μ.

Assuming a Coulomb friction for the gear contact the friction force can be directly calculated from the normal force. The friction force F_{fr} is dependent on the friction coefficient μ between the two gears. The friction coefficient μ depends on the materials used and whether or not they are lubricated. For now a safe guess of 0.3 is used for calculations for the frictional losses. The friction force acting on the corresponding moment arm results in a moment about the central axis. This moment represents the lost work as a result of the increased normal force from the stiffness of the suspension.

$$F_{fr}(\phi) = \mu F_n(\phi)$$

To calculate the energy loss from the calculated friction force we need to know the travelled distance. The total travel distance is equal to the circumference of the central gear. To calculate the total energy loss we need to integrate the energy loss between every coordinate on the gear profile.

$$W_{Loss} = \int_0^{2\pi} F_n \cdot \mu \cdot R_{fr}(\phi) \cdot \delta C(\phi) d\phi,$$

The solution of the integral above is approximated by a sum and implemented in Matlab. This way the energy loss per cycle can be calculated by implementing the input parameters for the gear profile, the reaction force as a result of the suspension and the friction coefficient between the gears.

DRIVING TORQUE

Assuming a case where no load is applied on the translating output shuttles, the system already requires a certain torque to overcome the aforementioned frictional forces. This torque is the result of the friction force F_{fr} multiplied with the moment arm of this force. Note that the direction of the friction force, and thus the corresponding moment arm, depends on the cycloidal profile.

This calculated energy loss will be compared to the known input energy to estimate the percentage of energy lost for each cycle, and thus give an approximation of the efficiency of the system. The input energy is derived from measurements done on a barrel spring(figure 5.10). These numbers may vary per barrel spring type, but will put the calculated energy loss in perspective.

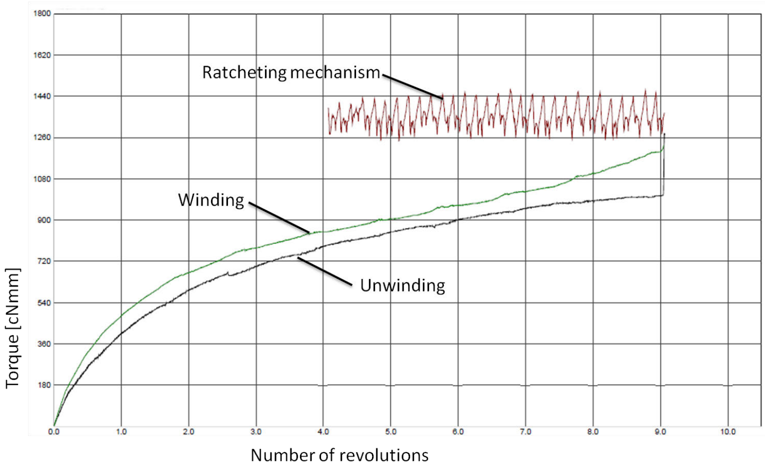

Figure 5.10: Example of the torque measured on the barrel gear. This data is provided by partner TAG Heuer, and is measured on an barrel gear system actually in use.

Not the entire range of the barrel spring can be utilized. Lets only assume the range between 630 and 1080 $cNmm$. The input energy per single rotation of the barrel spring is calculated as:

$$E_{in} = \frac{10.8 + 6.3}{2} = 8.15e^{-3} Nm$$

The frictional loss due to stiffness can then be compared to the available input torque:

$$\eta = \frac{E_{in} - W_{loss}}{E_{in}}$$

Note that this does not incorporate power transfer, thus the efficiency η will be a best-case scenario. It will however give an indication of the fraction of energy lost due to the stiffness of the compliant suspension compared to the available input energy.

Taking the parameters of the fabricated silicon prototype for the cycloidal rotor profile, and plotting the moment as a result of the friction forces results in the following plot, figure 5.11. The parameters of the cycloidal rotor are $R = 5.2mm$; $e = 0.295mm$; $R_r = 0.6mm$; $N = 16$. The cycloidal profile corresponding to this graph is shown in figure 5.12. The corresponding stiffness of the suspension of 0.02214N/mm is used for the calculation of the expected no-load torque profile shown in figure 5.11. In figure 5.11 the resulting moment is plotted using a friction coefficient $\mu = 0.3$. Note that the magnitude of this torque fluctuates as a result of the contact angle between the force from the suspension and the cycloidal profile. Also the magnitude of this moment as a result of a friction force is very small compared to the available input torque.

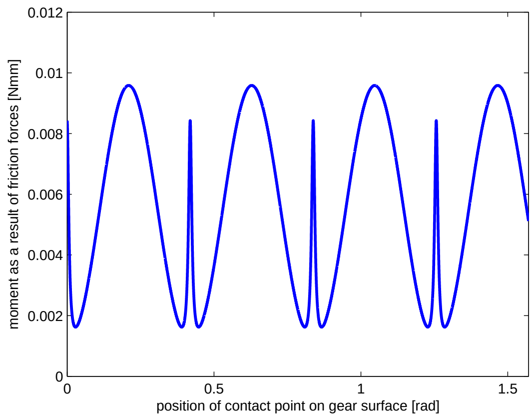

Figure 5.11: Moment as a result of friction forces due to suspension stiffness, plotted for a quarter of the profile. The moment is the result of the friction force F_{fr} multiplied with the moment arm R_{fr} in figure 5.9

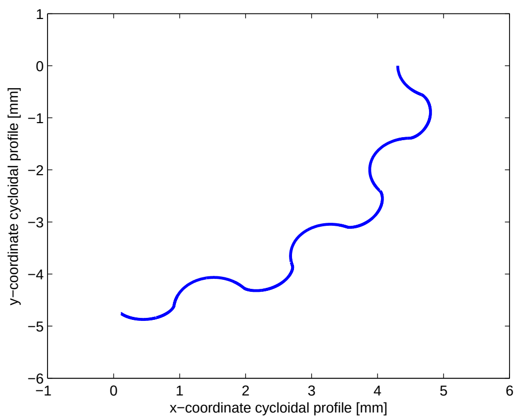

Figure 5.12: Profile corresponding to the plotted moment of figure 5.11

SENSITIVITY

Again the sensitivity around the optimal gear parameters mentioned in section 5.3 are checked, this time using the method of estimating the frictional loss as previously discussed. Note that the stiffness of the suspension plays an important role for the magnitude of the frictional losses. It does however not change the trend of the energy losses. For the plots shown in figure 5.13 a stiffness of 0.087N/mm is used. This stiffness value comes from the new design, including an applied load, see chapter 2.

5.5. NEGATIVE STIFFNESS

One possibility is to use a suspension with a negative stiffness in all directions. A suspension with a negative stiffness would be beneficial for the design for two reasons:

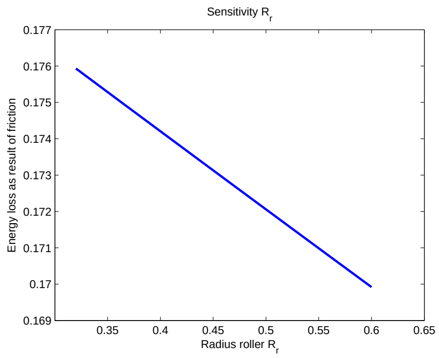

(a) Sensitivity of efficiency to parameter R_r around optimum using estimation of frictional losses based on the stiffness of the suspension.

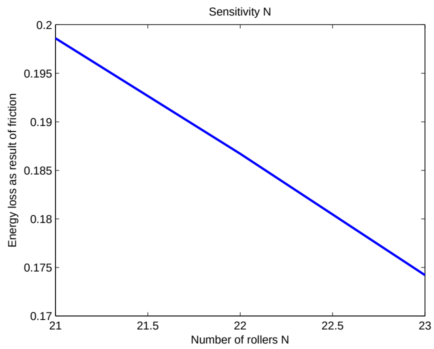

(b) Sensitivity of efficiency to parameter N around optimum using estimation of frictional losses based on the stiffness of the suspension.

Figure 5.13: Sensitivities of parameters of gridsearch around optimum based on force analysis of system.

- negative stiffness can guarantee contact
- negative stiffness will result in higher efficiency (reduced sliding loss)

Following the reasoning to use a ring gear with internal teeth to be suspended, we can conclude that a negative stiffness for the suspension would result in a contact between the gears. The negative stiffness will try to push the ring gear away from the center, resulting in a contact between the gears. A positive stiffness will want to remain in the central position of the suspension, therefore another mechanism is needed to guarantee contact.

Also the position of contact between the two gears will be beneficial. This will be more apparent when compared to the other solution to guarantee contact: a cam mechanism combined with a positive stiffness. The cam mechanism will have a lot of sliding due to the location of the contact between the gears. The negative stiffness suspension on the other hand will result in a mainly rolling contact between the gears. A mostly rolling contact will result in a lower energy loss due to friction.

Theoretically a suspension with a negative stiffness is desired over the other solutions. Therefore lets check this approach first to see if it is a feasible one.

ANSYS MODEL

A model was created to check on the feasibility of using two bistable elements placed perpendicular in a rigid framework. The idea is that the linear negative stroke will create a balanced system, just like we have seen with a linear positive system. For the model similar dimensions are used as for the system with a positive stiffness, to make the results comparable. A thickness of 30μm is implemented. This is the minimal thickness that can be produced, a thinner flexure resulting in a lower stress. The stress will be the critical point in the design as we will see later. After fabrication we will also see that the actual thickness is thinner than 30μm as a result of the silicon fabrication process (DRIE).

The length of the bistable flexures is chosen to be 7mm, comparable with the flexures in the positive stiffness model, able to fit in the defined design space.

The angle of the flexures in the bistable system determines the range of the negative stiffness and the magnitude of the stresses. Several runs are performed to see what the optimal angle for the bistable elements is. Based on the result of these simulations the feasibility of using a negative stiffness suspension will be evaluated.

With increments of 10μm the position is determined where the zero-force point of the suspension is. This means the point where both bistable elements are in there unstable zero-force position.

Different simulations were performed, varying the angle of the flexures only. A steeper angle will result in a longer range of linear negative stiffness, however a higher stress. A smaller angle will result in a lower stress,

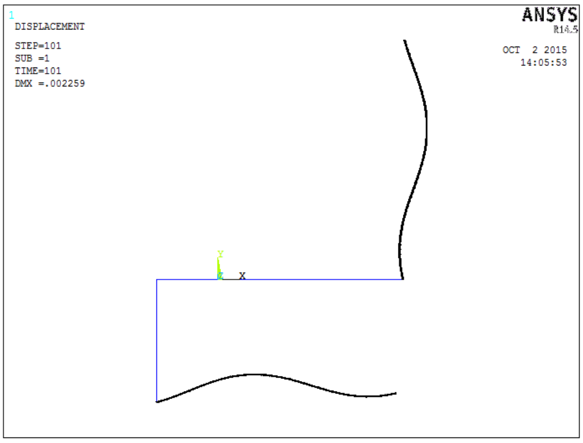

Figure 5.14: Screenshot of negative stiffness model in Ansys. First the rigid stage is positioned in the center of the negative stiffness beams (the unstable equilibrium point). Then a circular motion is traced similar to the model with a positive stiffness.

but a system much more sensitive to misalignment of the suspension position. Also the degree of static balancing greatly depends on the angle of the flexures, as can be seen in figure 5.15.

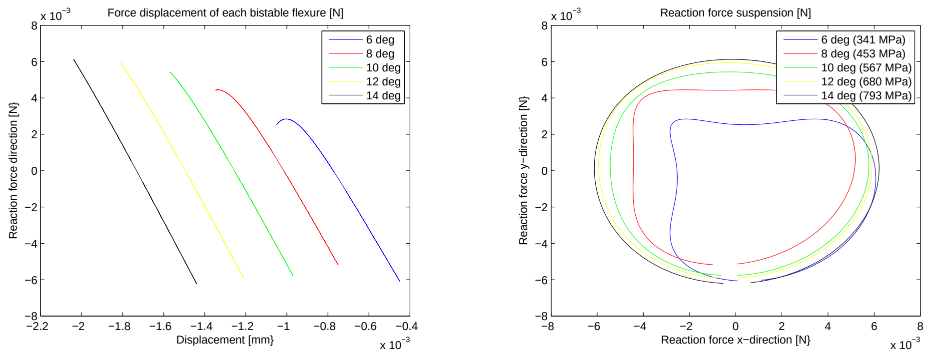

(a) Individual force deflection negative stiffness elements from Ansys model.

(b) Reaction forces from Ansys model. Combination of two bistable beams mounted perpendicular.

Figure 5.15: Results from simulation Ansys negative stiffness. Static balancing using negative stiffness (bistable) elements is possible, however not feasible due to high stresses. Sharper angles of the bistable beams will result in a longer linear negative stiffness range, but also increase the stress level.

As can be seen from the plots, all of the stresses for each are way too high (200 MPa design stress limit). Also as expected the higher the angle of the bistable beams, the better the static balancing. From these simulations can be concluded that bistable beams cannot be used as a method to generate a negative stiffness suspension in Silicon on this scale. A beam length of 7mm is already going to be a tight fit considering an additional suspension is required to deal with the rotational stiffness. The stresses cannot be lowered by using a thinner beam profile, since 30μm already is the thinnest beams that can be produced using this technique (with this manufacturer).

5.6. ANSYS MODEL

To verify the predictions of a statically balanced mechanism in x- and y-directions an Ansys model was created. Note that the design in figure 5.16 is rotationally symmetric. The modelling therefore only consists of half the design, which will then copied and rotated to form the other side of the suspension.

Flexural elements The model is build up starting from the position of the endpoints of the flexures. The endpoints of the flexures are defined as keypoints in Ansys, as can be seen in figure 5.17. In this model several

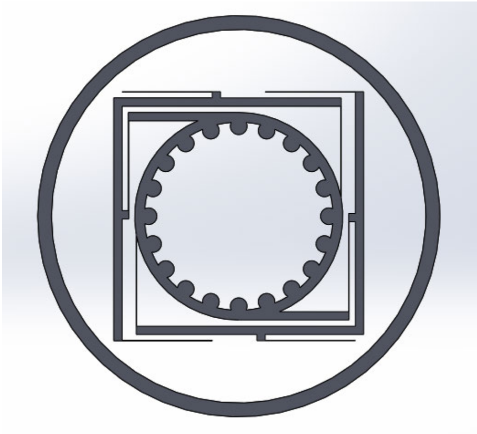

Figure 5.16: CAD model to explain following definitions of the model implemented in Ansys.

lengths are defined for modelling. The length of flexures $1-4$ are identical and named L_f. The vertical offset of flexures 1 & 2 with respect to the origin (keypoint 1) is named L_{off1}. The horizontal offset of flexures 1 & 2 with respect to the origin is named L_{off2}. The length of the intermediate stage (L_{int}) and ring stage (L_r) result in the distance between the parallel flexures.

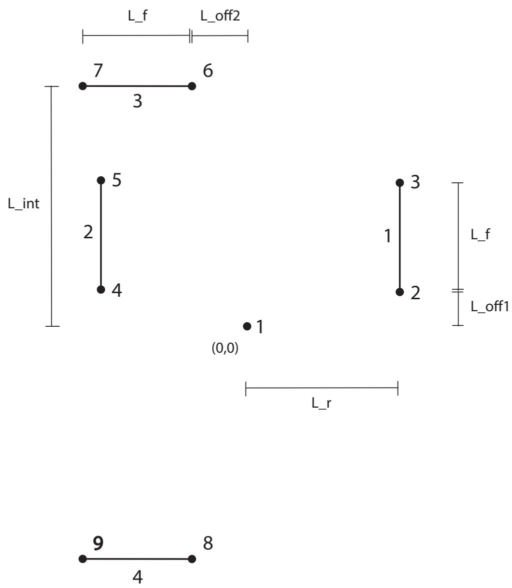

Figure 5.17: Position of the flexures defined by keypoints in Ansys.

The position of the flexure elements is now defined. Note that this is a single side of the suspension. Copying the defined keypoints and rotating the entire system over an angle of 180 degrees results in the position of the mirrored suspension.

The flexures $1-4$ are each build up out of 20 elements of the BEAM188 Elements Type. A thickness of $30\mu m$ and a width of $500\mu m$ is assigned to this element. Since this model will be made in silicon, an anisotropic material, the E-module is dependent on the direction. For this purpose different parameters are defined for the material properties in x- y- and z-direction (table 5.3).

As a result of the edging process of silicon the edges of the design are not perfectly straight. The thin flexural beams are especially affected by a change in the cross-section. Therefore instead of using a rectangular cross-section for the thin beams a modified cross-section is implemented. This shape can vary per fabrication method, and can vary even per manufacturer. The cross-section shape is adjusted by evaluating previous silicon samples with an electron microscope. The model is corrected according to these SEM images.

Table 5.3: Anisotropic properties of silicon implemented in Ansys

material direction	x	y	z
Elastic modulus [GPa]	169	169	130
Poissons ratio [-]	0.064	0.36	0.28
Shear modulus [GPa]	50.9	79.6	79.6

Rigid elements The flexures are connected to the ring gear, intermediate body and ground. These parts of the design are much thicker than the flexural elements. These parts can be approximated by a rigid element since their stiffness is orders of magnitude higher than that of the stiffness of the flexures. By using an element that cannot deform the calculation time is vastly reduced since these elements are eliminated from the costly finite element analysis. The MPC184 element is designated to the rigid parts of the design, giving these parts an 'infinite' stiffness.

As a result of using a rigid element, the shape of the bodies leaves the simulation unaffected. The geometry of the rigid parts does not matter, as long as their connection points with the flexural elements are defined properly. Taking a close look at figure 5.16 shows where the flexures are connected to the rigid parts. These connection points are connected with the MPC184 element (figure 5.18).

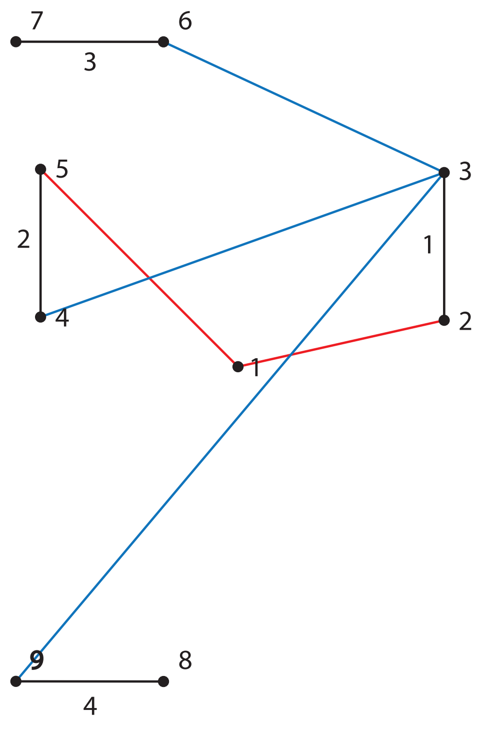

Figure 5.18: Modelling of rigid parts using MPC184 element in Ansys. Red = ring gear, blue = intermediate body.

Constraints The model will be connected to the ground via flexures 3 & 4 (figure 5.18 and their mirrored counterparts (not shown). These are the only constraints imposed on the model (figure 5.19). Note that on nodes 7 & 8 all degrees of freedom are constrained (3 translations and 3 rotations).

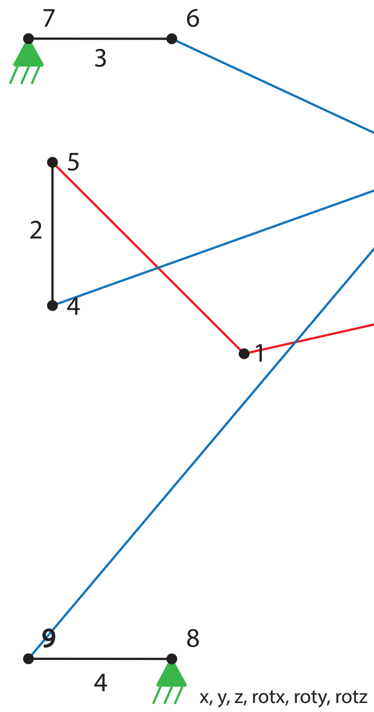

Figure 5.19: Model constraints as result of connection to ground (green). The ground is represented by a constraint in all directions and all rotations.

Inputs for the model The inputs for the model can be subdivided in two categories; input displacements and input forces. Both of these categories can be switched on and off for different analyses.

Displacements The ring gear will be assembled in conjunction with a central gear. The two gear profiles are designed with a certain eccentricity parameter e, which translates directly to the radius of the circular path over which the ring gear will translate. The ring gear will therefore be displaced as a result of a contact force acting between the central gear and the ring gear. The Ansys model does not take the geometry of the gear into account. However the displacement of the ring gear as a result of this geometry will be modelled. Therefore the displacement on the ring gear as a result of the eccentricity parameter is imposed on the body representing the ring gear (red lines in figure 5.19). Note that only the x- and y-displacement are imposed on keypoint 1, all rotations are left free.

Multiple displacement coordinates are defined on a circle as seen in figure 5.20 and the model is solved for each of them. For every displacement a static analysis is done to reveal the reaction forces as a result of the stiffness of the suspension. This will give the in-plane stiffness (x- and y- direction) of the suspension.

Note that by picking a point on the ring gear to define a displacement, this point automatically becomes a revolute joint for the body representing the ring gear. In reality the ring gear does not have a revolute joint.

Forces But there are more forces in play than only the reaction forces as a result of the stiffness. The central gear is also applying a torque on the ring gear as a result of the torque of the barrel spring. The location and direction of this force changes as a result of the motion of the ring gear. The distance from the center however is always the same: this is equal to the radius of the central gear. Note that this distance is independent on the eccentricity of the motion of the ring. Thus the location of the applied forces is relative to the origin of the model, not to the center of the (moving) ring gear. For this reason a number of rigid links (MPC184 element) is generated in the model to define the location of the applied force for each time step (and thus each displacement). A screenshot of the model as inplemented in Ansys can be seen in figure 5.21.

The forces applied on the specified locations are the result of the input torque applied by the barrel spring

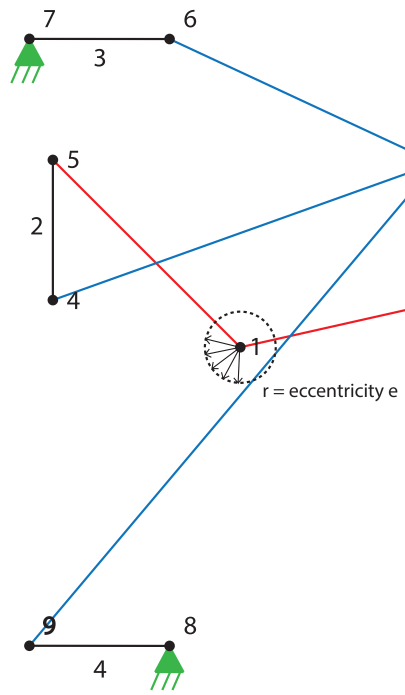

Figure 5.20: Input displacement x- and y- direction as result of eccentricity e of the cycloidal rotor profile.

divided by the radius of the central gear. The direction of the forces is therefore in the tangential direction of the input gear. To apply a pure moment, the calculated force is halved and applied on both sides on equal distance from the center of the central gear, in the model defined by the origin (figure 5.21).

$$F_{in} = \frac{M_{in}}{R} \tag{5.12}$$

A screenshot of the model including the applied forces is shown in figure 5.21. Note that the location of the applied forces will change as together with the displacement location.

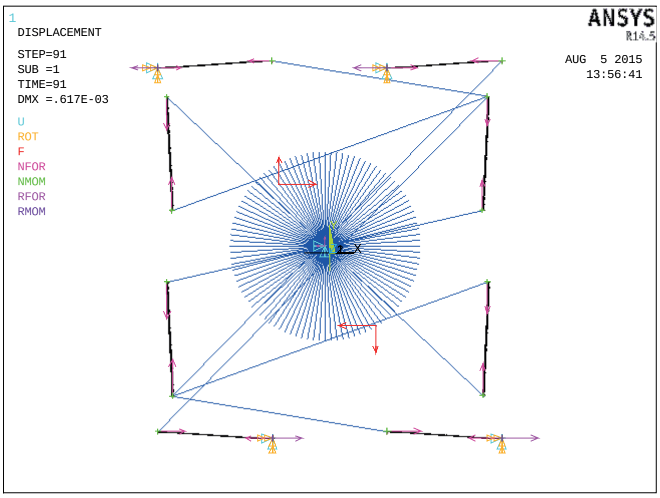

Figure 5.21: Model of suspension including the applied constraints an input forces. Identical results are obtained for a single applied moment on the center, or equivalent applied force acting on a radius as depicted in the figure.

The resulting forces are then simulated at a series of positions in the circular path of the ring gear. The forces are then read into Matlab where the results are processed. By plotting the resulting reaction force over the radial position of the circular path, the resulting stiffness can be visualized that the input axis will 'feel' when driving the system.

RESULTS

From this model some interesting behaviour is observed. The same trends show up during all simulations. Some further modelling is required to explain the shown behaviour.

The first interesting finding is periodic fluctuation in the stiffness of the suspension (figure 5.22. The reaction force differs for different positions of the circular path. This finding is not in line with the expectation of a statically balanced suspension. Another observation is that the magnitude of the reaction force is dependent on the torque applied to the suspension. The higher the torque, the more the suspension is pulling the ring back towards the centre (and thus in contact with the central gear). As a result the efficiency will be dependent on the input torque.

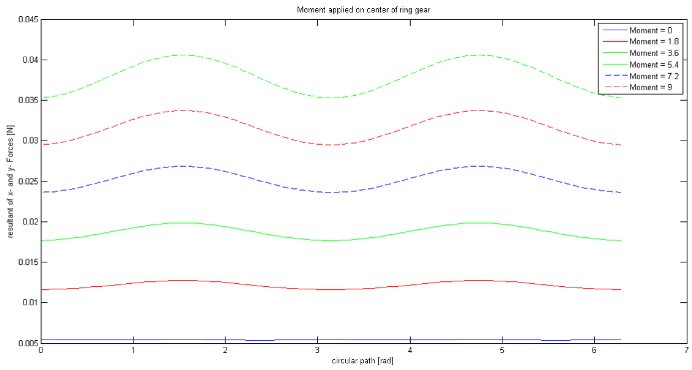

Figure 5.22: Results from Ansys modelling. The stiffness is dependent on the position of the suspension, hence not optimally balanced. Also the stiffness linearly depends on the load (moment) applied on the center of the annulus.

The difference in stiffness becomes apparent in the plot in figure 5.22. The suspension is moved over different radii, one simulation with a moment applied, the other time without any moment. The increase in stiffness is apparent when looking at the spacing between the individual red lines, and individual blue lines.

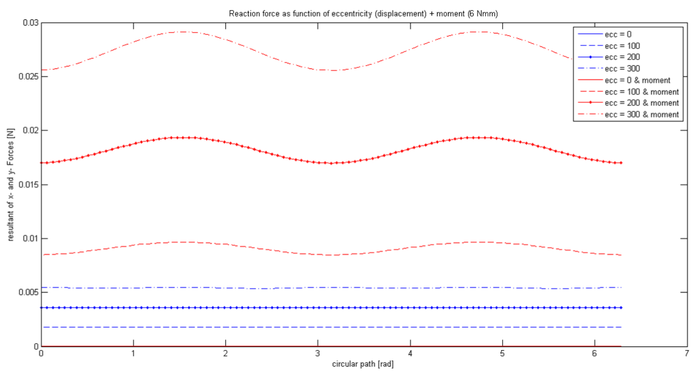

Figure 5.23: Results from Ansys modelling. The stiffness is dependent on the position of the suspension, hence not optimally balanced. Also the stiffness linearly depends on the radius of displacement of the suspension while a load is applied to the center of the annulus.

5.7. FREE-BODY-DIAGRAM

To get a better understanding on the findings from the Ansys modelling, a Free-Body-Diagram is created. Especially the fluctuation in the expected to be constant reaction force (static balancing) is target of investigation. Also this Free-Body-Diagram will help in finding the optimal placement of flexures in the suspension.

Defining inputs First of all the input forces/moments are determined. The input force on the ring gear and its suspension comes from the input torque on the central gear. For now we assume that this input torque is transferred at a single position, and that this force is tangential to the central gear. The input force that is being transferred to the ring gear at this single position can then be easily calculated from the input torque on the central gear, and its radius r (figure 5.24).

Note that in the real situation there is likely more than 1 contact point between the gears. Also the gears will try to push eachother away due to the pressure angle of the gear profile, thus the resulting force will not be in the tangential direction. These simplifications are made to approach the situation with a simple model.

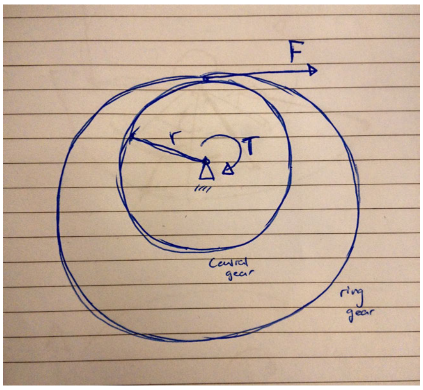

Figure 5.24: Input force as a result of torque on central gear. Note that in reality a force distribution is expected rather than a single contact point. For ease of implementation however this assumption is made.

The input torque that is working on the ring gear and its suspension can then be calculated as such:

$$F = \frac{T}{r}$$

Note that the direction of this force is constantly changing due to the change of contact point between the gears. This is the input we use to determine the forces in the system using the Free-Body-Diagram. This way we eliminate the system by removing the central gear, and only considering the ring gear and its suspension.

We want to easily compare this Free-Body-Diagram to the modelled situation in Ansys. In Ansys it was beneficial to place all the input forces on a single node, in our case the node at the centre of the ring gear. For this reason the single *input force* is changed in an *input force* + *input torque* depending on the radius of the ring gear (figure 5.25).

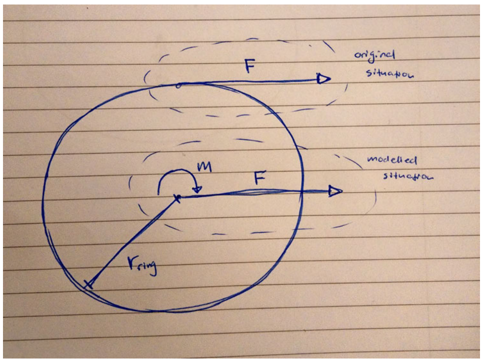

Figure 5.25: Input force and moment used for Free-Body-Diagram. Based on figure 5.24 these input loads are defined to represent transferred forces from the cycloidal rotor.

Free-Body-Diagram (FBD) With the inputs defined, we can create a Free-Body-Diagram (FBD). In the previously discussed Ansys model a serial flexure mechanism was modelled and mirrored. This model will only contain one side of the mirrored suspension (4 flexures instead of 8). Later we will see that this is actually a better scenario for static balancing reasons.

For all schematics in this chapter we assume a torque applied in clockwise direction. A model is made resembling the previously discussed Ansys model (figure 5.26).

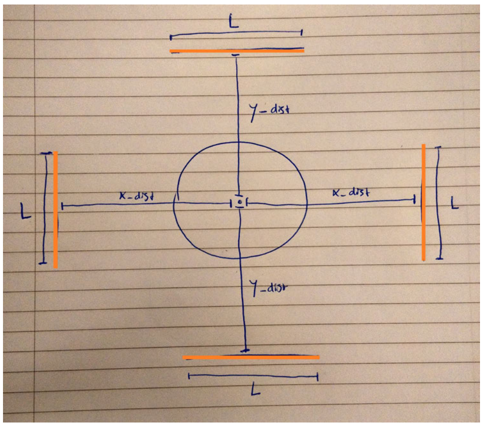

Figure 5.26: Dimensions used for FBD. The redundant parameters are removed from the model for simplification. Only the flexure length l,spacing s and the thickness t remain as parameters in the model.

Note that only the distance of the flexures from the center are taken into consideration. The reason for this is that the equilibrium in x- and y- direction do not depend on this parameter. This choice is supported by results from the Ansys model, which showed little change in the results when varying the parameters L_{off1} and L_{off2} (figure 5.17.

The small change observed is attributed to the position of the center of compliance of each of the translational stages [18]. When taking a value of half the flexure length for the parameters L_{off1} and L_{off2}, the flexures are placed symmetrically around the ring gear. As a result the input force F is located in the center of compliance of both the translational stages. As a result of this decision there will be no additional moment acting on the flexures induced by a moment arm on the translational stage.

Both this finding and the observations made in the Ansys model support the decision made to eliminate the L_{off1} and L_{off2} parameters from the FBD model, thus simplifying the model again. For two scenarios the Free-Body-Diagram is sketched in figure 5.27.

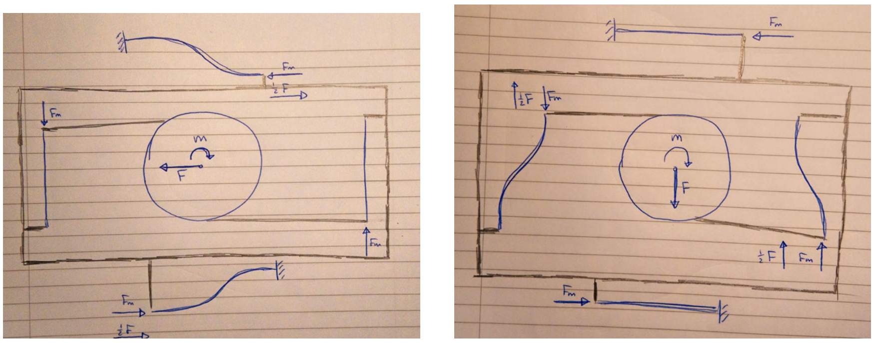

(a) First loading scenario for suspension. Maximal deflection of primary parallel flexural stage.

(b) Second loading scenario for suspension. Maximal deflection of secondary parallel flexural stage.

Figure 5.27: Schematic of Free-Body-Diagram for two key positions. Note that the direction of the applied force depends on the position of the compliant suspension, as the contact point between gears will shift during the motion.

As can be seen the reaction force F_m on the flexures as a result of applied moment is always directed in the same direction relative to the flexure. As a result all the flexures are loaded in tension, just as they were designed to. The magnitude of force F_m is dependent on the moment M and the leverage arm (distance to the flexure), x_{dist} and y_{dist} for respectively the vertical and horizontal flexures. The longer the leverage arm, the smaller this force will be.

Another interesting observation is made for the applied force F. The direction of the reaction force on the flexures as a result of applied force F does change direction. It will either work with force F_m, or against force F_m. As a result one side of the flexures will be loaded differently than the other side. This reaction force does not depend on the flexure distance, like we saw for the applied moment. As a result several different loading cases for the flexures can be obtained. Depending on the parameters of the model, either both flexures are loaded in tension, or one side is loaded in compression.

These forces are used to get an estimate on the resulting stiffness of the suspension in x- and y-direction. A model is used from the book 'Design principles for precision mechanisms' written by Herman Soemers (figure 5.28). This model includes both the stiffness of the flexure, and the effect of pre-stressing the flexure in the longitudinal direction. The model is applied on all separate flexures in the model to see the variation induced by non-symmetrical loading in the suspension.

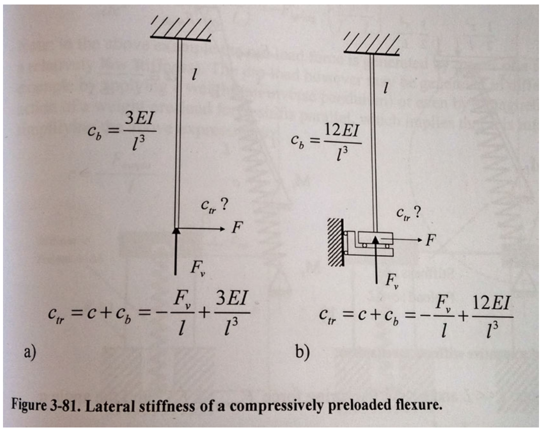

Figure 5.28: Image from 'Design principles for precision mechanisms': Calculation stiffness of flexure under compressive load.

Conclusion The model is implemented in Matlab to check on the actual numbers. As a result the following conclusions for the parameters of the model can be made:

- Parameters x_{dist} and y_{dist} should be equal to obtain a statically balanced system under loaded conditions
- For x_{dist} & y_{dist} equal to radius r_{ring}, the forces F_m and $\frac{1}{2}F$ counter eachother out. Meaning one side is unloaded, while the other side bears the full load.

The FBD model was also compared to the previously discussed Ansys model. The parameters of the model are identical in the FBD and the Ansys modelling. The parameters that are varied are the distance between respectively the horizontal and vertical flexures.

Interestingly the simple model implemented in Matlab manages to approximate the much more complicated model created in Ansys. Also the effect of parameters x_{dist} and y_{dist} becomes clear. The vertical and horizontal flexures should be spaced at equal distance to remove the observed torque ripple.

EXPLANATION TORQUE DEPENDENCY

The above Free-Body-Diagram does not explain the torque dependency of the stiffness of the suspension. The explanation for this torque dependent behaviour observed in both the Ansys simulation and the FBD model in Matlab lies in the loading case of each of the flexures. The flexures are displaced over a distance e, and at the same time loaded under tension by a (large) force from the input torque. Making a schematic drawing of a single flexure in the suspension reveals the problem (figure 5.30).

Each of the flexures are loaded in tension as a result of the applied moment. At the same time the flexures are deflected over a distance e. A force triangle can now be drawn and reveals that a component of this applied

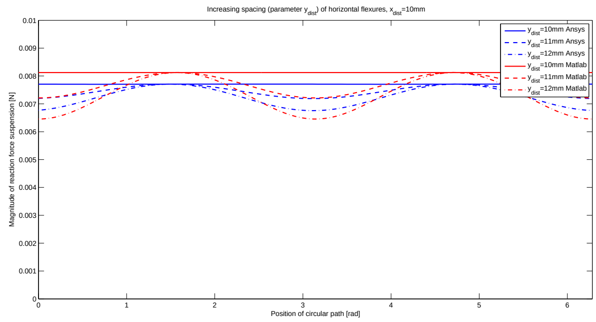

(a) Comparison FBD and Ansys for constant x_{dist}.

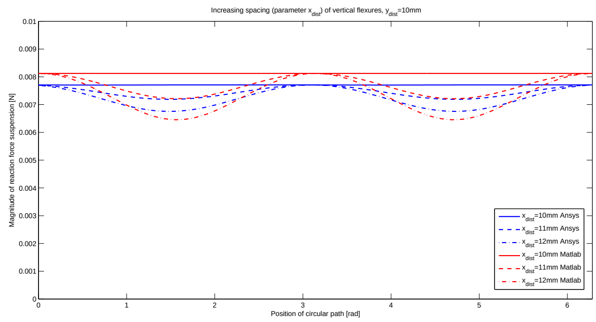

(b) Comparison FBD and Ansys for constant y_{dist}.

Figure 5.29: FBD model compared to Ansys. Using the FBD model the cause of the imbalanced suspension under loading conditions is determined. The spacing between the flexures, modelled as x_{dist} and y_{dist}, needs to be equal in order to have a statically balanced system when an input moment is applied.

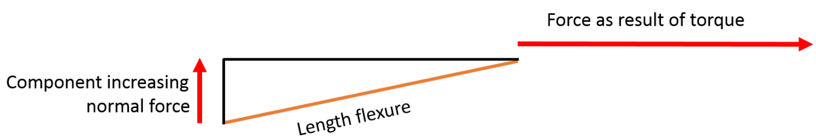

Figure 5.30: Explanation for torque dependency of suspension stiffness. Applied a (large) force on the flexure in deflected state will cause a sideways force. This sideways force will act as an increased stiffness of the suspension seen from the center of the suspension. The further the flexure is deflected, the larger this sideways force will be. Thus this stiffening effect is dependent on eccentricity e, as observed in figure 5.22.

force is directed towards the resting position of the flexures. In other words, it wants to move the suspension back to the center of its displacement (the central gear center). This component of the force stiffens the suspension, thus making the overall stiffness dependent on the input torque. The efficiency of the system is dependent on the contact force between the gears. A higher input torque will therefore result in a lower efficiency.

Since we have observed that there are scenarios possible where one side of the parallel flexures is unloaded, while the other side bears the full load, there are possibilities of overcoming this identified problem. If we can direct all the force to one side of the parallel flexures, and ensure that at that moment the flexure is in line with the applied force, the component sketched in figure 5.30 will be very small or equal to zero.

5.8. NEW ANSYS MODEL

A new Ansys model was created that removed the redundant parameters. This made the Ansys model much easier to implement. As observed the fluctuation in stiffness throughout the cycle was caused by an unequal spacing of the primary and secondary set of parallel flexures. From this we can conclude that the spacing s for both sets of parallel flexures should be equal. Also the flexures are placed symmetrically around the central axis to remove any effects of applying a force away from the center of compliance of the parallel flexures [18].

LOADING CASE

The previous Ansys model only incorporated the applied moment. From the FBD can be concluded that this loading case is not an accurate representation. Besides an applied moment, the suspension is also subjected to an additional force. In the previous model this force could not be applied since the displacement was imposed on the center of the suspension (center of annulus). The new Ansys model depicts a more accurate representation by not imposing this displacement at the center of the annulus, but by imposing the position of the output shuttle, which in the real situation will be locked by the rest of the compliant transmission. As a result the center of the annulus is left free to be subjected to both a moment and a force.

DUAL-LAYER

As a result of the symmetrical placement of the flexures around the ring gear, the suspension can only have a single intermediate stage with a translational motion. Since this will be the output stage for the reciprocating transmission, this is the part that will lock the compliant ring transmission. Only a single translational direction can be locked in a single layer. Since we need to constrain both translations in order to keep the ring gear in place, another layer is required to constrain the other translational motion. We cannot constrain this second translation on the ring gear itself because the ring gear translates in two directions simultaneously.

Therefore the same suspension is required in an additional plane, only this time rotated by 90 degrees to be able to lock the other translational direction.

NEW MODEL

Since the flexural members are orientated symmetrical around the central axis, the model can be build up using polar coordinates, figure 5.31. The model is then only depending on the length l and spacing s of the flexural components. The model uses the same material parameters for Silicon as in the previous model, as well as the same element types to represent the flexural members and rigid connections.

The rigid annulus is represented by red lines, the (single) intermediate body is depicted in blue in figure 5.31. The flexural members are depicted by black lines. All lines are glued together to model the monolithic suspension. All DOFs are fixed at the grounding points, keypoints 5 and 9. Note that although a blue line crosses keypoint 1, they are not connected in the model. The only connection between the intermediate stage and the annulus is via the horizontal flexures, figure 5.31.

Like in the FBD model, the loads will be applied at the center of the annulus, in the model represented by keypoint 1, figure 5.31. Here the moment as a result of the barrel spring will be applied on the center of the annulus, keypoint 1 in figure 5.32, as well as the force as a result of the gear contact. This resulting force is again the derived by dividing the moment M on the barrel spring by the radius of the cycloidal rotor r, like in the FBD model (see section 5.7). Of course the direction of this applied force changes with the location of the gear contact, and hence the position of the suspension.

$$F = \frac{M}{r}$$

The motion of the suspension is imposed by a displacement on the intermediate shuttle, at the position where the rest of the suspension will be connected, keypoint 10 in figure 5.31. This position is chosen such that forces acting on the suspension go through the center of compliance of the parallel suspension. The displacement (position of suspension) and applied force are related. In the real situation the translating shuttles will be the positions locked by the remainder of the transmission.

The entire model is doubled and rotated 90 degrees to create the second layer. The central points on the annulus are fused together. An offset is introduced between the two layers to prevent interference. The resulting model is shown in figure 5.32

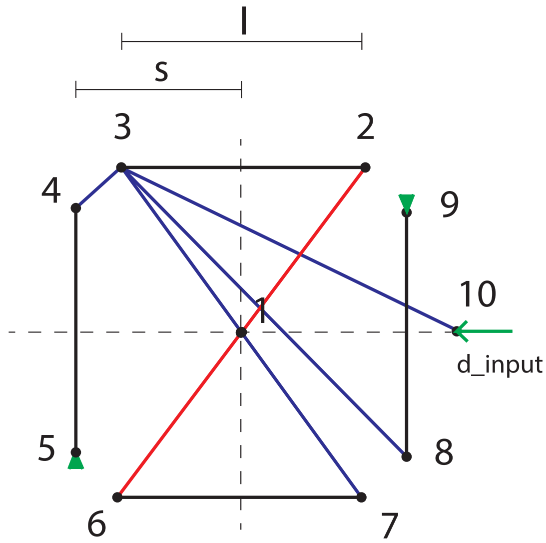

Figure 5.31: New Ansys model parameters. Only the length l, spacing s and thickness t of the flexural members remain. This reduction is based on the findings in the previous sections, where the effect of these parameters is studied.

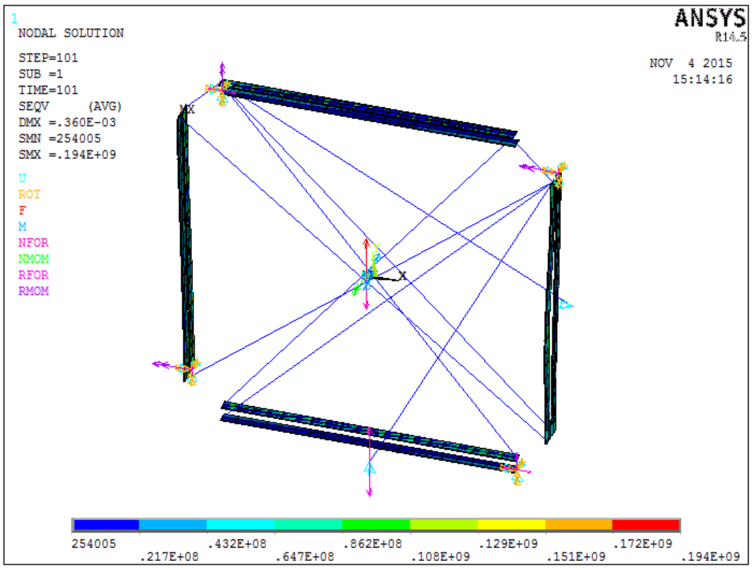

Figure 5.32: New Ansys model including simulated reaction forces/moments.

6

EXPERIMENTS

Experiments are designed to validate the results from the simulations. Two measurement protocols are designed as such. One is aiming at verifying the force-deflection behaviour predicted by the Ansys simulations (FDT). The other is aiming at incorporating the gear profile and estimating the efficiency of the system by measuring the frictional losses (FDR). The abbreviations represent the type of measurement; FD stand for Force-Deflection. Both of the measurements require a Force-Deflection setup. The T and R in the abbreviations stand for the type of input motion, translational or rotational.

These measurement protocols are made for a preliminary design, because of a delay caused by the fabrication technique. The micro design is fabricated in Silicon using a process called photolithography. For this process a mask has to be made with the pattern that we want edged in the silicon wafer. This however does not change the way to validate the simulation results. Note that this design is not optimized for the torsional load that will be applied. The code $TR01E1Si$ is a reference to the name given to the design.

6.1. FORCE-DEFLECTION MEASUREMENT

Measurement Protocol

TR01E1Si_FDT

(30um beams)

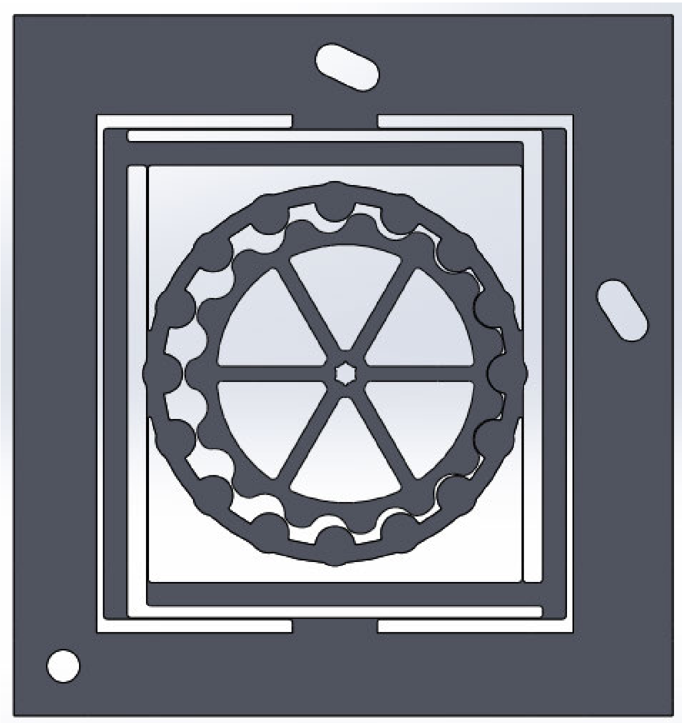

Introduction

This initial reciprocator design is aiming at verifying simulations for the efficiency of the system. The first aspect is to verify that the stiffness of the suspension is identical in all radial directions, thus resulting in a system without any rotational stiffness. The second aspect is to verify the frictional loss of the system. This measurement protocol is only aiming at the first aspect; the stiffness of the suspension. The central gear is therefore not included for this measurement. Only the ring gear and suspension are required.

The ring gear is moving over a circular path as a result of the geometry of the two gears. When traveling over this circular path, we would like to see the energy in the suspension to be constant. As a result the rotational stiffness felt by the input gear will be equal to zero (not taking frictional losses into account). The way to achieve this is to have a suspension that is statically balanced (constant energy) over its entire circular path.

This measurement is aiming at verifying that the suspension is statically balanced when moving over a circular path. This is verified by mapping the x-y stiffness profile. This is done by performing translational force-deflection measurements in radial direction. After each measurement the ring is rotated 360/16 degrees (16 = number of ‘rollers’ on the ring) and the force-deflection measurement is repeated.

An important aspect for this measurement are **centering of the ring gear**, such that a rotational stage can be used to re-orientate the ring radially. The other important aspect is that the **positioning of the tip with respect to the ring** shape is identical for each test run. The specified rotational angle of 360/16 degrees should ensure this.

Test1: Force-deflection.

Setup	Force deflection measurement in radial directions.
Goal	To verify the x-y stiffness profile of the suspension
Input data	Translational displacement
Output data	Force as a function of displacement (.xls or .txt preferred).
Target devices	1
Minimal length of measurement	300 μm
Minimal sample rate	~
Repetitions per device	~
Test steps	1. Center the ring gear using a high speed camera and tracking the translational motion when the rotational stage is activated. If there is translational motion the ring is not properly centered. 2. Position the tip of the force deflection setup on the highest part of (one of the 16) circular rings. 3. Perform force deflection measurement over a range of 300 μm. 4. Rotate the entire device over an angle of 360/16 degrees and repeat steps 2 and 3 until all radial directions are covered.
Additional Notes:	Try to get the tip as close as possible to the surface before each test run. Post-processing of the results will take care of any errors of tip positioning.

EXPERIMENTAL SETUP

The aforementioned measurement protocol is carried out on the Force-Deflection setup at Flexous. A mount was 3D-printed for the silicon device to be mounted on the test setup. The mount was designed to fit on a precision rotational stage. The measurement probe was fitted on a manual translational stage, which in turn was fitted on a linear actuator. This way the force could be applied in all possible directions and positions in the plane.

The device was rotated between each measurement run over an angle of 360/16 degrees as described in the protocol. Instead of centering the gear on the rotational stage as is decribed in the measurement protocol the decision was made to manually position in x- and y- direction before every test. This was done because only 5 measurements are needed, thus manually repositioning would take less time than carefully centering the prototype. After each rotation of the device the translational position of the probe was manually adjusted.

Also the maximum displacement imposed on the suspension was lowered to ensure the device would survive the test. Instead of a displacement of 300 μm what it was designed for, the maximal displacement used in the experiment was 200 μm. This smaller displacement is more than enough to find the slope in the measured data, and thus the stiffness of the suspension.

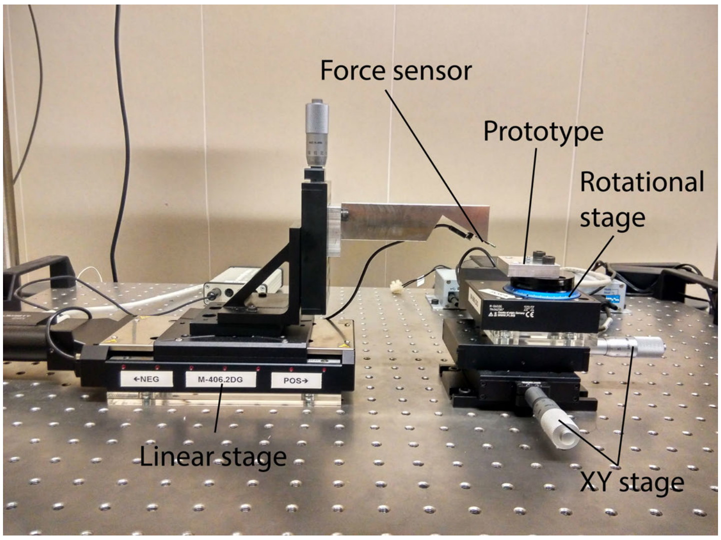

Figure 6.1: Picture of force-deflection setup indicating the components. The prototype is manually positioned using the XY stage and rotated with respect to the force sensor for each measurement direction using a precision rotational stage. Each measurement (5 directions) was done 5 times, resulting in a total of 25 force-deflection datasets.

SPECIFICATIONS FORCE SENSOR

Table 6.1 shows the specifications of the force sensor used for the force-deflection measurement.

RESULTS

The raw data is plotted in figure 6.2. Some start-up behaviour for each measurement run is observed. This is caused by the probe not touching the device in a small range of its displacement. The probe registers no force on its probe and this translates to a noisy signal around the 0-value. This data will be removed when processing of the data.

By calculating the Pearson coefficient for each data run we can check the linearity of the data. The Pearsson coefficient is calculated on the cropped data where the non-zero terms are already removed. The Pearson coefficients between the output force and the input motion for every run are shown in table 6.2. From these numbers we can conclude that the measured stiffness is linear.

The next step is to analyse the slopes of the lines to compare the stiffness of the device in the 5 directions. For this a linear regression model was fitted on the cropped data. The results of this fitting are plotted separately

Table 6.1: Specifications of force sensor (FT-S10000) as specified by the manufacturer.

Sensor force range	$\pm 10000\mu$N
Sensor gain	5000μN/V
Output Signal	$0-5$V
Output voltage at zero load	2.25V
Power supply voltage	5V
Resolution at 1000Hz	5μN
Resolution at 10Hz	0.5μN

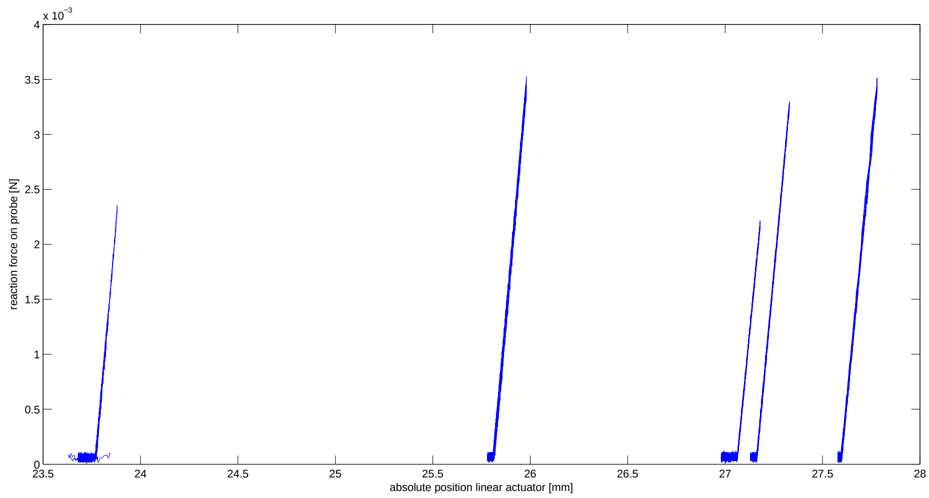

Figure 6.2: Raw data from the measurement for each of the 5 directions. Note that the 5 force-deflection datasets per measurement direction are overlapping.

for each of the 5 measurements in figure 6.3. The slopes of the linear regression model of the different measurements can then be compared to check if the stiffness of the suspension is identical in all directions, and compared to the expected stiffness from the finite element modelling, and linear beam theory.

Note that the absolute displacement in the data plots are the result of repositioning of the sensor. The Force-Deflection plot should pass through the origin. For comparing the measured data with results from the Ansys simulation a correction will be applied to align the data points with the origin. This correction will be based on the calculated linear regression model.

CONCLUSION

Ansys modelling indicates a system with a nearly identical stiffness in all 5 directions. As can be observed from the slopes of the linear regression model the stiffness is not identical in all directions. Instead a variation between the highest and lowest stiffness of $(0.02318 - 0.02091)/0.02318 = 9.78\%$ is observed.

Table 6.2: Pearsson coefficients for each of the 5 measurement directions.

	Pearsson coefficient
measurement 1	0.9974
measurement 2	0.9981
measurement 3	0.9995
measurement 4	0.9995
measurement 5	0.9993

Table 6.3: Slopes of force-deflection data based on a linear regression model. The same model is used to calculate the Pearsson coefficients in table 6.2

	Slope linear regression model [N/mm]
measurement 1	0.02318
measurement 2	0.02307
measurement 3	0.02211
measurement 4	0.02135
measurement 5	0.02091

DISCUSSION

Having a closer look at the design drawings reveals a small hint on why the stiffness is not constant. The fillets applied to the design result in slightly shorter flexures (figure 6.4). As a result the vertical flexures are slightly longer than the horizontal flexures. We would expect therefore that the stiffness in x-direction (horizontal) is lower than the stiffness in y-direction (vertical), something we observed in the measured data.

The stiffness of the beams in the linear regime can be calculated based on linear beam theory. The loading case can be estimated as a beam that is fixed on one end, and has only its rotation constrained on the other end (figure 6.5. Since no rotation on either end is permitted by the design of the beam is connected to rollers on the right side. Note that horizontal displacement is still possible (figure 6.5(b)).

From this case the stiffness k can be calculated as follows:

$$
\begin{aligned}
k = \frac{F}{\delta y} &= \frac{12EI}{L^3} \\
&= E\left(\frac{wt^3}{L^3}\right)
\end{aligned}
$$

Where w stands for the width of the beam and t represents the thickness of the beam. Note that here a rectangular cross-section of the beam is assumed. From this equation for the stiffness of the beam the difference in stiffness can be calculated as a result of the observed difference in beam length. Lets name the stiffness of the beams with a length of 4.83 mm k_{low}, and the stiffness of the beams with a length of 4.78 mm k_{high}. After all the beam with a higher length will have a lower stiffness and the the other way around. Then the expected difference in stiffness can be calculated as follows:

From this case the stiffness k can be calculated as follows:

$$
k_{difference} = \frac{k_{high} - k_{low}}{k_{high}} = 3.07\%
$$

It can be concluded that the difference in length alone cannot explain the observed stiffness. However looking at the equation for the theoretical stiffness , we see that the stiffness is very sensitive to the thickness of the flexural beams as well. A small difference in thickness as a result of an uneven etching process in x- and y-direction can result in a discrepancy in the stiffness as observed. Such small difference are not visible with the SEM, which relies on visual inspection with an approximated precision of $\pm 1.5\mu$m.

6.2. NO-LOAD TORQUE MEASUREMENT

Some alterations were made to the original protocol to get more out of the measured data. To get an idea of the sensitivity of the positioning errors, various translational misalignments were introduced to the positioning of the annulus with respect to the cycloidal rotor. This way the suspension will be displaced more in one direction than the other, resulting in an unbalanced system. This affects the normal force between the gears, and thus the frictional loss of the system. Both the original protocol and the altered protocol are presented.

Measurement Protocol

TR01E1Si_FDR

(30um beams)

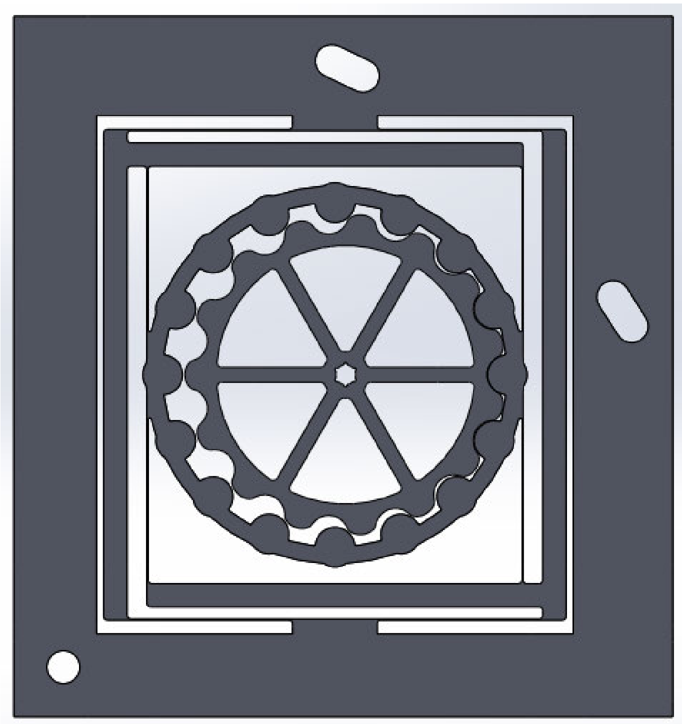

Figure 1 TR01E1Si

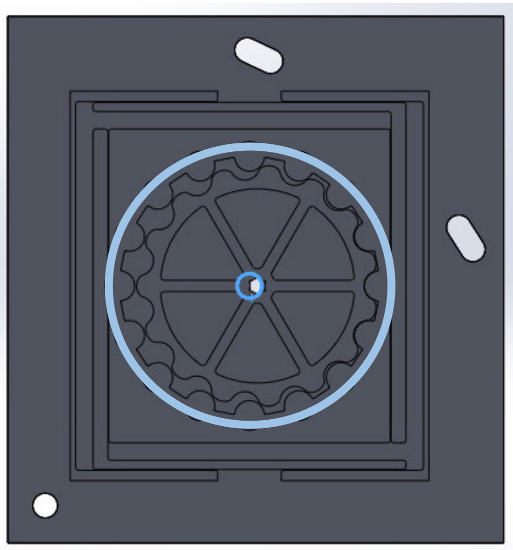

Figure 2 – location for bearing for input gear

Introduction

This initial reciprocator design is aiming at verifying simulations for the efficiency of the system. The first aspect is to verify that the stiffness of the suspension is identical in all radial directions, thus resulting in a system without any rotational stiffness. The second aspect is to estimate the frictional loss of the system. This measurement protocol is only aiming at the second aspect; the frictional loss between the two gear contacts. The frictional loss can be estimated by performing a torque measurement on the central gear.

This frictional loss is dependent on the normal force and the friction coefficient. The normal force is the result of the reaction force of the suspension on the ring gear. For this reaction force to be identical in all radial directions it is important that the central gear is positioned properly! For the correct positioning see the picture on the right (this is the position where bearings are placed for the input shaft). When the input gear is aligned, the suspension should exert a reaction force equal in all radial positions, as will be verified in another experiment.

The aim of this experiment is to find the torque needed to drive the system, and hence get an estimation on the efficiency of the system. This experiment assumes no work being done by the system. The measurement is done using a torque-speed setup. The torque will be measured using a rheometer at the end of a gear transmission with a ratio of 720. The experiment will be performed at low speed to find the losses due to friction only (no dynamics).

Key aspects for this experiment are the positioning of the input gear, as the static balancing principle relies on this positioning. The input gear should be positioned **concentric** with the ring gear when its suspension is in **un-deflected position**. An assembly was uploaded in BOX with the design including the mounting position for the central gear

Note: This setup does not include the input torque (≈9mNm). This experiment will solely aim at the frictional losses as a result of the system without external forces/torques.

Test1: Force-deflection.

Setup	Rheometer (Torque-Speed).
Goal	To determine the torque required to drive the system.
Input data	Angular velocity
Output data	Torque as a function of angular displacement (.xls or .txt preferred).
Target devices	1
Minimal length of measurement	90 degrees
Minimal sample rate	~
Repetitions per device	~
Test steps	1. Center the ring gear with respect to the suspension (see mounting assembly). 2. Connect the two correctly positioned parts by positioning ring gear over the central gear. 3. Apply a low angular velocity on the rheometer (low speed at reciprocator as well). 4. Use camera to capture the positioning of both gears and movement of suspension. 5. Compare results with and without the ring gear (+suspension) connected to the central gear.

Measurements on the reciprocator

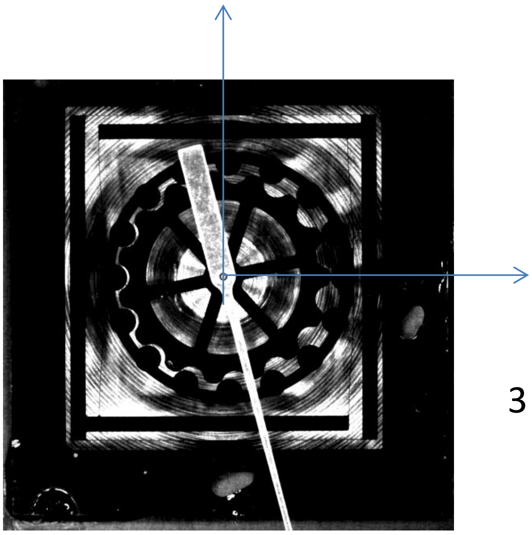

9 positions:

- center of the wheel aligned with center of the outer ring: up0r0
- center of the outer ring displaced of X up and Y right with respect to the center of the wheel. File: upXrY

3 experiments carried out for each position:

- 0.0157 rad/s for 400 s (i.e. 1 full rotation in 400 s) : peak1
- 0.0628 rad/s for 100 s (i.e. 1 full rotation in 100 s) : peak2
- 0.628 rad/s for 100s (i.e. 10 full rotations in 100 s) : peak3

Table 6.4: Specifications of the torque sensor (AR-G2), as provided by the manufacturer TA Instruments.

Minimum Torque Oscillation CR	0.003μNm
Minimum Torque Oscillation CS	0.003μNm
Minimum Torque Steady CR	0.01μNm
Torque Range Steady Shear CS	0.01μNm
Maximum Torque	200mNm
Torque Resolution	0.1nNm
Motor Inertia	18μNms
Angular Velocity Range CS	0 to 300 rad/s
Angular Velocity Range CS	1.4$E-9$ to 300 rad/s
Frequency Range	7.5$E-7$ to 628 rad/s
Displacement Resolution	25nrad
Step change in velocity	7ms
Step change in straint	30ms
Direct Strain Control	Standard
Thrust Bearing	Magnetic Bearing
Normal/Axial Force Range	0.005 to 50 N
Smart Swap{TM}	Standard
Smart Swap Geometry	Standard
Peltier Plate	-40 to 200°C
Environmental Test Chamter	−160 to 600°C
ETC Camera Viewer	Optional
Concentric Cylinder	−20 to 150°C
Circulator Control	Peltier Control
Upper Heated Plate	−30 to 150°C

EXPERIMENTAL SETUP

The experimental setup consists of two separate XY-stages (Newport M-406). One XY-stage is used to position the annulus (and suspension) relative to the cycloidal rotor. The other XY-stage is used to position the entire setup (suspension and annulus, cycloidal rotor and aforementioned XY-stage) with respect to the torque sensor (TA Instruments AR-G2). The procedure for aligning the annulus with the cycloidal is done using a microscope. The annulus and cycloidal rotor are roughly aligned concentric with the suspension in undeflected position. After mounting the annulus (cycloidal rotor and annulus in same place) the alignment is checked using the microscope. The horizontal flexures should be placed at same spacing from the center of the cycloidal rotor, and the same holds for the vertical flexures. This distance is checked using the microscope and adjusted accordingly. The procedure is estimated to have a precision of ±0.5μm. From this position the adjustments are made to perform the sensitivity measurements.

SPECIFICATIONS TORQUE SENSOR

Table 6.4 shows the specifications of the force sensor used for the no-load driving torque test.

RESULTS

The results from the torque measurement are shown in figure 6.7. The measured data is in the same order of magnitude as the simulations. The differences can be explained by the wide range for the friction coefficient μ for silicon, and the possible losses in the gear train being used in the setup. The difference in amplitude can be attributed to a play in the bearings suspending the axis of the cycloidal rotor. This play is reducing the effective displacement of the suspension, resulting in a lower reaction force from the suspension, lowering the overall fluctuation in the normal force, and thus the fluctuations in the observed moment.

SENSITIVITY

The annulus (and its suspension) are positioned with respect to the central axis of the cycloidal profile. As mentioned in the alterations in the protocol, a sensitivity was performed. The in-plane alignment was changed compared to the 'optimal' alignment, which is done using a microscope and manual positioning. The in-plane misalignment results in one side of the suspension being deflected more than the other, resulting in an asymmetric loading of the gears. This will affect the frictional force, and thus the measured moment. The sensitivity of the positioning error was measured for different misalignment distances, as shown in figures 6.8 and 6.9.

CONCLUSION

The frictional loss as a result of the stiffness pushing the annulus on the cycloidal rotor is constant, apart from the fluctuation for each gear tooth. The energy loss due to the stiffness is marginal compared to the energy throughput of the system, in case of an input moment of 9Nmm. The magnitude and trend of the measured moment was predicted by the modelling.

From the sensitivity plots, see figures 6.8 and 6.9, it is clear that the misalignment results in different moments being measured on different positions in the rotational cycle. The case where no misalignment was introduced, figure 6.7(a), the measured was constant (apart from the fluctuations per toot) over the entire cycle. An indication that the suspension indeed is statically balanced, as it was designed. Also this observation indicates that the positioning of the system was done precisely enough. A similar positioning procedure in a real mechanical watch case would result in a constant energy loss in of this system.

The sensitivity measurements shows a fluctuating energy loss depending on the position of the mechanism, as was expected. A higher contact force between the cycloidal rotor and the annulus will result in an increased frictional loss. The energy loss is still marginal compared to the power throughput of the system. However fluctuating energy loss effect is expected to be amplified when a load is applied to the system, since the stiffening effect is dependent on the displacement (eccentricity) of the suspension, see section 5.7.

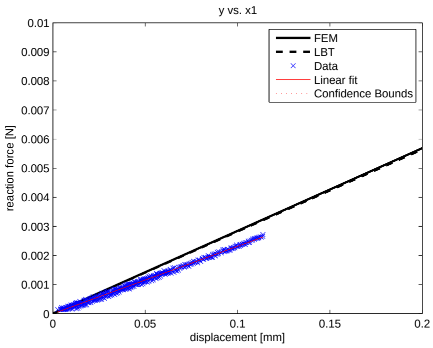

(a) Measurement 1 compared to FEM and LBT

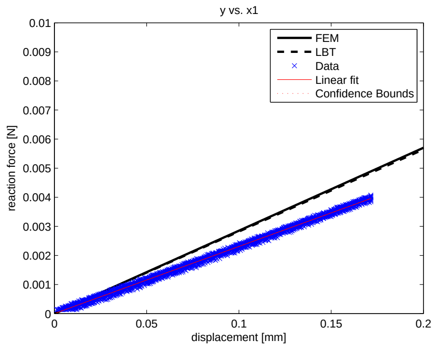

(b) Measurement 2 compared to FEM and LBT

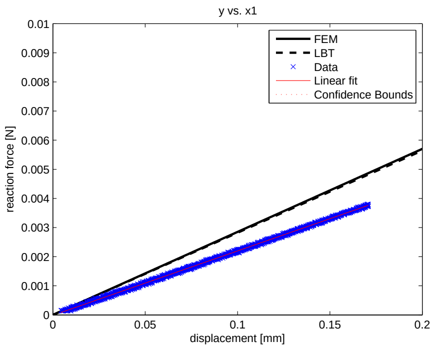

(c) measurement 3 compared to FEM and LBT

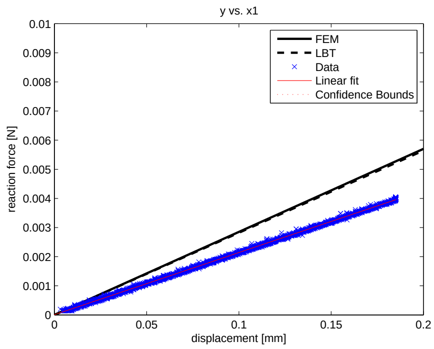

(d) Measurement 4 compared to FEM and LBT

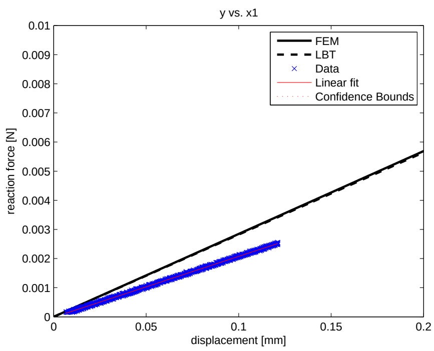

(e) Measurement 5 compared to FEM and LBT

Figure 6.3: Measurement data compared to Ansys modelling (FEM) and linear beam theory (LBT). The simulations are done for a rectangular beam thickness t of 21.5μm, resulting from the SEM imaging. Note that simulations for a thickness t of 20μm show a better fit, which can be attributed to an inaccuracy of $\pm$1.5μm for the SEM imaging.

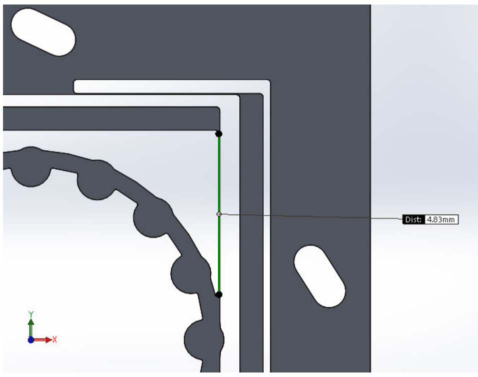

(a) Length flexures closest to ring gear (secondary stage).

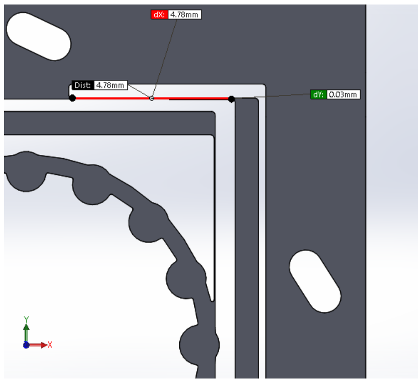

(b) length flexures closest to base (primary stage).

Figure 6.4: Difference in length between horizontal and vertical flexures observed after rechecking the CAD files. The difference can explain 3% stiffness deviation.

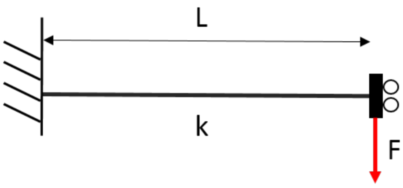

(a) Simplified model for flexure load case.

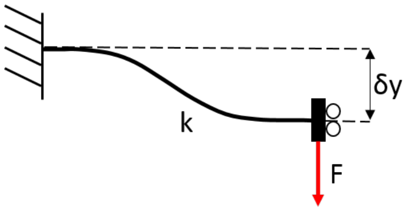

(b) Beam deformation under loading.

Figure 6.5: Linear beam theory loading case for stiffness calculation.

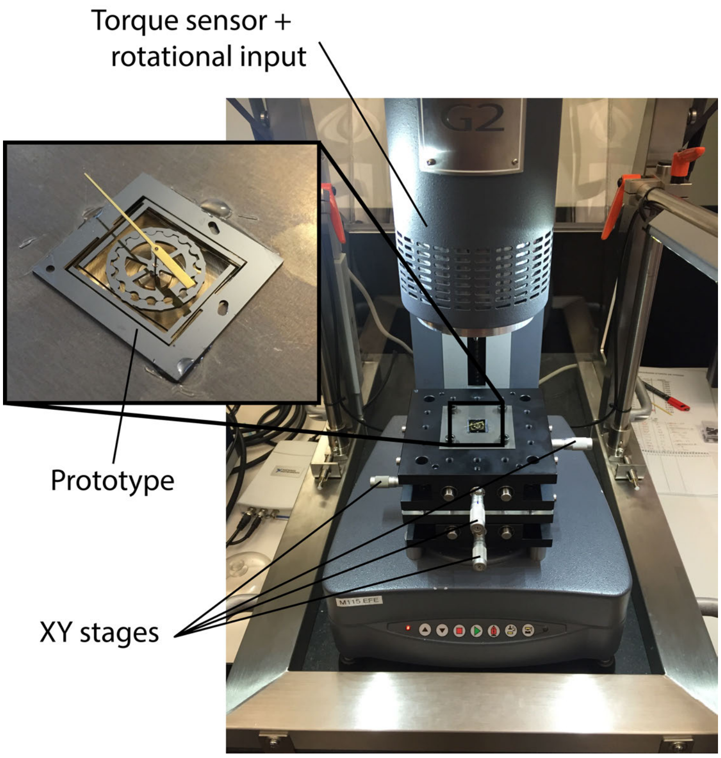

Figure 6.6: Picture of the setup used to measure the torque. An input rotational velocity is applied on the cycloidal rotor, and the resisting torque is measured using a torque sensor (TA Instruments AR-G2).

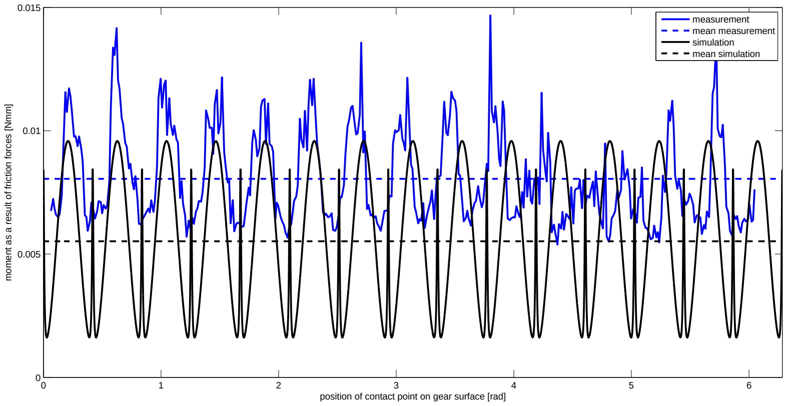

(a) Torque measurement and simulation for a single full rotation of the cycloidal rotor.

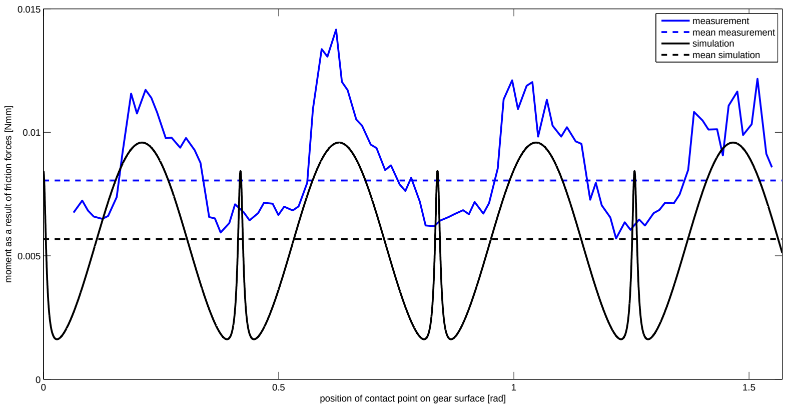

(b) Torque measurement and simulation for a quarter rotation of the cycloidal rotor.

Figure 6.7: Torque data compared to simulated torque. A friction coefficient of $\mu = 0.3$ is taken for the simulation, with an displacement for the suspension of 295μm.

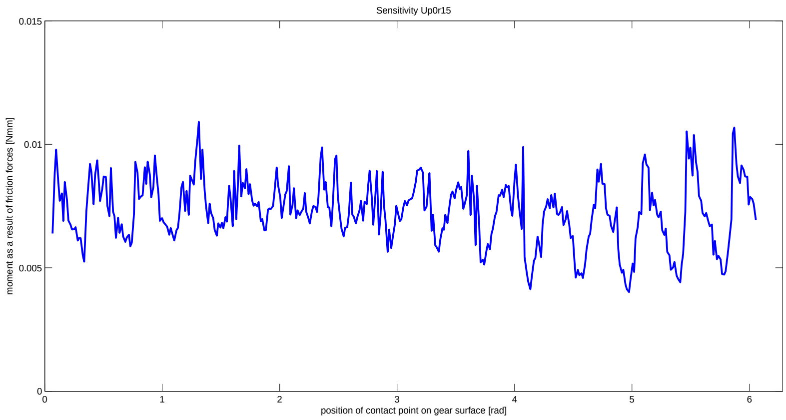

(a) Positioning error 15μm x-direction (toward the right)

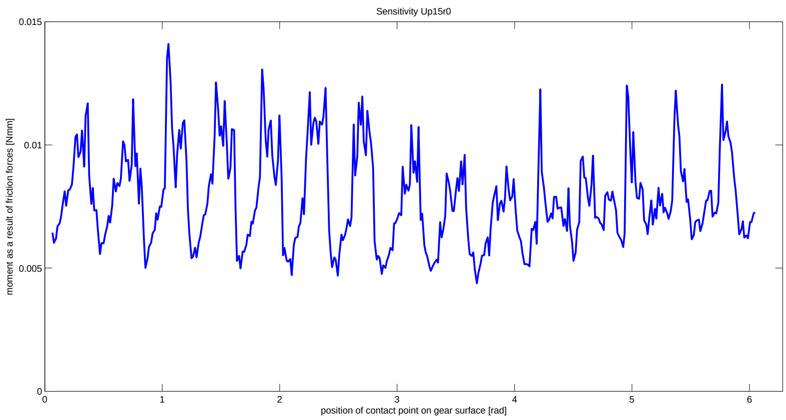

(b) Positioning error 15μm y-direction (upwards)

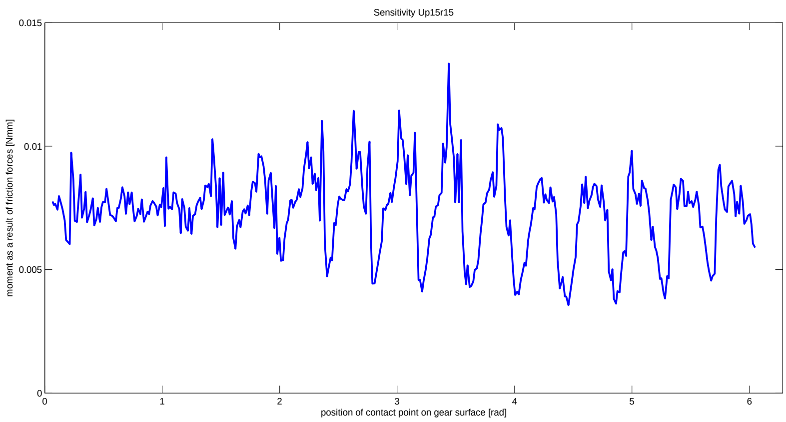

(c) Positioning error 15μm in both x- and y-direction (right and upwards)

Figure 6.8: Sensitivity for positioning error of gear alignment. The in-plane alignment is varied with 15μm in x- and y-direction

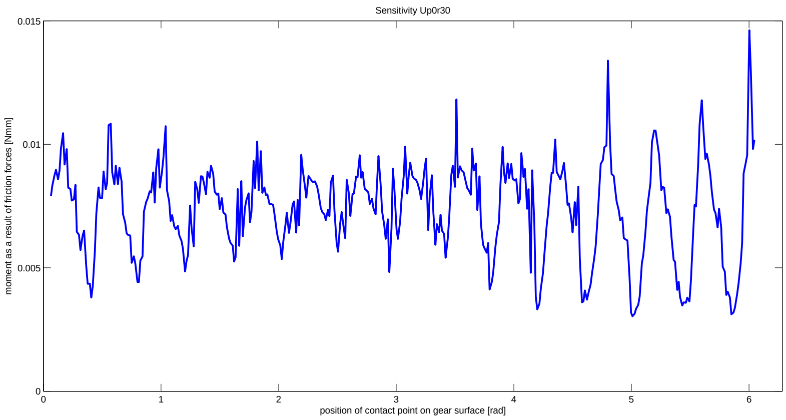

(a) Positioning error 30μm x-direction (toward the right)

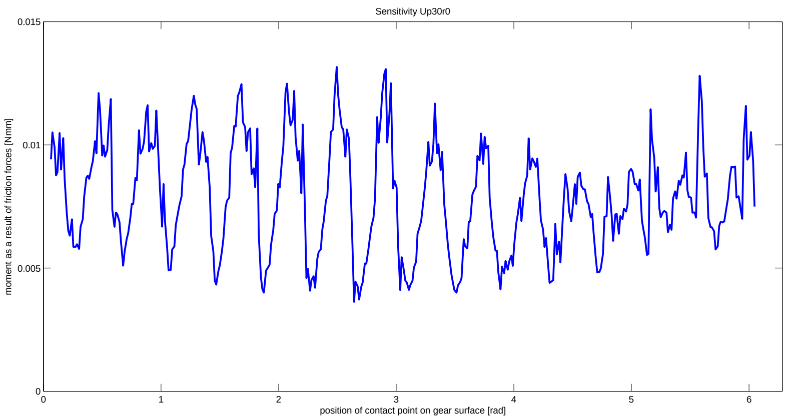

(b) Positioning error 30μm y-direction (upwards)

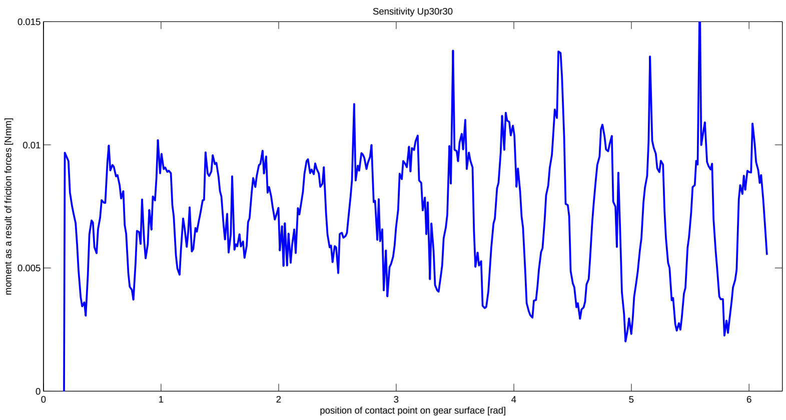

(c) Positioning error 30μm in both x- and y-direction (right and upwards)

Figure 6.9: Sensitivity for positioning error of gear alignment. The in-plane alignment is varied with 30μm in x- and y-direction

BIBLIOGRAPHY

[1] R. Du and L. Xie, *The Mechanics of Mechanical Watches and Clocks* (Springer, 2013).

[2] Q. H. Chen, D. M. Sun, D. H. Zhao, G. R. Kang, and J. Sun, *Kinematics analysis of morse cvt input mechanism,* Applied Mechanics and Materials **477**, 384 (2014).

[3] K. Ahn, S. Cho, and S. W. Cha, *Optimal operation of the power-split hybrid electric vehicle powertrain,* Proceedings of the Institution of Mechanical Engineers, Part D: Journal of Automobile Engineering **222**, 789 (2008).

[4] X. Li, W. He, L. Li, and L. C. Schmidt, *A new cycloid drive with high-load capacity and high efficiency,* Journal of Mechanical Design **126**, 683 (2004), 10.1115/1.1758254.

[5] C. Zhang, Y. Song, and J. Zhang, *Review of researches on ring-plate gear reducers with small tooth number difference,* in *12th IFToMM World Congress, France.*

[6] N. Ciblak and H. Lipkin, *Remote center of compliance reconsidered,* in *Proceedings of The 1996 ASME Design Engineering Technical Conference and Computers in Engineering Conference, Irvine*, pp. 1–10.

[7] G. Zong, X. Pei, J. Yu, and S. Bi, *Classification and type synthesis of 1-dof remote center of motion mechanisms,* Mechanism and Machine Theory **43**, 1585 (2008).

[8] D. P. Arnold and N. Wang, *Permanent magnets for mems,* Microelectromechanical Systems, Journal of **18**, 1255 (2009).

[9] M. A. Pucheta, N. E. Ulrich, and A. Cardona, *Automated sketching of non-fractionated kinematic chains,* Mechanism and Machine Theory **68**, 67 (2013).

[10] J. B. Hopkins and M. L. Culpepper, *Synthesis of multi–degree of freedom flexure system concepts via freedom and constraint topologies (fact),* Precision Engineering **not publish yet** (2007).

[11] J. B. Hopkins and M. L. Culpepper, *Synthesis of precision serial flexure systems using freedom and constraint topologies (fact),* Precision Engineering **35**, 638 (2011).

[12] F. Guan, C. Zhou, and Q. Huang, *An innovative planetary gear reducer with overcoming the" dead point",* Open Mechanical Engineering Journal **7** (2013).

[13] J. W. Sensinger and J. H. Lipsey, *Cycloid vs. harmonic drives for use in high ratio, single stage robotic transmissions,* in *Robotics and Automation (ICRA), 2012 IEEE International Conference on* (IEEE) pp. 4130–4135.

[14] T. Mackic, M. Blagojevic, Z. Babic, and N. Kostic, *Influence of design parameters on cyclo drive efficiency,* Journal of the Balkan Tribological Association Vol **19**, 497 (2013).

[15] B. A. Salamon and A. Midha, *An introduction to mechanical advantage in compliant mechanisms,* Journal of Mechanical Design **120**, 311 (1998).

[16] J.-H. Shin and S.-M. Kwon, *On the lobe profile design in a cycloid reducer using instant velocity center,* Mechanism and Machine Theory **41**, 596 (2006).

[17] Y.-W. Hwang and C.-F. Hsieh, *Determination of surface singularities of a cycloidal gear drive with inner meshing,* Mathematical and Computer Modelling **45**, 340 (2007).

[18] N. Ciblak and H. Lipkin, *Design and analysis of remote center of compliance structures,* Journal of Robotic Systems **20**, 415 (2003).

A

Ansys APDL code for Silicon prototype

```
FINISH
/CLEAR
/OUTPUT


pi = 3.14159265359

!!!!!!!!!!!!!!!!!!!!!!!!!!!!!!!!!!!!!!!!!!!!!!!!!!!!!!!!!!!!!!!!!!!!!!!!!!!!!!!!

l = 5e-3
d0 = 1.3e-3
d1 = 11.35e-3
d2 = 0.6e-3
d3 = 1.1e-3
d4 = 13.7e-3!2*d0 + 2*l + d3
d5 = 0!0.5e-3

!l = 5e-3
!d0 = 1.3e-3
!d2 = 0.6e-3
!d3 = 1.1e-3
!d4 = 13.7e-3!2*d0 + 2*l + d3
!d5 = 0!0.5e-3
!d1 = d3+d4

!!!!!!!!!!!!!!!!!!!!!!!!!!!!!!!!!!!!!!!!!!!!!!!!!!!!!!!!!!!!!!!!!!!!!!!!!!!!!!!!

eccentricity = 300e-6

input_M = -9e-3!-0.1950 ! [Nm] input moment as result of barrel spring torque


sensx = 0!30e-6 ! sensitivity x-direction
sensy = 0!sqrt(2)*5e-6 ! sensitivity y-direction

!!!!!!!!!!!!!!!!!!!!!!!!!!!!!!!!!!!!!!!!!!!!!!!!!!!!!!!!!!!!!!!!!!!!!!!!!!!!!!!!
```

```
n_elements = 20
substeps = 10

/PREP7
ET,1,BEAM188
ET,2,MPC184
KEYOPT,2,1,1

/ESHAPE,1

SECTYPE,1,beam,RECT
SECOFFSET,CENT,,,
SECDATA ,30e-6, 525e-6

!SECTYPE,1,beam,MESH,MEMS
!SECOFFSET,CENT,,,
!SECREAD,'APDL_MemsSect','SECT','C:\Users\Jan\Desktop\Thesis\Prototypes
\1-1_scale_May2015',MESH

MPTEMP,,,,,,,,
MPTEMP,1,0
MPDATA,EX,1,,169e9
MPDATA,EY,1,,169e9
MPDATA,EZ,1,,130e9
MPDATA,PRXY,1,,0.064
MPDATA,PRYZ,1,,0.36
MPDATA,PRXZ,1,,0.28
MPDATA,GXY,1,,50.9e9
MPDATA,GYZ,1,,79.6e9
MPDATA,GXZ,1,,79.6e9
MP,DENS,1,2330
MP,Mu,1,0.14

!!!!!!!!!!!!!!!!!!!!!!!!!!!!!!!!!!!!!!!!!!!!!!!!!!!!!!!
!!!!!!!!!!!!!! suspension !!!!!!!!!!!!!!!
!!!!!!!!!!!!!!!!!!!!!!!!!!!!!!!!!!!!!!!!!!!!!!!!!!!!!!!
Kp_n = 10
*DO,I,0,1
               CSYS,0
               CLOCAL, 11+I, 0, -Folded_Offset_Radius*cos(i*180/180*pi), -
               Folded_Offset_Radius*sin(i*180/180*pi), 0, 180*I

               K,1+I*Kp_n,0-d5,0
               K,2+I*Kp_n,d1/2-d5,d0
               K,3+I*Kp_n,d1/2-d5,d0+l
               K,4+I*Kp_n,-d1/2-d5,d0
               K,5+I*Kp_n,-d1/2-d5,d0+l

               K,6+I*Kp_n,-d1/2-d2-d5,d0+l
               K,7+I*Kp_n,-d1/2-d2-d5,d0+l+d3
               K,8+I*Kp_n,-d1/2-d2+l-d5,d0+l+d3
               K,9+I*Kp_n,-d1/2-d2-d5,d0+l-d4
               K,10+I*Kp_n,-d1/2-d2+l-d5,d0+l-d4

               *GET,Line_ID1,LINE,0,NUM,MAXD
               L,2+I*Kp_n,3+I*Kp_n
```

```
               L,4+I*Kp_n,5+I*Kp_n
               L,7+I*Kp_n,8+I*Kp_n
               L,9+I*Kp_n,10+I*Kp_n
               *GET,Line_ID2,LINE,0,NUM,MAXD
               L,1+I*Kp_n,2+I*Kp_n
               L,2+I*Kp_n,4+I*Kp_n
               L,3+I*Kp_n,5+I*Kp_n
               L,5+I*Kp_n,6+I*Kp_n
               L,6+I*Kp_n,7+I*Kp_n
               L,6+I*Kp_n,9+I*Kp_n
               *GET,Line_ID3,LINE,0,NUM,MAXD

               TYPE,1
               SECNUM,1
               REAL,1
               LSEL,S,LINE,,Line_ID1+1 ,Line_ID2
               LESIZE,ALL, , ,n_elements
               LMESH,ALL

               TYPE,2
               SECNUM,1
               REAL,1
               LSEL,S,LINE,,Line_ID2+1 ,Line_ID3
               LESIZE,ALL, , ,1
               LMESH,ALL

*ENDDO

ID_Guide1_base = 8
ID_Guide2_base = 8+Kp_n
ID_Guide3_base = 10
ID_Guide4_base = 10+Kp_n

ID_Guide1_tip = 2
ID_Guide2_tip = 2+Kp_n
!ID_Guide3_tip = 2+Kp_n*2
!ID_Guide4_tip = 2+Kp_n*3

CSYS,0
ALLSEL,ALL
*GET,KP_Cur,KP,0,NUM,MAXD
K,KP_Cur+1,0,0
*GET,Line_ID1,LINE,0,NUM,MAXD
L,ID_Guide1_tip,KP_Cur+1
L,ID_Guide2_tip,KP_Cur+1
!L,ID_Guide3_tip,KP_Cur+1
!L,ID_Guide4_tip,KP_Cur+1
*GET,Line_ID2,LINE,0,NUM,MAXD

ID_Gear_Center = KP_Cur+1

TYPE,2
SECNUM,1
REAL,1
LSEL,S,LINE,,Line_ID1+1 ,Line_ID2
LESIZE,ALL, , ,1
```

```
LMESH,ALL

!!!!!!!!!!!!!!!!!!!!!!!!!!!!!!!!!!!!!!!!!!!!!!!!!!!!!!!
!!!!!!!!!!!!!!KP->NODE !!!!!!!!!!!!!!!!
!!!!!!!!!!!!!!!!!!!!!!!!!!!!!!!!!!!!!!!!!!!!!!!!!!!!!!!


KSEL,S,KP,,ID_Guide1_base
NSLK,S
*GET, ID_Guide1_base,NODE,,NUM,MIN
KSEL,S,KP,,ID_Guide2_base
NSLK,S
*GET, ID_Guide2_base,NODE,,NUM,MIN
KSEL,S,KP,,ID_Guide3_base
NSLK,S
*GET, ID_Guide3_base,NODE,,NUM,MIN
KSEL,S,KP,,ID_Guide4_base
NSLK,S
*GET, ID_Guide4_base,NODE,,NUM,MIN

KSEL,S,KP,,ID_Guide1_tip
NSLK,S
*GET, ID_Guide1_tip,NODE,,NUM,MIN
KSEL,S,KP,,ID_Guide2_tip
NSLK,S
*GET, ID_Guide2_tip,NODE,,NUM,MIN
!KSEL,S,KP,,ID_Guide3_tip
!NSLK,S
!*GET, ID_Guide3_tip,NODE,,NUM,MIN
!KSEL,S,KP,,ID_Guide4_tip
!NSLK,S
!*GET, ID_Guide4_tip,NODE,,NUM,MIN

KSEL,S,KP,,ID_Gear_Center
NSLK,S
*GET, ID_Gear_Center,NODE,,NUM,MIN
ALLSEL,ALL

!EDELE,175
!EDELE,177
!!!!!!!!!!!!!!!!!!!!!!!!!!!!!!!!!!!!!!!!!!!!!!!!!!!!!!!
!!!!!!!!!!!!!!SOL !!!!!!!!!!!!!!!!
!!!!!!!!!!!!!!!!!!!!!!!!!!!!!!!!!!!!!!!!!!!!!!!!!!!!!!!


/SOL
/ESHAPE,1
NLGEOM,1
OUTRES,ALL,ALL
SOLCONTROL,ON,ON
!AUTOTS,ON
NEQIT,200
NSUBST,substeps ,,substeps

!Prestress
TIME,1
```

```
D,ID_Gear_Center,Uy,eccentricity
D,ID_Gear_Center,Ux,0
D,ID_Guide1_base,ALL
D,ID_Guide2_base,ALL
D,ID_Guide3_base,ALL
D,ID_Guide4_base,ALL

!D,ID_Guide3_base,ALL
!D,ID_Guide4_base,ALL

SOLVE

!steps = 100
!*DO,I,1,steps
!               TIME,I+1
!               NSUBST,1,,1
!               angle = (90/180)*pi ! direction of deflection measurement
!               D,ID_Gear_Center,Uy,(I*eccentricity/steps)*cos(angle) + sensy
!               D,ID_Gear_Center,Ux,(I*eccentricity/steps)*sin(angle) + sensx
!               SOLVE
!*ENDDO

steps = 100
*DO,I,1,steps
               TIME,I+1
               NSUBST,1,,1
               angle = 4*pi/2/steps*I
               D,ID_Gear_Center,Uy,eccentricity*cos(angle) + sensy
               D,ID_Gear_Center,Ux,eccentricity*sin(angle) + sensx
               F,ID_Gear_Center,Mz,input_M
               SOLVE
*ENDDO


/POST26
TIMERANGE,1,steps+1
NSOL,2,ID_Gear_Center,U,X,
NSOL,3,ID_Gear_Center,U,Y,
RFORCE,4,ID_Gear_Center,F,X,FX
RFORCE,5,ID_Gear_Center,F,Y,FY
PLVAR,4,5


*CREATE,scratch,gui
*DEL,VAR_export
*DIM,VAR_export,TABLE,500,5
VGET,VAR_export(1,0),1
VGET,VAR_export(1,1),2
VGET,VAR_export(1,2),3
VGET,VAR_export(1,3),4
VGET,VAR_export(1,4),5
/OUTPUT,'APDL_Result_test','txt','C:\Users\Jan\Desktop\Thesis\Prototypes
\1-1_scale_May2015\Measurements'
*VWRITE,VAR_export(1,0),VAR_export(1,1),VAR_export(1,2),VAR_export(1,3),...
VAR_export(1,4),smax_vec,smax_vec
%G, %G, %G, %G, %G, %G, %G
```

```
/OUTPUT,TERM
*END
/INPUT,scratch,gui
```

B

ANSYS APDL CODE IMPROVED MODEL - DUAL LAYER

```
FINISH
/CLEAR
/OUTPUT


pi = 3.14159265359

!!!!!!!!!!!!!!!!!!!!!!!!!!!!!!!!!!!!!!!!!!!!!!!!!!!!!!!!!!!!!!!!!!!!!!!!!!!!!!!

l_f = 14.3e-3 !        length flexures
r_f = 8.9e-3!   radius flexures
R = 8e-3! radius central gear

eccentricity = 300e-6

layer_space = 400e-6

input_M = -9e-3!-0.1950 ! [Nm] input moment as result of barrel spring torque
input_F = -input_M/R ! [N] input force as result of barrel spring torque

pos_Fsh = 1000e-6 ! distance used to obtain location for pushing force on shuttle
(force must be directed at center)

!!!!!!!!!!!!!!!!!!!!!!!!!!!!!!!!!!!!!!!!!!!!!!!!!!!!!!!!!!!!!!!!!!!!!!!!!!!!!!!

n_elements = 20
substeps = 10

/PREP7
ET,1,BEAM188
ET,2,MPC184
KEYOPT,2,1,1
KEYOPT,2,2,1


/ESHAPE,1
```

```
SECTYPE,1,beam,RECT
SECOFFSET,CENT,,,
SECDATA ,50e-6, 525e-6

MPTEMP,,,,,,,,
MPTEMP,1,0
MPDATA,EX,1,,169e9
MPDATA,EY,1,,169e9
MPDATA,EZ,1,,130e9
MPDATA,PRXY,1,,0.064
MPDATA,PRYZ,1,,0.36
MPDATA,PRXZ,1,,0.28
MPDATA,GXY,1,,50.9e9
MPDATA,GYZ,1,,79.6e9
MPDATA,GXZ,1,,79.6e9
MP,DENS,1,2330
MP,Mu,1,0.14

!!!!!!!!!!!!!!!!!!!!!!!!!!!!!!!!!!!!!!!!!!!!!!!!!!!!!!!
!!!!!!!!!!!!!! suspension !!!!!!!!!!!!!!!
!!!!!!!!!!!!!!!!!!!!!!!!!!!!!!!!!!!!!!!!!!!!!!!!!!!!!!!

*DO,I,0,1


               CSYS,1

        K,200,0,0,0

                K,1+I*100,0,0,layer_space-I*(2*layer_space)

                K,2+I*100,sqrt((l_f**2)/4 + r_f**2),-atan(l_f/(2*r_f))*...
                180/pi + I*90,layer_space-I*(2*layer_space)
                K,3+I*100,sqrt((l_f**2)/4 + r_f**2),atan(l_f/(2*r_f))*...
                180/pi + I*90,layer_space-I*(2*layer_space)

                K,4+I*100,sqrt((l_f**2)/4 + r_f**2),-atan(l_f/(2*r_f))*...
                180/pi + 90 + I*90,layer_space-I*(2*layer_space)
                K,5+I*100,sqrt((l_f**2)/4 + r_f**2),atan(l_f/(2*r_f))*...
                180/pi + 90 + I*90,layer_space-I*(2*layer_space)

                K,6+I*100,sqrt((l_f**2)/4 + r_f**2),-atan(l_f/(2*r_f))*...
                180/pi + 180 + I*90,layer_space-I*(2*layer_space)
                K,7+I*100,sqrt((l_f**2)/4 + r_f**2),atan(l_f/(2*r_f))*...
                180/pi + 180 + I*90,layer_space-I*(2*layer_space)

                K,8+I*100,sqrt((l_f**2)/4 + r_f**2),-atan(l_f/(2*r_f))*...
                180/pi + 270 + I*90,layer_space-I*(2*layer_space)
                K,9+I*100,sqrt((l_f**2)/4 + r_f**2),atan(l_f/(2*r_f))*...
                180/pi + 270 + I*90,layer_space-I*(2*layer_space)

                K,10+I*100,r_f + pos_Fsh,-90 + I*90,layer_space-I*...
                (2*layer_space)         ! location for shuttle force...

               CSYS,0
```

```
               *GET,Line_ID1,LINE,0,NUM,MAXD
               L,2+I*100,3+I*100
               L,4+I*100,5+I*100
               L,6+I*100,7+I*100
               L,8+I*100,9+I*100
               *GET,Line_ID2,LINE,0,NUM,MAXD
               L,1+I*100,2+I*100
               L,1+I*100,6+I*100
               L,3+I*100,4+I*100
               L,3+I*100,7+I*100
               L,3+I*100,8+I*100
               L,3+I*100,10+I*100

               *GET,Line_ID3,LINE,0,NUM,MAXD

                CSYS,1

                TYPE,1
               SECNUM,1
               REAL,1
               LSEL,S,LINE,,Line_ID1+1 ,Line_ID2
               LESIZE,ALL, , ,n_elements
               LMESH,ALL

               TYPE,2
               SECNUM,1
               REAL,1
               LSEL,S,LINE,,Line_ID2+1 ,Line_ID3
               LESIZE,ALL, , ,1
               LMESH,ALL

*ENDDO

!!!!!!!!!!!! connect layers together

               *GET,Line_ID3,LINE,0,NUM,MAXD
               L,1,200
               L,101,200
               *GET,Line_ID4,LINE,0,NUM,MAXD
               TYPE,2
               SECNUM,1
               REAL,1
               LSEL,S,LINE,,Line_ID3+1 ,Line_ID4
               LESIZE,ALL, , ,1
               LMESH,ALL

!!!!!!!!!!!!!!!!!!!!!!!!!!!!!!!!!!!!!!!!!!!!!!!!!!!!!!!
!!!!!!!!!!!!!SOL !!!!!!!!!!!!!!!
!!!!!!!!!!!!!!!!!!!!!!!!!!!!!!!!!!!!!!!!!!!!!!!!!!!!!!!

CSYS,0
NSEL,ALL
NROTAT,ALL

/SOL
/ESHAPE,1
```

```
NLGEOM,ON
OUTRES,ALL,ALL
SOLCONTROL,ON,ON
AUTOTS,ON
NEQIT,200
NSUBST,substeps ,,substeps

        D,85,UZ,0
        D,23,ALL
        D,65,ALL
        D,109,ALL
        D,151,ALL

SOLVE

TIME,1

steps = 100
*DO,I,1,steps

        TIME,I+1
        NSUBST,1,,1
        angle = 4*pi/2/steps*I

        F,173,Mz,input_M + sensy
        F,173,Fy,input_F*cos(angle)
        F,173,Fx,input_F*sin(angle)

        D,86,UY,eccentricity*sin(angle)
        D,172,UX,-eccentricity*cos(angle)

        SOLVE
*ENDDO

FINISH
/POST1
PLDISP,0

/POST26
TIMERANGE,1,steps+1
NSOL,2,172,U,X,
NSOL,3,86,U,Y,
RFORCE,4,172,F,X,FX
RFORCE,5,86,F,Y,FY
RFORCE,6,172,F,Y,FN1
RFORCE,7,86,F,X,FN2

PLVAR,2,3

*CREATE,scratch,gui
*DEL,VAR_export
*DIM,VAR_export,TABLE,500,6
VGET,VAR_export(1,0),1
VGET,VAR_export(1,1),2
VGET,VAR_export(1,2),3
VGET,VAR_export(1,3),4
```

```
VGET,VAR_export(1,4),5
VGET,VAR_export(1,5),6
VGET,VAR_export(1,6),7


/OUTPUT,'APDL_Result_2_layer','txt','C:\Users\Jan\Desktop\New␣model
(cylindrical␣coordinates)'
*VWRITE,VAR_export(1,0),VAR_export(1,1),VAR_export(1,2),VAR_export(1,3),...
VAR_export(1,4),VAR_export(1,5),VAR_export(1,6)
%G, %G, %G, %G, %G, %G, %G
/OUTPUT,TERM
*END

/INPUT,scratch,gui
```

C

Matlab script Linear Beam Theory model

```
clear all
close all
clc

E = 169e9; % [Pa] youngs modulus silicon (approximate)
L = 14.3e-3%5e-3; % [m] length of flexure
w = 525e-6; % [m] width of the flexures
t = 50e-6; % [m] thickness of the flexures

M = 0%9e-3; % [Nm] moment applied (clockwise = POSITIVE)
e = 300e-6; % [m] eccentricity (=displacement)
R = 5.2e-3; % [m] radius of central gear (affects applied force)
F_input = 0%M/R; % [N] force pulling (or pushing) on flexure

xdist = 8.9e-3%(11.35e-3)/2%8.9e-3; % [m] horizon9tal distance (radius)
from flexures 1 and 2 to center (origin)
ydist = 8.9e-3%7.4e-3; % [m] vertical distance (radius) from flexures 3 and 4
 to center (origin)

angle = [0:(2*pi/1000):2*pi];

%% input displacement and force
x = e*sin(angle);
y = e*cos(angle);

Fx = -F_input*cos(angle);
Fy = F_input*sin(angle);

d = [x;y]';
F_in␣=␣[Fx;Fy]';

% figure
% plot(x,y)
% hold on
% plot(x(1),y(1),'o')

%% Forces from Free-Body-Diagram (flexures considered to be very stiff
```

```
 in longitudinal direction)
F1 = (1/2)*(-M/xdist + F_in(:,2)); %
F2 = (1/2)*(-M/xdist - F_in(:,2));

F3 = (1/2)*(-M/ydist + F_in(:,1));
F4 = (1/2)*(-M/ydist - F_in(:,1));

i=251
d(i,:)
F1(i,:)
F2(i,:)
F3(i,:)
F4(i,:)

% figure
% plot(F1)



%% stiffness
t1 = 24.1e-6;
t2 = 19.1e-6;

I = (w*t^3)/12; % rectangular cross-section assumed
    a=t2;
    b=t1;
    I2 = w*(a+b)*(a^2+b^2)/48; % trapezoidal cross-section assumed

cf = (12*E*I)/L^3;

c1 = F1/L + cf;
c2 = F2/L + cf;
c3 = F3/L + cf;
c4 = F4/L + cf;

cx = c1 + c2; % [N/m] stiffness in x-direction
cy = c3 + c4; % [N/m] stiffness in y-direction

% figure
% plot(angle,c1)

%% forces

Fr1 = d(:,1).*c1; % [N] reaction flexure 1
Fr2 = d(:,1).*c2; % [N] reaction flexure 1
Fr3 = d(:,2).*c3; % [N] reaction flexure 1
Fr4 = d(:,2).*c4; % [N] reaction flexure 1

Frx = Fr1 + Fr2; % [N] reaction x-direction
Fry = Fr3 + Fr4; % [N] reaction y-direction

% geometrical force (triangle)
Fgeomx =  F1.*(d(:,1)/L) + F2.*(d(:,1)/L);
Fgeomy =  F3.*(d(:,2)/L) + F4.*(d(:,2)/L);

% stiffness + geometrical reaction forces combined
```

```
Ftotx = Frx+Fgeomx;
Ftoty = Fry+Fgeomy;

% figure(5)
% plot(angle,Fgeomx)
% hold on
% plot(angle,Fgeomy)

%% mirrored system !!!

%Ftotx = 2*Ftotx;
%Ftoty = 2*Ftoty;


%     tot_reac = sqrt(Ftotx.^2+Ftoty.^2);
%     x = angle;
%     sens = 'Matlab_opt_0Nmm.mat';
%     save(sens, 'x', 'tot_reac');


%% plotting
figure(1)
plot(Ftotx,Ftoty) % [N] reaction forces in x- and y-direction
hold on
plot(Ftotx(1),Ftoty(1),'o')
xlabel('reaction␣force␣x-component')
ylabel('reaction␣force␣y-component')

%     savemat = 'Mx10y12.mat';
%     save(savemat,'Ftotx', 'Ftoty');

figure(2)
plot(angle,sqrt(Ftotx.^2+Ftoty.^2))
xlabel('angle␣[rad]')
ylabel('reaction␣force␣magnitude␣[N]')
%axis([0, 2*pi, 0, 0.5])

figure(3)
plot(angle,F1)
hold on
plot(angle,F2,'--')
plot(angle,F3,'-r')
plot(angle,F4,'--r')
xlabel('angle␣[rad]')
ylabel('reaction␣forces␣individual␣flexures')
legend('F1␣[N]','F2␣[N]','F3␣[N]','F4␣[N]')

figure(4)
plot(angle,c1)
hold on
plot(angle,c2,'--')
plot(angle,c3,'-r')
plot(angle,c4,'--r')
xlabel('angle␣[rad]')
ylabel('lateral␣stiffness␣of␣individual␣flexures')
legend('c1␣[N/m]','c2␣[N/m]','c3␣[N/m]','c4␣[N/m]')
```

D

Matlab script cycloidal rotor

```
clear all; close all; clc
syms t x y

%% rotor

format long

% R = 8; % radius of the rotor [mm]
% E = 0.295; % eccentricity [mm]
% Rr = 2; % radius of rollers [mm]
% N = 12; % number of rollers annulus
% Q = Rr/R; % roller radius ratio
% P = E/R;

R = linspace(7,7,1);
E = linspace(0.295,0.295,1);
Rr = linspace(0.8,0.8,1);
N = linspace(21,21,1); % number of rollers annulus

t = [0:0.0001:2*pi];

%% Solidworks shape
% x_rotor_SW = (R*cos(t))-(Rr*cos(t+atan(sin((1-N)*t)/((R/(E*N))-cos((1-N)*t)))))-...
(E*cos(N*t))
% y_rotor_SW = (-R*sin(t))+(Rr*sin(t+atan(sin((1-N)*t)/((R/(E*N))-cos((1-N)*t)))))+..
(E*sin(N*t))


%% equation for rotor

% x_rotor = (R*cos(t))-(Rr*cos(t+atan2(sin((1-N)*t),((R/(E*N))-cos((1-N)*t)))))-...
(E*cos(N*t));
% y_rotor = (-R*sin(t))+(Rr*sin(t+atan2(sin((1-N)*t),((R/(E*N))-cos((1-N)*t)))))+...
(E*sin(N*t));
% C = sum((sqrt(diff(x_rotor).^2 + (diff(y_rotor)).^2))); % circumference of
cycloidal disk
%
% figure
% plot(x_rotor,y_rotor)
```

```
% axis equal
% xlabel('[mm]')
% ylabel('[mm]')

%% optimize to efficiency based on formula
% R_vec = linspace(10/2,13/2,7);
% E_vec = linspace(0.3,0.3,1);
% Rr_vec = linspace(0.2,2,19);
% N_vec = linspace(10,20,11);
R_vec = linspace(7,7,1);
E_vec = linspace(0.295,0.295,1);
Rr_vec = linspace(0.3,0.9,7);
N_vec = linspace(21,21,1); % number of rollers annulus

mu = 0.3; % friction coefficient

etha = zeros(length(R_vec),length(E_vec),length(Rr_vec),length(N_vec));

    %sens = zeros(1,length(N_vec));
tic
for i = 1:length(R_vec)
    R = R_vec(i);
    i
    length(R_vec)
    for j = 1:length(E_vec)
        E = E_vec(j);

        for k = 1:length(Rr_vec)
            Rr = Rr_vec(k);
            if E_vec(j) < Rr_vec(k)
            Q = Rr/R; % roller radius ratio
            P = E/R;

            for l = 1:length(N_vec)
                N = N_vec(l);
                if Rr < R*sin(pi/N)
                    if Q < sin(pi/N)
                        if P < (1/N-(1e-4))
                    x_rotor = (R*cos(t))-(Rr*cos(t+atan2(sin((1-N)*t),...
                    ((R/(E*N))-cos((1-N)*t)))))-(E*cos(N*t));
                    y_rotor = (-R*sin(t))+(Rr*sin(t+atan2(sin((1-N)*t),...
                    ((R/(E*N))-cos((1-N)*t)))))+(E*sin(N*t));
                    C = sum((sqrt(gradient(x_rotor).^2 +...
                    (gradient(y_rotor)).^2))); % circumference of
                    cycloidal disk [mm]
                    % efficiency
                    etha(i,j,k,l) = 1 - (((mu*C)/(2*pi))
                    *(1/(E*(N-1)))); % efficiency cycloidal gear
                    profile for cylinders fixed to annulus
                       %sens(l) = etha(i,j,k,l);
                        end
                    end
                end
            end
            end
        end
```

```
    end
end
toc

%[sorted_etha, index] = sort(etha,'ascend'); % trying to find the 10
best solutions!!


[i,j,k,l] = ind2sub([length(R_vec),length(E_vec),length(Rr_vec),length(N_vec)],...
find(etha==max(max(max(max(etha))))));

[R_vec(i),E_vec(j),Rr_vec(k),N_vec(l)]
etha_opt_formula = max(max(max(max(etha))))

R = R_vec(i); E = E_vec(j); Rr = Rr_vec(k); N = N_vec(l);

x_rotor = (R*cos(t))-(Rr*cos(t+atan2(sin((1-N)*t),((R/(E*N))-cos((1-N)*t)))))-...
(E*cos(N*t));
y_rotor = (-R*sin(t))+(Rr*sin(t+atan2(sin((1-N)*t),((R/(E*N))-cos((1-N)*t)))))+...
(E*sin(N*t));

figure
plot(x_rotor,y_rotor)
axis equal
xlabel('gear␣shape␣x␣[mm]')
ylabel('gear␣shape␣y␣[mm]')

% save('GridSearch_literature.mat','etha')

%% Efficiency based on kinematics
K = 0.087%0.019 %(0.038/0.3) % reaction force including applied input
torque of 9Nmm (increases normal force)
% 0.019;  [N/mm] spring stiffness suspension (measurement)

[energy_loss] = Efficiency_kinematics(R,E,Rr,N,K,mu,t); % [Nmm] energy loss

energy_loss_J_per_rotation = energy_loss*1e-3; % [J] energy loss in Joule
(1 times circumference)
energy_delivered = ((10+6.3)/2); % [Nmm]rough calculation
of energy in barrel spring for a single rotation
energy_delivered_J_per_rotation = energy_delivered*1e-3; % [J] energy
delivered in Joule by barrel spring for a single rotation
etha_kinematics = (energy_delivered_J_per_rotation-energy_loss_J_per_rotation)/...
energy_delivered_J_per_rotation

% figure
% plot(x_rotor,y_rotor)
% hold on
% plot(x_rotor(energy_loss),y_rotor(energy_loss),'*r')

%% sensitivity plots

% figure(1)
% plot(Rr_vec(6:end),sens(6:end),'LineWidth',2)
% xlabel('Radius␣roller␣R_r')
% ylabel('Efficiency␣\eta␣according␣to␣literature')
```

```
% title('Sensitivity␣R_r')

% figure(1)
% plot(N_vec(1:6),sens(1:6),'LineWidth',2)
% xlabel('Number␣of␣rollers␣N')
% ylabel('Efficiency␣\eta␣according␣to␣literature')
% title('Sensitivity␣N')

%% large scale proto
% R = 120; % radius of the rotor [mm]
% E = 10; % eccentricity [mm]
% Rr = 25; % radius of rollers [mm]
% N = 10; % number of rollers

%% silicon micro design
% R = 5.2; % radius of the rotor [mm]
% E = 0.295; % eccentricity [mm]
% Rr = 0.6; % radius of rollers [mm]
% N = 16; % number of rollers
```

E

Matlab script cycloidal rotor contact force analysis

```
function efficiency = efficiency(R,E,Rr,N,K,mu,t)

% clear all
% close all
% clc
% R = linspace(5.2,5.2,1);
% E = linspace(0.295,0.295,1);
% Rr= linspace(0.6,0.6,1);
% N = linspace(16,16,1);

% R = 16/2;
% E = 0.295;
% Rr = 2;
% N = 12; % number of rollers annulus
% K = 0.022124;%0.015526243681761;
% mu = 0.3;
% t = [0:0.0001:2*pi];

x_rotor = (R*cos(t))-(Rr*cos(t+atan2(sin((1-N)*t),((R/(E*N))-cos((1-N)*t)))))-...
(E*cos(N*t));
y_rotor = (-R*sin(t))+(Rr*sin(t+atan2(sin((1-N)*t),((R/(E*N))-cos((1-N)*t)))))+...
(E*sin(N*t));
M_radius = [(sqrt(x_rotor.^2 + y_rotor.^2))'];␣%␣[mm]␣distance␣to␣center␣for
␣each␣point␣on␣rotor␣surface␣for␣calculation␣of␣reaction␣moment␣by␣friction

F␣=␣K*(E);␣%␣[N]␣reaction␣force␣of␣suspension
F_vec␣=␣zeros(length(x_rotor),3);
for␣i␣=␣1:length(x_rotor)
␣␣␣␣F_vec(i,:)␣=␣F*[-cos(t(i)),sin(t(i)),0];␣%␣force␣as␣a␣result␣of
␣␣␣␣␣suspension␣stiffness␣(depending␣on␣position␣of␣contact)
end

xgrad␣=␣gradient(x_rotor);
ygrad␣=␣gradient(y_rotor);
Surf_grad_vec␣=␣[xgrad',ygrad',zeros(length(xgrad),1)];␣%␣gradient␣of
␣rotor␣surface␣calculated
```

```
theta␣=␣zeros(length(x_rotor),1);
F_norm␣=␣zeros(length(x_rotor),1);
moment_F_friction␣=␣zeros(length(x_rotor),1);

for␣k␣=␣1:length(x_rotor)
␣␣␣␣%theta(k)␣=␣pi-acos(dot(F_vec(k,:),Surf_grad_vec(k,:))/...
␣␣␣␣(norm(F_vec(k,:))*norm(Surf_grad_vec(k,:))));␣%␣[rad]␣angle
␣␣␣␣between␣spring␣force␣and␣surface␣gradient
␣␣␣␣%theta(k)␣=␣atan2(norm(cross(F_vec(k,:),Surf_grad_vec(k,:))),...
␣␣␣␣dot(F_vec(k,:),Surf_grad_vec(k,:)));
␣␣␣␣u␣=␣F_vec(k,:);
␣␣␣␣v␣=␣Surf_grad_vec(k,:);
␣␣␣␣theta(k)␣=␣atan2(norm(cross(u,v)),dot(u,v));
␣␣␣␣F_norm(k)␣=␣F*sin(theta(k));
␣␣␣␣moment_F_friction(k)␣=␣sin(theta(k))␣*␣mu␣*␣F_norm(k)␣*...
␣␣␣␣␣M_radius(k);␣%␣[Nmm]␣Moment␣as␣a␣result␣of␣friction
␣␣␣␣␣force␣(=␣measured␣friction␣force)
end

%␣figure
%␣plot(t(1:15708),theta((1:15708))*180/pi)

%␣figure
%␣plot(F_norm)
%␣test␣=␣find(F_norm␣<␣0.12);
%␣test␣=␣find(F_norm␣>␣0.25);
%␣theta(test);

F_friction_vec␣=␣mu*F_norm;␣%␣calculation␣Coulomb␣friction␣force
C␣=␣[(sqrt(gradient(x_rotor).^2␣+␣(gradient(y_rotor)).^2))];␣%␣travel
␣distance␣circumference␣cycloidal␣disk␣[mm]

%␣test=1
%␣figure
%␣plot(x_rotor((end-16750):end),y_rotor((end-16750):end),'LineWidth',2)
%␣␣axis([-1␣7␣-1␣7])
%␣hold␣on
%␣plot(x_rotor(test),y_rotor(test),'o')

%
%␣figure
%␣plot(t(1:15708),F_friction_vec(1:15708))

energy_loss␣=␣gradient(t)*moment_F_friction;%C*F_friction_vec;␣%␣[Nmm]

%␣figure
%␣plot(t,F_Norm)
%␣plot(t,F_friction_vec)

%␣figure
%␣plot(t(1:15708),theta(1:15708))
%
figure
plot(t(1:end),moment_F_friction(1:end),'LineWidth',2)
hold␣on
plot(t(1:end),mean(moment_F_friction(1:end)))
```

```
xlabel('position of contact point on gear surface [rad]')
ylabel('moment as a result of friction forces [Nmm]')
axis([0 2*pi 0 0.015])
%
%      sens = 'Matlab_moment_F_friction';
%      save(sens, 't', 'moment_F_friction');

% figure
% plot(t,720*moment_F_friction)
% xlabel('position of contact point on gear surface [rad]')
% ylabel('expected at rheometermoment as a result of friction forces [Nmm]')
% axis([0 2*pi 0 720*0.20])

% figure
% plot(t(1:15708),moment_F_friction(1:15708),'LineWidth',2)
% axis([0 2*pi/4 0 0.05])
% ylabel('expected moment as a result of friction forces [Nmm]')
% xlabel('position of contact point on gear surface [rad]')
% mean(moment_F_friction)

efficiency = energy_loss;
```

F

ANSYS APDL CODE FOR NEGATIVE STIFFNESS

```
!!!!!!
!! double bistable suspension: test to see stiffness profile in x and y direction
!!!!!!

        FINISH
        /CLEAR
        /OUTPUT

        ! Constant values
        w = 500e-6                              ![m]    Width of beams
        n = 50                                  ![]             Mesh
        datapoints = 50
        pi = 3.14159265359

        ! Variables that can be changed
        l = 7e-3                                ![m]    Length of beams
        angle = 14
        alpha = angle*(acos(-1)/180)            ![radian]       Angle of the beams
        alpha2 = (angle+90)*(acos(-1)/180)
        t = 30e-6                               ![m]    Thickness of beams
        curve_rad = 200e-3                      ![m]    Length radius curve_rad
        l_rigid1 = l                            ![m] length rigid horizontal
        l_rigid2 = l/2                          ![m] length rigid vertical

        Gear_Radius = 300e-6    ! radius of circular path [m]

        sensx = 0e-6! sensitivity in x-direction [m]
        sensy = 0e-6! sensitivity in y-direction [m]

        prestressx =  -1740e-6 + sensx ! prestress towards bistable center [m]
        prestressy =  prestressx + sensy ! prestress towards bistable center [m]


        ! Radius calculations
        curve_centerx_1 = l_rigid1 + curve_rad*cos(alpha)+l*0.5*sin(alpha)...
        ![m] Curve center x location
        curve_centery_1 = curve_rad*sin(alpha)-l*0.5*cos(alpha)...
```

```
        ![m] Curve center y location

        curve_centerx_2 = curve_rad*cos(alpha2)+l*0.5*sin(alpha2)...
        ![m] Curve center x location
        curve_centery_2 = -l_rigid2 + curve_rad*sin(alpha2)-l*0.5*cos(alpha2)...
        ![m] Curve center y location

        !dx = 1.1
        !dy = 1.1
        !travelrangex = dx*sin(alpha)*l ![m]    Displacement for final...
         movement, movement should be symmetrical
        !travelrangey = dy*sin(alpha)*l ![m]    Displacement for final...
         movement, movement should be symmetrical

        /PREP7
        ET,1,BEAM188    !Define local element from the element library
        SECTYPE,1,beam,RECT
SECOFFSET,CENT,,,
SECDATA ,t, w

MPTEMP,,,,,,,,
MPTEMP,1,0
MPDATA,EX,1,,169e9
MPDATA,EY,1,,169e9
MPDATA,EZ,1,,130e9
MPDATA,PRXY,1,,0.064
MPDATA,PRYZ,1,,0.36
MPDATA,PRXZ,1,,0.28
MPDATA,GXY,1,,50.9e9
MPDATA,GYZ,1,,79.6e9
MPDATA,GXZ,1,,79.6e9
MP,DENS,1,2330
MP,Mu,1,0.14

        ET,2,MPC184 ! rigid bodies
        KEYOPT,2,1,1

        ! Keypoints
        K,1,0,0
        K,2,l_rigid1,0
        K,3,0,-l_rigid2

        K,4,l_rigid1+l*cos(alpha2),l*sin(alpha2)
        K,5,l*cos(alpha),l*sin(alpha)-l_rigid2

        K,6,l_rigid1-curve_centerx_1,-curve_centery_1
        K,7,-curve_centerx_2,-l_rigid2-curve_centery_2


        ! Arcs
        LARC,2,4,6,curve_rad
        LARC,3,5,7,curve_rad

        LSEL,S,LINE,,1 ,4
        LESIZE,ALL, , ,n, ,1, , ,1, !Specifies the division and spacing...
        ratio on unmeshed lines, n is ANGSIZ: The division arc spanned by...
```

```
        the elemend edge...
        TYPE,1   !Activates an element type number to be assigned...
        to subsequently defined elements
        SECNUM,1 !Defines the section ID number to be assigned...
        to the subsequently-defined element
        LMESH,ALL        !Generates nodes and line elements along lines.

        L,1,2
        L,1,3

        TYPE,2
        SECNUM,1
        REAL,1
        LSEL,S,LINE,,3 ,4
        LESIZE,ALL, , ,1
        LMESH,ALL

        !Constraints
        D,2,ROT
        D,103,UZ,0
        D,103,ROTZ,0
        D,103,UY,0
        D,2,ALL,0
        D,53,ROTZ,0
        D,53,ROTX,0
        D,53,ROTY,0


/SOL
/ESHAPE,1
NLGEOM,1
OUTRES,ALL,ALL
SOLCONTROL,ON,ON
!AUTOTS,ON
NEQIT,100
NSUBST,substeps ,,substeps

!Prestress
TIME,1

D,53,UX,prestressx
D,53,UY,prestressy
D,103,UX,prestressx
SOLVE

steps = 100

!*DO,I,1,steps
!                       TIME,I+1
!                       NSUBST,1,,1
!                       angle = 4*pi/2/steps*I
!               D,53,UX,-3e-3/steps*I
!               !D,53,UY,-3e-3/steps*I
!               D,103,UX,-3e-3/steps*I
!               SOLVE
!*ENDDO
```

```
*DO,I,1,steps
                TIME,I+1
                NSUBST,1,,1
                angle = 4*pi/2/steps*I
                D,53,UX,prestressx+Gear_Radius*sin(angle)
                D,53,UY,prestressy+Gear_Radius*cos(angle)
                D,103,UX,prestressx+Gear_Radius*sin(angle)
                SOLVE
*ENDDO


!/POST1
!
!! Stress analysis
!!*VEC,smax_vec,D,ALLOC,100
!*DIM,smax_vec,ARRAY,100,2,1, , ,
!
!SET,FIRST
!*DO,i,1,steps
!
!SET,NEAR,,,,i,,,
! /EFACET,1
!PLNSOL, U,SUM, 0,1.0
!AVPRIN,0, ,
!ETABLE,SMAXI,SMISC,32
!AVPRIN,0, ,
!ETABLE,SMAXJ,SMISC,33
!/REPLOT,RESIZE
!PLETAB,SMAXI,NOAV
!
!ESORT,ETAB,SMAXI,0,1
!*GET,SMAXI,SORT,,MAX
!*GET,SMAXJ,SORT,,MAX
!maxstressI = abs(SMAXI)
!!*SET, smax_vec(i,1,1), maxstressI
!smax_vec(i)=maxstressI
!maxstressJ = abs(SMAXJ)
!
!*ENDDO

/POST26
TIMERANGE,1,steps+1
NSOL,2,53,U,X,
NSOL,3,53,U,Y,
RFORCE,4,2,F,X,FX
RFORCE,5,53,F,Y,FY
PLVAR,4,5

*CREATE,scratch,gui
*DEL,VAR_export
*DIM,VAR_export,TABLE,500,5
VGET,VAR_export(1,0),1
VGET,VAR_export(1,1),2
VGET,VAR_export(1,2),3
VGET,VAR_export(1,3),4
```

```
VGET,VAR_export(1,4),5
/OUTPUT,'APDL_Result_silicon','txt','C:\Users\Jan\Desktop\Thesis...
\Suspension\Negative_stiffness'
*VWRITE,VAR_export(1,0),VAR_export(1,1),VAR_export(1,2),VAR_export(1,3),...
VAR_export(1,4),smax_vec,smax_vec
%G, %G, %G, %G, %G, %G, %G
/OUTPUT,TERM
*END
/INPUT,scratch,gui
```